A Dynamic Phasor Model of a
Modular Multilevel Converter for EMT Co-Simulation

by

Rupasinghe Arachchige Tharinda Janesh Kumar Rupasinghe

A thesis submitted to the Faculty of Graduate Studies of
The University of Manitoba
in partial fulfilment of the requirements for the degree of

MASTER OF SCIENCE

Department of Electrical and Computer Engineering
University of Manitoba
Winnipeg.

Abstract

This thesis presents a new dynamic phasor model of a modular multilevel converter (MMC), which can be used for electromagnetic transient (EMT) simulation studies. The model is extendable to capture and replicate any given number of harmonics of the output waveforms and also it produces the most dominant frequency components of internal capacitor voltages and arm currents waveforms. The internal dynamics of the MMC are modeled using the conventional dynamic phasor (CDP) principles in form of a linear state equation system. Solution of the state equations, which is obtained via numerical integration, is then used to build the dynamics of output voltage waveforms of the MMC by applying a new concept referred to as base-frequency dynamic phasors (BFDP). Validation of the model is carried out against a detailed switching model and a detailed average model of an MMC by integrating all three models in an inverter, a rectifier, a back-to-back HVDC system and, a 12-bus system built in PSCAD/EMTDC simulator. Simulation results illustrate that the new MMC model is much more computationally efficient than other two models and is also capable of maintaining a high level of accuracy.

Acknowledgments

This thesis becomes a reality with the kind of support of many individuals. I would like to convey my deepest gratitude to all of them.

First and foremost, I would like to express my profound gratitude to my advisor, Prof. Shaahin Filizadeh for his continuous guidance and consistent advice throughout the research. A special thanks must be conveyed to the examining committee for accepting this thesis for review.

I would also like to acknowledge the support and inspiration given by academic and non-academic staff of the Department of Electrical and Computer Engineering, all the colleagues and friends, whom I shared this wonderful experience with and my beloved family. Furthermore, I am grateful to the Faculty of Graduate Studies, University of Manitoba and Natural Science and Engineering Research Council (NSERC) of Canada for providing financial support for the research. I would also like to acknowledge the technical support I received from Manitoba HVDC Research Center.

Last but not least, I would like to pay tribute to each and everyone, who shared their knowledge and experience in the process of accomplishing this endeavor.

Janesh Rupasinghe

In dedication to

My family,

All my teachers

And friends

Contents

List of Tables

List of Figures

List of Abbreviations

AC   alternative current

BFDP   base-frequency dynamic phasor

CDP   conventional dynamic phasor

DC   direct current

EMT   electromagnetic transient

HVDC   high voltage direct current

IGBT   insulated gate bipolar transistors

LCC   line commutated converter

MMC   modular multilevel converter

NIS   numerical integration substitute

NLC   nearest level control

PCC   point of common coupling

PLL   phase locked loop

PWM   pulse-width modulation

SHE   selective harmonic elimination

SPWM   sinusoidal pulse-width modulation

SVM   space vector modulation

VSC   voltage source converter

Chapter 1

Introduction

1.1   General Background

Evolution of power conversion circuit topologies has led to rapid developments in high voltage direct current (HVDC) power transmission in electrical power systems. HVDC power transmission has traditionally been dominated by thyristor-based line commutated converters (LCCs). Independent control of LCC-HVDC systems without affecting the linked AC system was impossible due to the lack of turn-off capability of thyristors, and thus these conventional HVDC systems are not suitable to operate with weak AC grids [1]. Apart from that, the inability of controlling real and reactive power independently and large filtering requirements of LCC systems have led the industry towards finding new power converter topologies for HVDC systems [1]–[5].

Advancement of power semiconductor devices, especially the introduction of insulated gate bipolar transistors (IGBTs), made voltage source converters (VSC) a reality. VSC topologies are able to overcome most of the challenges with LCCs and offer additional benefits such as black-start capability, fast dynamic performance, and unipolar dc link voltage [3]–[6]. These benefits have caused VSCs to appear in various

applications including renewable energy sources, electric machines drives, and power conditioners [1], [2], [7]. Practical limitations in terms of control and power losses restricted VSCs to two- and three-level converters; these converters were suitable for HVDC applications wherein losses need to be as small as possible [1], [3], [5]. As a result, technologies have moved towards multi-cell converter topologies that provides cost effective and efficient power conversion at high voltages [1], [8]. Introduction of multi-cell converters made a significant improvement to the VSC-HVDC topologies. They produce high-quality voltage waveforms by incrementally adding a number of small and identical voltage levels. As the trend continued, a new multi-cell convertor topology referred to as modular multi-level converter (MMC) was introduced in [9]. Since then, MMCs have received significant attention in high and medium voltage applications due to the unique features and benefits they have to offer.

1.2   EMT Simulation

For majority of time, a power system operates under steady state, and its behaviour can be characterised using voltage and currents in frequency domain. However, energy exchange between electrical and magnetic components under a sudden change in the system such as a switching event, fault or any other disturbance results in large variations of currents and voltages [10]. Exchange of stored energy between electrical fields of capacitors and magnetic fields of inductors in a power system under various dynamic conditions is referred to as electromagnetic transients (EMT) [10], [11]. These transients may consist of dc components as well as frequency components in the range of below one hertz to several kilo-hertz, and die out rapidly, sometimes even before protection decisions may be made. Knowledge about these transients is vital in

determining component ratings, insulation levels, designing protection systems, and explaining equipment failures [12]. Therefore, EMT simulations are carried out in order to understand the power system performances under different disturbances.

Earlier in EMT simulation, state space modeling was used, but it was replaced by the nodal analysis method due to its code complexity, greater solution time, and difficulty of identifying modeling parameters [10]. Nodal analysis-based methods have become the most widely used EMT simulation engines due to their flexibility and simplicity. In such a method, a discrete equivalent of a given element is represented as a current source and a conductance. A set of nodal equations are developed taking as unknowns the voltages of each node. These take the form of (1.1).

$$[Y]\bar{V} = \bar{I} \tag{1.1}$$

where the square matrix $[Y]$ is called the admittance matrix and is made of conductances between each node. The voltage vector $\bar{V}$ consists of node voltages, and $\bar{I}$ with currents of current sources associated with each node.

One of the major challenges in this method is to develop current source–conductance equivalents of capacitors, inductors, and nonlinear elements. A method called numerical integration substitution (NIS) based on trapezoidal integration is employed in many EMT solvers in order to transform these components into current source and conductance equivalents for simulation [10], [11]. This set of nodal equations is then solved by taking the inverse of the admittance matrix to find the node voltages iteratively until the end of simulation is reached. Each iteration increases the time by a fixed time interval, which is referred to as time-step and this procedure is referred to as the electromagnetic transient (EMT) simulation.

For a system with constant conductances, the admittance matrix does not change, and its inversion is required only once for the entire simulation. The systematic nature of this method allows to readily develop nodal equations for large networks in digital computer simulation.

1.3   Problem Definition

The main feature that characterizes an MMC is its multi-cell arrangement. Each cell is made of two or more power electronic switches depending on the cell configuration. A switch is equipped with a small current-limiting inductor and a resistor-capacitor snubber circuit. In EMT simulation programs, capacitors and inductors are represented by a current source and a conductance applying NIS method while a switch is represented by a variable resistance [10]. This is illustrated in Figure 1.1 ignoring current limiting inductance.
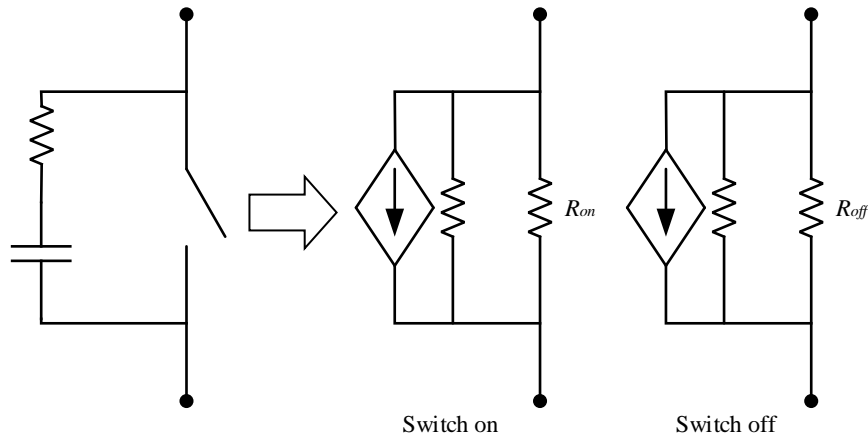
Figure 1.1: EMT simulation program equivalence of switches

When a switching event is detected, the admittance matrix is reformed by changing the value of the switching branch resistance. If the switch is on, a small value is used for the on-time resistance R_{on} and if the switch is off, it can be modeled

by selecting large resistance value for R_{off}. Since the conductance of a switching branch changes each time a switching event occurs, this procedure involves reformation and inversion of the admittance matrix after each such event. As a result, the computational requirement of the EMT algorithm increases commensurately to the number of switching events in the network. If the system consists of frequently switched components such as power electronic converters, computational complexity and simulation time of the EMT solver will be increased significantly.

An MMC is constructed using hundreds of switches in each arm and produces a large number of frequent switching actions. Therefore, a detailed EMT solver must model thousands of switches using the above explained method. This will result in a large number of nodes in the EMT program and the admittance matrix whose size corresponds to the number of nodes in the network subsystem has to be reformed and inverted every time a switching action occur [6], [8]. For this reason, EMT simulation of an MMC integrated network must be carried out using adequately small time-steps in order to obtain transient details accurately. This approach is not practical due to its inefficiency and massive computational burden. Requirement of an efficient technique for EMT simulation of MMC has made the way to simplified and averaged models of MMC.

Dynamic phasors are a widely accepted averaging technique used for EMT simulation of power electronic converters. Effort in this research is to develop a simplified and flexible new MMC model in the context of an EMT solver by employing dynamic phasor theories. The new model will allow direct interfacing of an MMC with the rest of the network built in an EMT simulator.

1.4 Thesis Motivation and Objectives

The types of MMC models for EMT simulation can be classified as detailed models, equivalent circuit based models, arm switching function based models, and average value models. Comparison between different types of MMC models including detailed and average models are given in [6] and [13]. The majority of simplified MMC models, which are based on averaging techniques, replicate the transient responses through simplified functions neglecting switching details of the MMC. A simplified detailed model considering Thévenin equivalent of an MMC is given in [8]. Even though it is faster than the detailed switching model, the speed is much less compared to an average model. Models presented in [13], [14] are based on the arm switching function. These types of models are much faster than most other models and can be used to study the dynamic behaviors of large systems [15]. However, the problem with the arm switching function models is that they do not consider the submodules behavior; therefore, internal dynamics cannot be studied and will be a disadvantage when selecting design parameters such as component ratings and deciding insulation levels.

Several MMC models based on dynamic phasors have been proposed in the literature. One of the attractive features of dynamic phasor modeling is its selectivity, which makes it flexible to include or exclude harmonics. The majority of previous works focus on the modeling of low-frequency components of dynamics and high-frequency components have been ignored. Models presented in [16] and [17] fall into this category. Apart from the MMC model, impact on controller gains during transients is studied using eigen-analysis in [16]. However, it does not provide a comparative validation against a recognized EMT simulator. The phasor model proposed in [17] considers the variables in rotating d-q frame at fundamental

frequency and double the fundamental frequency (for circulating currents). An extended frequency dynamic phasor MMC model is proposed and validated in [18], [19]. This model is flexible to amend any number of higher order harmonics based on the study requirement.

However, all aforementioned MMC models are developed and simulated in the dynamic phasor environment. In other words, MMC interface including AC system, DC system and controllers are also modeled in dynamic phasor domain and they do not have the capability to readily interface with an electrical network build in an EMT simulator.

The motivation of this thesis is to develop an extended-frequency dynamic phasor model of an MMC in the context of an EMT solver. The primary objectives of this thesis can be enumerated as below.

1. Development of a simplified and flexible MMC model for EMT simulation employing dynamic phasor principles. This model must be capable of yielding any given number of harmonics efficiently as per the user requirement and the user must be able to study both internal and external dynamics of the MMC accurately in steady state and during transient events.

2. Integrate the developed MMC model in a recognized EMT simulator interfacing with the rest of the electrical network and control system, which are built in the EMT simulator.

3. Validation of the steady state and dynamic responses and the efficiency of the developed model by comparing the results for various transient events with a detailed IGBT-based MMC model or another validated average MMC-EMT model.

1.5   Thesis Outline

A general background of MMC and EMT simulation was given in this chapter. The rest of the thesis is organized as follows. Chapter 2 presents a comprehensive survey on MMCs including topology, principle of operations, and general applications. Modulation and controlling scheme of MMC submodules are also briefly discussed.

Basic theory behind dynamic phasors is provided in Chapter 3. Mathematical preliminaries of the traditional method and a new dynamic phasor technique are explained and then a comparison is made between the two methods by taking an example case of a three-phase thyristor converter.

An in-depth explanation of the proposed MMC model is presented in Chapter 4. This chapter includes derivation of MMC dynamic equations, applying dynamic phasor principles, switching function details, numerical integration and finally, MMC-EMT interface with AC and DC systems.

Chapter 5 is allocated to validation of the MMC model developed in Chapter 4. This is carried out by comparing results with a widely accepted EMT simulator called PSCAD/EMTDC. Several MMC-HVDC test systems are considered including a rectifier, an inverter, and a back-to-back converter. Moreover, an MMC-based HVDC link is embedded in a twelve-bus network and results are studied.

Finally, conclusions, contributions, and limitations of the proposed model are given in Chapter 6. Suggestions for future improvements of the model are also provided.

Chapter 2

An Introduction to Modular Multilevel Converters (MMCs)

MMCs are the newest member introduced to the VSC family in order to overcome shortcomings of traditional LCC and VSC topologies. Since their introduction, MMCs have become an attractive converter topology in medium and high power applications; and have, therefore, received substantial attention in research studies throughout the past decade [5], [7], [20], [21]. This chapter is dedicated to give an overview about operation, control, and applications of a typical MMC.

An MMC is a multi-cell VSC topology, which connects a large number of submodules to achieve the desired output waveform. Design and configuration of MMCs offer the following important benefits over traditional two-level and three-level VSC topologies [1]–[4], [20]–[24].

➢ **Scalability and redundancy:** The modularity feature of an MMC makes it expandable to any number of output voltage levels. As a result, higher voltages are easily achieved and reliability and redundancy can be improved with minimum cost.

- ➢ **Good harmonic performance:** The output AC waveform of an MMC is produced by switching a large number of small and identical voltage levels and/or using high switching frequency. This produces a nearly sinusoidal waveform at the output with low high order harmonic content, thereby the requirement of a large filter and filter cost can be minimized.

- ➢ **Improved efficiency:** Use of high-frequency pulse-width modulation (PWM) switching methods are not compulsory for MMCs. The switching frequency can be lowered thus saving vast amount of semiconductor switching losses compared to other VSC schemes. Reduced converter power losses overcome a major drawback of conventional VSC and make an MMC an excellent choice in high power applications.

- ➢ **Reduced *dv/dt* ratio:** In an MMC, switching is internal to the submodules; thus, a small fraction of voltage is subjected to switching. This results in a reduced rate of change of voltage of the MMC due to switching. Hence the effect of stray capacitance and the requirement of insulation level become less. Also an MMC does not require a separate DC link capacitor to stabilize the DC voltage.

   However, use of such large number of switching devices brings more challenges particularly in switching and control. Therefore, more effort needs to be devoted to address barriers associated with MMCs.

2.1   MMC Circuit Topology and Operation

An MMC consists of six converter arms, each arm built up by stacking a large number of identical submodules. An arm acts as a variable voltage source that provides a large

number of output voltage levels. This allows the MMC to synthesize an approximately sinusoidal three-phase waveform at its AC side by regulating the operating voltage level of individual arm. Figure 2.1 illustrates a graphical representation of the most common MMC configuration.
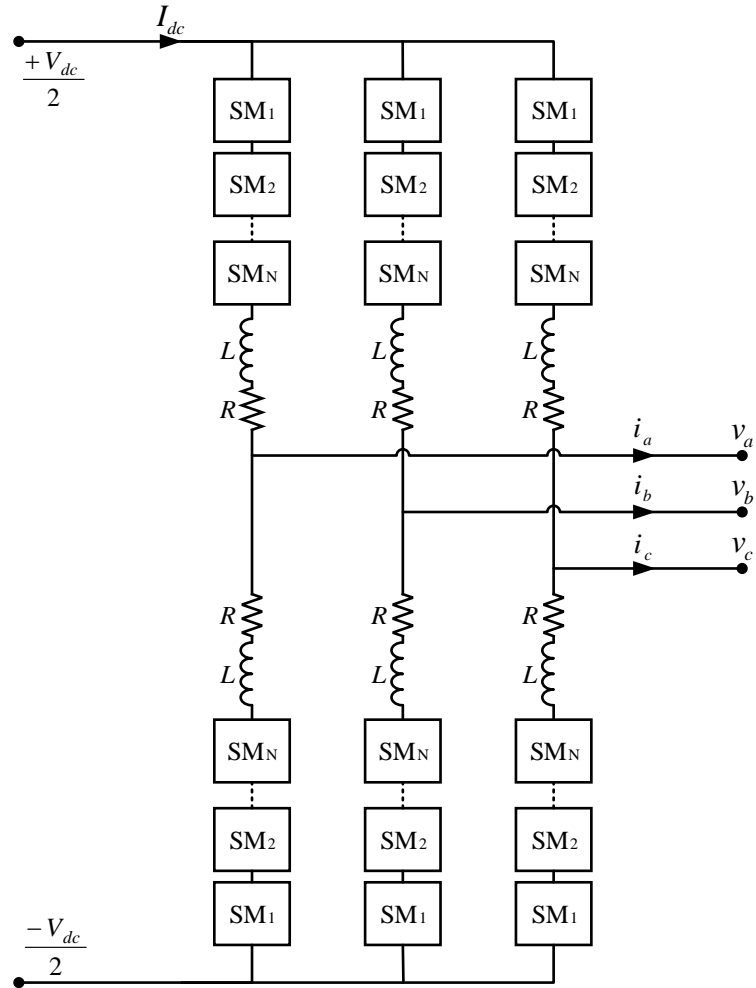
Figure 2.1 : Three-phase MMC configuration

Each submodule consists of IGBT switches and an integrated capacitor. The submodule capacitor can be inserted in series with other submodule in the same arm or bypassed by switching its submodule IGBTs. The most common submodule configurations are the two-level half bridge and three-level full bridge structures. In

a half bridge submodule, the output voltage can be switched either to E or zero, where E is the voltage of the integrated capacitor of the submodule. In the full bridge case, the voltage of each submodule can be switched to $\pm E$ and zero. Figure 2.2 illustrates circuit diagrams and corresponding switching patterns of IGBTs in both configurations.

(a)

(b)
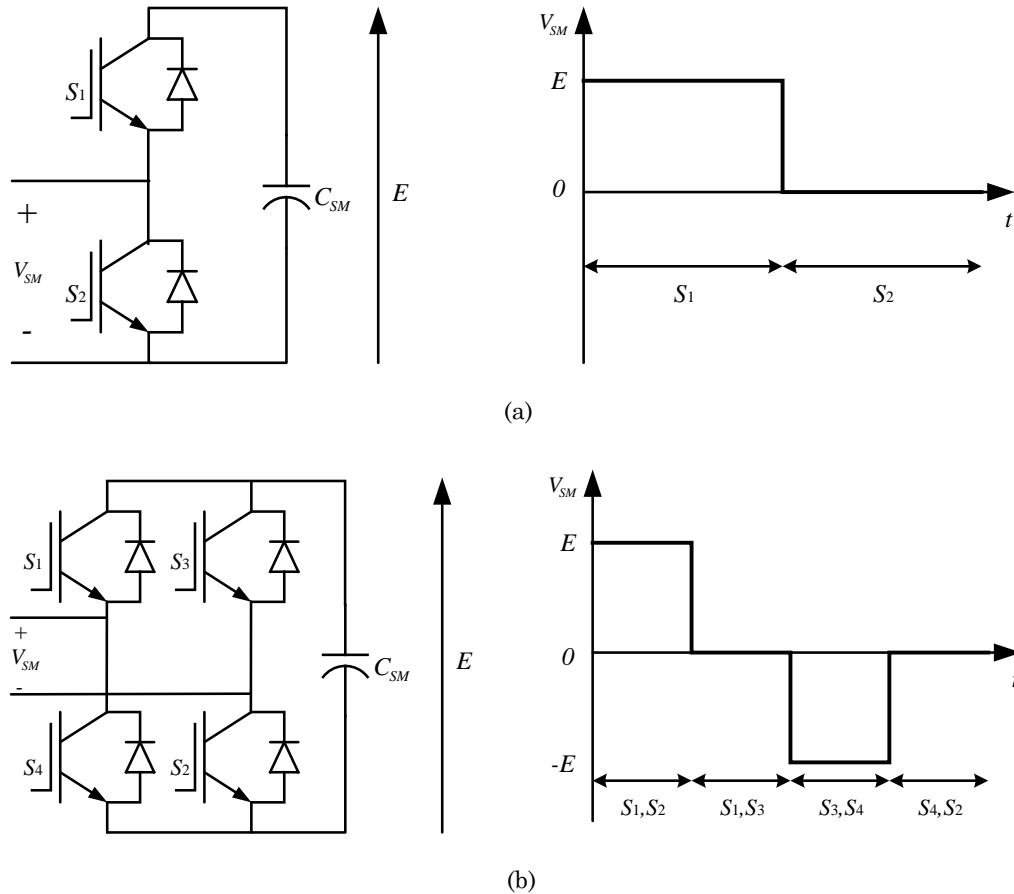
Figure 2.2 : Configurations and switching patter of (a) half-bridge submodule (b) full-bridge submodule

The main drawback of the full bridge scheme is higher number of switches that in turn increases the cost and power losses. Therefore, half bridge submodules are widely used in many MMC-HVDC applications [7], [9], [20]. Hereinafter in this thesis, only the half-bridge submodule structure is considered. More details about different kind of submodule schemes can be found in [25]–[28].

For a given MMC arm, the number of submodule per arm, *N,* is a constant. The maximum number of voltage levels that can be produced in the output voltage using *N* number of submodules is *N*+1. The total voltage of the upper arm and lower arm in the same phase must be equal to the DC voltage and the maximum and minimum voltages that a single arm can achieve are $+V_{dc}/2$ and $-V_{dc}/2$, respectively. Therefore, the nominal voltage of each submodule capacitor can be calculated as

$$E = \frac{V_{dc}}{N} \tag{2.1}$$

Since the total voltage across the upper and lower arms of one leg is equal to V_{dc}, it is clear from (2.1) that the total number of inserted capacitors in one phase leg must be equal to *N* at any given instant. In other words, the sum of inserted capacitors in the upper arm and inserted capacitors in the lower arm in the same leg is equal to *N*. By adjusting the inserted number of submodule capacitors in each arm with time, any desired AC voltage waveform can be synthesized. This procedure is summarized in Table 2-1 and Figure 2.3 considering *N* = 5.

Table 2-1 : MMC submodule switching pattern in a leg

Switching Level	Number of inserted submodule capacitors			AC Voltage
	Upper arm	Lower arm	Total	
①	0	5	5	$V_{dc}/2$
②	1	4	5	$3V_{dc}/10$
③	2	3	5	$V_{dc}/10$
④	3	2	5	$-V_{dc}/10$
⑤	4	1	5	$-3V_{dc}/10$
⑥	5	0	5	$-V_{dc}/2$
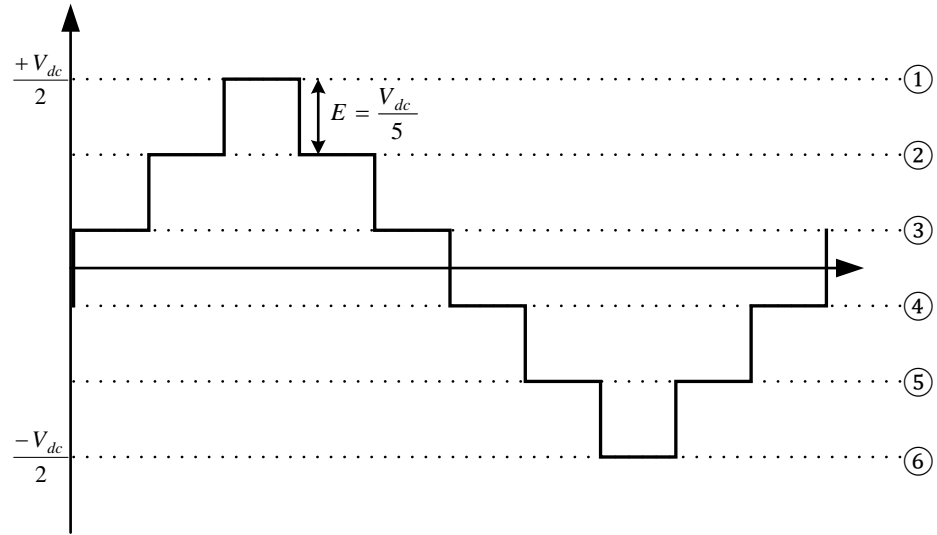
Figure 2.3 : Synthesizing AC voltage waveform of MMC

Generally, the MMC arm consists of a few hundred submodules; thus, the number of voltage levels is high, and the capacitor voltages (voltage step size) become small. By using an appropriate switching technique (for example the one discussed in Section 2.2.1), the desired sinusoidal waveform at the output can be achieved.

Apart from submodule string, each MMC arm includes a small inductor, whose role is to limit high-frequency components of the arm current and the rate of change of current during a critical fault situation such as a DC pole-to-pole short circuit [1], [7], [24]. Furthermore, the arm inductor avoids parallel connection of each arm from the DC side [1], [24]. Each arm is a voltage source and connecting them in parallel will lead to abnormal situations.

Selecting an appropriate value for the arm inductance and submodule capacitance are major design considerations of MMCs. Capacitance selection methods are mainly based on the energy storage inside the MMC [29], [30] and minimizing capacitor voltage ripples [31]. The submodule capacitance can be calculated based on the energy to power ratio (*EP*) as below.

$$C_{SM} = \frac{EP \times S_{MMC} \times N}{3V_{dc}^2} \tag{2.2}$$

where S_{MMC} is the rated power of the MMC. The energy to power ratio is typically selected in the range 10-50 J/kVA depending on the application [29].

An arm inductor selection principle under circulating current suppression control is proposed in [32]. Approaches presented in [29] and [31] do not consider circulating current control, but suggest a way to find the arm inductance based on circulating current resonance prevention. Typically, the arm inductor is selected as in (2.3) [31].

$$X_T + \frac{X_{arm}}{2} \approx 0.15 X_{base} \tag{2.3}$$

where X_T is the reactance of the link transformer, X_{arm} is the arm reactance of the MMC, and X_{base} is the converter base impedance. When looking from the AC side, the upper and lower arm inductances of the same phase are connected in parallel; thus, only half of the arm reactance is taken as the equivalent.

2.2 Control of MMC

MMC control basically consists of system level control, arm current control, and balancing control [16]. Control of real and reactive power comes under system control while arm current control includes circulating current suppression. Balancing control ensures that the voltages of submodule capacitors are kept close to the nominal value. There are several options to control power flow of the MMC including direct control and decoupled control. Also many techniques are proposed in the literature to control the circulating current. However, system control and circulating current suppression are not included in the scope of this thesis.

Since the switching pattern decides the submodule capacitor insertion in the arm, capacitor balancing and modulation schemes are interrelated. Therefore, it is essential to select an appropriate modulation technique to switch submodules before implementing a balancing algorithm. Capacitor voltage balancing based on different PWM techniques can be found in [33]–[36]. However, the main issue with high-frequency PWM methods is the increased amount of power losses. Therefore, low-frequency modulation techniques are proposed in many MMC applications [37]–[39]. Nearest level control (NLC) is one of such widely used low-frequency switching methods when a large number of arm submodules are used.

2.2.1 Nearest Level Control Modulation

The NLC technique produces the nearest voltage level that can be produced by switching submodule capacitors with respect to a given reference voltage waveform. The nearest output voltage level n is produced by rounding to a nearest voltage level as

$$n(t) = round\left(\frac{v_{ref}(t)}{E}\right) \tag{2.4}$$

where v_{ref} is the reference voltage waveform. The maximum possible error that can be occur due to this process is $E/2$. The produced waveform by NLC modulation takes the shape of a staircase as depicted in Figure 2.4.
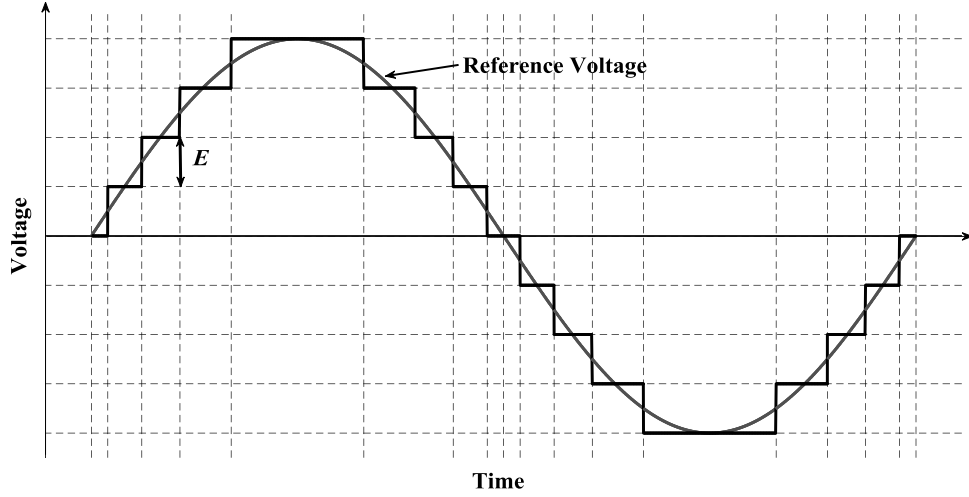
Figure 2.4 : Nearest level control modulation for $N = 8$

Since the maximum and minimum voltage levels that can be achieved by switching submodules are $+V_{dc}/2$ and $-V_{dc}/2$, it is important to maintain the reference voltage within these limits. Even though the number of voltage levels that can produced by N arm submodules is $N+1$, the actual number of voltage levels could be less than the maximum in case the magnitude of the reference voltage is less than $\left(\dfrac{V_{dc}}{2} - \dfrac{E}{2}\right)$. More about generating voltage reference is discussed in subsection 2.2.2.

There are other modulating techniques such as sinusoidal pulse-width modulation (SPWM), selective harmonic elimination (SHE), and space vector modulation (SVM). However, the simplicity of the concept and implementation make NLC popular in MMC applications. One flaw of this method is that harmonic contents are significant when the number of levels is small [39]. Therefore, it is recommended to practice NLC modulation only when the number of levels is large enough.

2.2.2 Generating the Voltage Reference

The output voltage of the MMC is a function of the DC voltage and expected to be sinusoidal. Therefore, a reference for the output voltage can be given as below.

$$v_{ref} = m \frac{V_{dc}}{2} \sin(\theta + \delta) \tag{2.5}$$

where m is the modulation index, θ is the phase angle, and δ is the power angle. Each arm must produce the voltage difference between the output voltage and the DC pole voltage it is connected to. Based on this reference, separate references for both the upper and lower arms can be written.

$$v_{ref}^{u} = \frac{V_{dc}}{2}\left(1 - m \sin(\theta + \delta)\right) \tag{2.6}$$

$$v_{ref}^{l} = \frac{V_{dc}}{2}\left(1 + m \sin(\theta + \delta)\right) \tag{2.7}$$

Subscript u and l stand for the upper and lower arms, respectively. In order to generate voltage waveforms properly, both reference signals require three input parameters.

1. **Modulation index (m):** The ratio between the phase voltage magnitude (peak) to half of the DC voltage is referred to as the modulation index. It is generated through a controller and is generally used to control the AC voltage magnitude or reactive power.

2. **Power angle (δ):** An MMC is normally connected to the AC system through a transformer at the point of common coupling (PCC). Power flow of the system can be handled by changing the phase angle at the converter output. Phase angle

difference between converter waveform and the phase angle at the PCC is referred to as δ. It can be used to control active power flow or DC bus voltage based on the converter requirement. A common practice is to control active power at the receiving end and DC voltage at the sending end in a VSC-HVDC system.

3. **Phase angle (θ):** When the MMC interfaces to the AC system, the converter output voltage must be shifted relative to a known reference point. This is achieved by measuring the instantaneous value of the voltage phase angle at the PCC by mean of a phase-locked loop (PLL). There are many PLL architectures in the literature. A PLL generates a ramp train between $[0,2\pi]$ whose value reflects the instantaneous phase angle of the tracking signal, in this case, the positive sequence of the ac waveform at fundamental frequency. Phase of the input signal is tracked by synchronizing with a targeted point (positive zero crossing or positive peak) of the signal.

The entire procedure of generating the reference voltage waveforms for the upper and lower arms can be summarised to a block diagram as shown in Figure 2.5. In this method modulating signals (m and δ) are generated directly from the system parameters for a given operating point. Even though this is very simple and effective in controlling system parameters, achieving secondary control objectives such as direct control of circulating current and average capacitor voltage is difficult in this method. Therefore, it is important to note that in general applications of MMCs controllers are implemented in rotating coordinates and modulation signals are generated in current regulation stage.
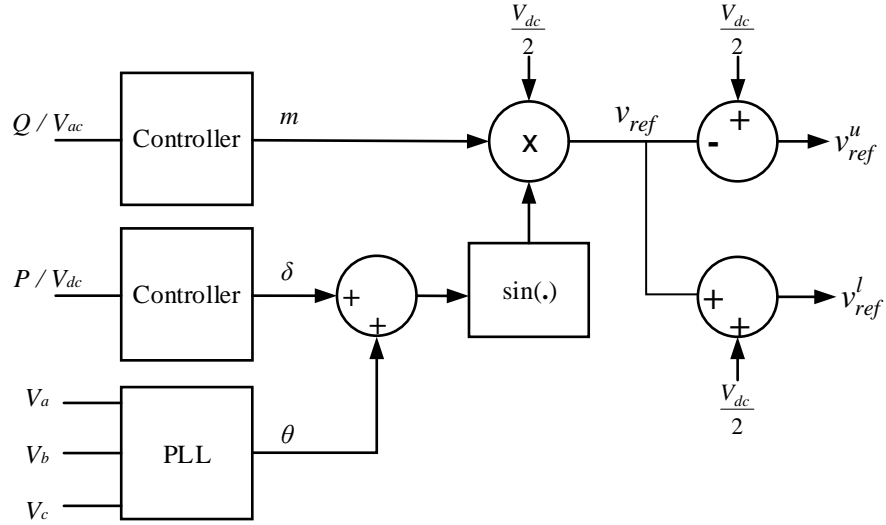
Figure 2.5 : Arm voltage reference waveforms generation

2.2.3   Capacitor Voltage Balancing

In an MMC, each submodule can be switched independently and selectively. Even though the modulation technique discussed in previous sections determines the number of submodules to be inserted to achieve a particular voltage, it does not provide any information about which submodule capacitors to insert or bypass. On the other hand, if the submodule capacitors are not utilized equally, some capacitors will charge or discharge more than the other capacitors, thus making capacitor voltages unequal. If a capacitor is bypassed, it will neither charge nor discharge. If a capacitor is inserted, the total arm current starts to flows through the capacitor, hence, charging or discharging it depending on the direction of the arm current. Therefore, a capacitor voltage balancing algorithm is necessary in order to select the inserted submodule capacitors in the MMC arm while maintaining capacitor voltages approximately equal. A block diagram of a capacitor voltage balancing algorithm starting from NLC modulation is illustrated in Figure 2.6.
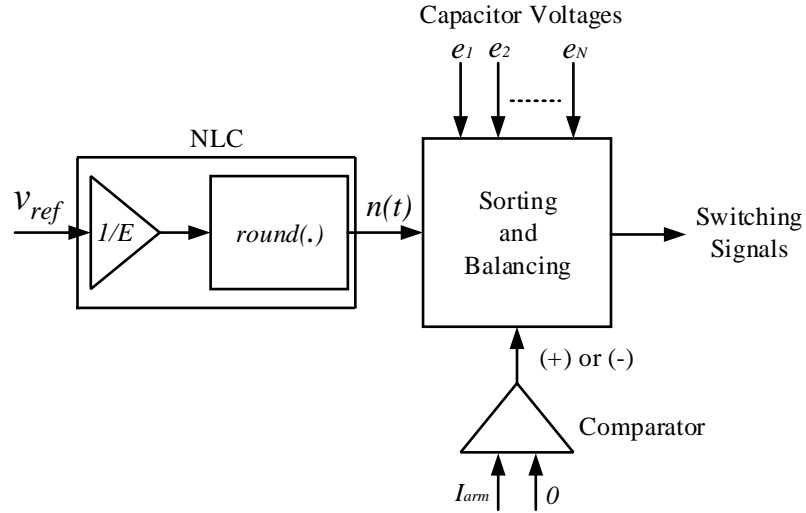
Figure 2.6 : MMC capacitor voltage balancing

Details about this capacitor balancing algorithm are available in [8], [37] and [40]. Firstly, the voltages of individual capacitors and the direction of arm current are measured in the beginning of each switching instant. Capacitors are then sorted and listed in ascending or descending order based on the magnitude of individual voltages. If the direction of arm current is positive ($I_{arm} > 0$), $n(t)$ number of submodule capacitors with lowest voltages are selected and inserted. If the arm current is in negative direction ($I_{arm} < 0$), $n(t)$ number of capacitors with highest voltages are selected and inserted. This balancing algorithm ensures that the capacitors with the lowest voltages are charged or capacitors with the highest voltages are discharged during each switching instant. Consequently, all capacitor voltages are balanced and maintained close to their nominal voltage value.

2.3   MMC Applications

Even though MMCs were initially designed for HVDC applications, their excellent performance compared to other VSC topologies have made them a promising technology for other applications such as medium-voltage motor drives and power quality applications as well. Details about the following applications are found in [1], [2], [7], [20].

1. **HVDC transmission systems:** Since MMCs are capable of providing high DC voltage levels and transfer power with increased efficiency, they are used in many HVDC bulk power transmission systems. Unlike traditional LLC systems, MMCs can change power flow direction without changing the DC voltage polarity. Therefore, MMCs can be used in multi-terminal HVDC systems and they allow to connect several HVDC systems forming an HVDC grid with improved controllability and reliability. Another MMC-HVDC application is found in offshore wind farm systems. The power generated in offshore wind farms is transmitted over long distances via submarine cables and then connected to an AC grid. MMCs have become a popular candidate in those application due to the benefits they offer in terms of efficiency and cost. Furthermore, an MMC's ability to supply islanded loads as the primary voltage source makes it more suitable in applications such as offshore wind interconnections since they require the black start capability. In addition to that, MMCs are used to connect two or more asynchronous AC systems using back-to-back schemes. Reduced filtering requirement allows to construct compact back-to-back power transfer stations.

2. **Medium-voltage motor drives:** MMCs can be found in variable-speed drives and regenerative energy sources as the line-side converter and in some marine applications as the motor-side converter. Also single-phase structures of MMCs are used in some traction applications as a power electronic transformer. In comparison with other medium-voltage drives, MMCs offer many advantages. Simplicity in voltage scalability and the modularity of structure require less engineering effort in construction. Redundancy can be achieved with less expense. Furthermore, dynamic performances can be improved by using high switching frequency compared to conventional drives. Most MMC medium voltage drives are available in the 2kV-8kV voltage range.

3. **Power quality applications:** One of the main advantages of using MMCs in power quality applications is that they can be connected to the grid without a transformer or filters due to their excellent harmonic and dynamic performances. Many studies have been carried out in this area, and it is expected that MMCs play key roles in the future. MMC-based STATCOMs are already developed and installed in order to compensate harmonics and reactive power demanded by distorted loads. It is investigated in literature to use MMCs in grid connection of large energy-storage systems. Another potential application of MMC is for grid integration of solar photovoltaic and wind energy systems. Unified power quality conditioners (UPQC) are another focus research area of MMC applications. It consists of two back-to-back connected MMCs, and is capable of providing series and parallel compensation, where the series compensation handles the voltage sag and swell problems in AC bus while the parallel compensation handles the power factor and harmonics problems that occur due to distorted loads.

2.4 Summary and Major Conclusions

A general overview of MMCs, which is important to understand the rest of this thesis, was given in this chapter. Basic circuit structure of a commonly used MMC topology and submodule structures were presented and their operation was explained. Modulation and capacitor voltage balancing are two major aspects of inner control systems, which ensure smooth operation of an MMC. A low-frequency switching technique referred to as nearest level control was explained. A capacitor voltage balancing algorithm based on sorting was presented. Then, several implemented and potentially viable MMC applications were discussed to show the importance and recent advancement of MMC.

As a conclusion, MMCs are a rapidly developing VSC topology with many benefits over traditional LLCs and other VSC topologies. In spite of all the advances made over the past decade, MMCs are still not the perfect converter that can be used in all power conversion applications. Therefore, continuous research has to be carried out in order to overcome challenges and technical barriers focusing various aspects of MMCs.

Chapter 3

Dynamic Phasor Principles

Dynamic phasors are essential tools in power electronic converter modeling; they use the quasi-periodic nature of converter waveforms to represent them as time-varying Fourier coefficients [11], [41], [42]. Dynamic phasor-based modeling looks at the average dynamics of current and voltage waveforms over a predefined length of time instead of looking at detailed or instantaneous behaviour of waveforms thus saving large computational burden and time compared to EMT simulators [43]. Another advantage of dynamic phasor-based modeling is that it gives the flexibility to model any selected number of harmonics for simulation purposes [11], [16], [18]. The user can select a larger time-step for dynamic phasor-based simulations if the accuracy required is less, thereby allowing use of multiple time-steps in EMT-dynamic phasor co-simulation applications [44]. The primary intention of dynamic phasor representation in power electronics is to model the slow dynamics of converters without paying attention to fast dynamics such as switching transients.

Generally, phasor analysis is a representation of periodic waveforms using complex numbers assuming that their magnitude and phase are constants [11], [42]. However, in transient analysis, both magnitude and phase of those signals change

over time. The dynamic phasor principle provides a method to represent quasi-periodic signals by approximating the magnitude and phase of signals within a fixed window, which is then slid over time. The time interval is usually chosen as the switching period of the particular system or converter [43], [45].

Other than power electronic converter modeling, dynamic phasor principles are successfully employed in areas such as modeling and analysis of power system dynamics and faults, modeling and analysing of electrical machines, and modeling of flexible ac transmission systems (FACTS) [41]. Before moving into the proposed model of an MMC, a mathematical review is necessary to understand the concept of dynamic phasors. Therefore, this section presents a detailed explanation of conventional dynamic phasor principle (CDP) and a recently developed dynamic phasor concept, which is based on fundamental frequency only.

3.1   Conventional Dynamic Phasors

3.1.1   Mathematical Principles

The use of generalised averaging method for power conversion circuits generally referred to as dynamic phasors is well described in [11] and [45]. Consider a quasi-periodic signal $x(t)$ over the time interval $(t\text{-}T, t\,]$, the Fourier series of $x(t)$ is given by

$$x(t - T + s) = \sum_{k=-\infty}^{+\infty} \langle x \rangle_k (t) e^{jk\frac{2\pi}{T}(t-T+s)}$$

(3.1)

where, $s \in (t\text{-}T, t\,]$ and integer k is the order of the harmonic. T is the period of the signal $x(t)$. The Fourier coefficient $\langle x \rangle_k (t)$ is a time-dependent complex value as the

time interval under consideration slides over time; therefore, it is referred to as a dynamic phasor of $x(t)$ [41], [45], [46]. It represents the time-varying magnitude and phase of kth harmonic of $x(t)$ with angular frequency of $k.2\pi/T$. The value of $\langle x \rangle_k(t)$ is given by

$$\langle x \rangle_k(t) = \frac{1}{T}\int_0^T x(t-T+s)e^{-jk\frac{2\pi}{T}(t-T+s)}ds \qquad (3.2)$$

It is important to note that the formulation of (3.1) using (3.2) requires large number of repetitive integrations accumulating considerable computational burden. Therefore, in order to obtain a proper approximation (with arbitrary accuracy), (3.1) can be modified as

$$x(t) \approx \sum_{k=-n}^{+n} \langle x \rangle_k(t)e^{jk\frac{2\pi}{T}(t-T+s)} \qquad (3.3)$$

The value of n is chosen based on the required level of accuracy. When n approaches infinity as in (3.1), the error of approximation approaches zero at the expense of increased computations [46]. A major drawback of the CDP is that it becomes inefficient when modeling systems consisting of a large number of harmonics as the dynamic phasor of each harmonic needs to be considered separately.

3.1.2   Properties of Conventional Dynamic Phasors

The following properties of dynamic phasors are useful in modeling applications.

1. **Differentiation**: The time-derivative of the kth Fourier coefficient of $x(t)$ can be calculated as

$$\frac{d}{dt}\langle x \rangle_k(t) = \left\langle \frac{d}{dt}x \right\rangle_k(t) - jk\frac{2\pi}{T}\langle x \rangle_k(t) \qquad (3.4)$$

In most circumstances, dynamic systems are represented using first-order differential equations; thus, the relationship given in (3.4) is useful when calculating individual dynamic phasors of such systems for each frequency. However, for a non-linear system, it is difficult to evaluate the right-hand side of (3.4) using a finite number of operations. Therefore, approximations need to be made to model such systems using dynamic phasors.

2. **Convolution**: If the right-hand side of (3.4) is a polynomial, it can be written as an explicit function of individual dynamic phasor quantities using the following convolution relationship [45]. Consider two signals $x(t)$ and $y(t)$; dynamic phasors of product of the two signals are given by

$$\langle x.y \rangle_k = \sum_{i=-\infty}^{+\infty}\langle x \rangle_{k-i}\langle y \rangle_i \qquad (3.5)$$

Since higher order harmonics are often negligibly small in most of the applications, the above infinite series can be approximated with a finite series by considering only the most dominant components[45].

3. **Complex Conjugate**: Another property proven to be useful when modeling with dynamic phasors is complex conjugate. Calculation of positive-frequency dynamic phasor coefficients is adequate since any negative-frequency dynamic phasor coefficient is obtained as the complex conjugate of the positive-frequency dynamic phasor coefficient of the same order; i.e.,

$$\langle x \rangle_{-k}(t) = \langle x \rangle_k^*(t) \tag{3.6}$$

where $*$ denotes complex conjugate.

3.2   Base-Frequency Dynamic Phasors

Base-frequency dynamic phasor (BFDP) is a recently developed concept to model and simulate electrical networks by interfacing to an EMT simulator. This method allows to write all the harmonics, including dc, in terms of the fundamental dynamic phasor component. The main principles behind this method are explained and presented in [44], [47]. The goal of this section is to explain the mathematical concept and advantages of BFDP.

3.2.1   Mathematical Concept

The theory that explains the BFDP starts with the conventional method. Equation (3.1) can be modified as a series of explicitly real values as below.

$$x(t - T + s) = \langle x \rangle_0(t) + 2\,\mathrm{Re}\left(\sum_{k=1}^{+\infty} \langle x \rangle_k(t) e^{jk\frac{2\pi}{T}(t-T+s)}\right) \tag{3.7}$$

As pointed out in Section 3.1, (3.7) represents each harmonic with a distinct dynamic phasor coefficient. However, (3.7) can be reorganized to represent all the harmonics and the dc component as a term at the fundamental frequency as shown below.

$$x(t-T+s) = \mathrm{Re}\left(\left(\langle x\rangle_0(t)e^{-j\frac{2\pi}{T}(t-T+s)} + 2\sum_{k=1}^{+\infty}\langle x\rangle_k(t)e^{j(k-1)\frac{2\pi}{T}(t-T+s)}\right)e^{j\frac{2\pi}{T}(t-T+s)}\right) \quad (3.8)$$

The term that represents all the harmonics and the dc value is defined as the BFDP, $\langle X\rangle_B$, as below. Henceforth in this thesis, the notation $\langle\cdot\rangle_B$ denotes the BFDP of corresponding signal.

$$\langle X\rangle_B(t) = \langle x\rangle_0(t)e^{-j\frac{2\pi}{T}(t-T+s)} + 2\sum_{k=1}^{+\infty}\langle x\rangle_k(t)e^{j(k-1)\frac{2\pi}{T}(t-T+s)} \quad (3.9)$$

An approximation to the right-hand side of (3.9) can be made by deciding on the most relevant values of integer k based on the required level of accuracy. A signal represented in BFDP can be converted to a time-domain signal using the following equation.

$$x(t) = \mathrm{Re}\left(\left(\langle X\rangle_B(t)\right)e^{j\frac{2\pi}{T}t}\right) \quad (3.10)$$

Since all the harmonic components are amalgamated in one component in this method, the convolution property of the conventional method is no longer directly applicable. Therefore, a new expression to find the BFDP of the product of two signals $x(t)$ and $y(t)$ must be obtained starting from the basic definition as follows.

$$\langle x\ y\rangle_B(t) = \sum_{i=-\infty}^{+\infty}\langle x\rangle_i\langle y\rangle_{-i}e^{-j\frac{2\pi}{T}t} + 2\sum_{h=1}^{+\infty}\left(\sum_{i=-\infty}^{+\infty}\langle x\rangle_i\langle y\rangle_{h-i}\right)e^{j(h-1)\frac{2\pi}{T}t} \quad (3.11)$$

As in the definition of BFDP method, the first term of the right-hand side presents the dc component of the product and the second term provides the remaining

30

harmonic components. In most power system applications, at least one of the two waveforms is nearly sinusoidal; hence, its higher order harmonics may be ignored. Therefore, an approximation can be made to estimate $\langle xy \rangle_B$ as shown in (3.12). If it is assumed that the signal $x(t)$ is a nearly sinusoidal, then

$$
\begin{aligned}
\langle x\ y \rangle_B (t) = & \left(\langle x \rangle_{-1} \langle y \rangle_1 + \langle x \rangle_1 \langle y \rangle_{-1} \right) e^{-j\frac{2\pi}{T}t} \\
& + 2\sum_{h=1}^{+\infty} \left(\langle x \rangle_{-1} \langle y \rangle_{h+1} + \langle x \rangle_1 \langle y \rangle_{h-1} \right) e^{j(h-1)\frac{2\pi}{T}t}
\end{aligned}
\tag{3.12}
$$

When the product does not have a dc component, the first term on the right-hand side will vanish and the equation can be further simplified only to the second term. In order to solve the second term, only non-zero harmonic components need to be considered for h to avoid unnecessary calculations. The time-derivative of BFDP follows the same property as in conventional method.

3.2.2   Efficient EMT to BFDP Conversion

When a dynamic phasor model is interfaced with an EMT solver, only the instantaneous values of present and past time-steps of voltage and current signals are available. A straightforward way of converting EMT signal to BFDP is to use (3.9). It demands the dynamic phasors corresponding to each individual harmonic, which have to be calculated using (3.2) by integrating over the past cycle as in the CDP method. If the signal consists of a large number of harmonics, this will require several integrations in order to accurately represent the signal using dynamic phasors. This will result in increased computational intensity thus reducing the speed of simulations and one will find no advantage for BFDP over CDP. In order to make this

process efficient, an alternative method, which only needs one integration is discussed below. Details of this new algorithm are first proposed in [44] and [47] and are compatible only with BFDP.

Figure 3.1 illustrates the steps of augmentation of the base-frequency component using a given EMT signal.
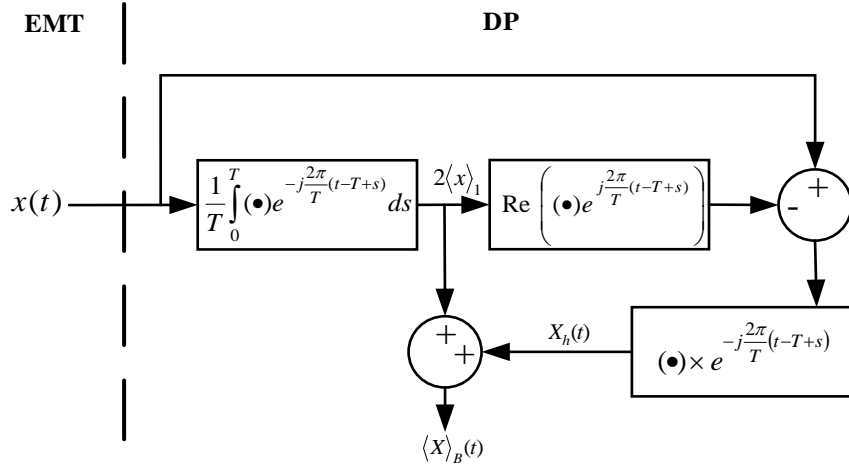
Figure 3.1 : EMT to BFDP conversion

Consider the signal $x(t)$ over the time interval $[t\text{-}T, t]$; the Fourier series of $x(t)$ is given in (3.1). One can express the same series separating the fundamental component of the signal as

$$x(t - T + s) = 2\,\mathrm{Re}\!\left(\langle x \rangle_1(t)e^{j\frac{2\pi}{T}(t-T+s)}\right) + \sum_{k=-\infty,k\neq-1,1}^{+\infty}\langle x \rangle_k(t)e^{jk\frac{2\pi}{T}(t-T+s)} \qquad (3.13)$$

The second term on right-hand side has all the frequency components including dc except the fundamental. This equation can be rearranged to represent harmonic contents of the second term at the fundamental frequency as follows.

$$x(t-T+s) = 2\operatorname{Re}\left(\langle x \rangle_1(t)e^{j\frac{2\pi}{T}(t-T+s)}\right) + \underbrace{\left(\sum_{k=-\infty,k\neq-1,1}^{+\infty}\langle x \rangle_k(t)e^{j(k-1)\frac{2\pi}{T}(t-T+s)}\right)}_{X_h(t)}e^{j\frac{2\pi}{T}(t-T+s)} \qquad (3.14)$$

The dynamic phasor of fundamental component, $\langle x \rangle_1$, can be calculated using (3.2) with $k = 1$ as depicted in Figure 3.1 and the left-hand side is available from the EMT solver. Using (3.14), one can define a new variable, $X_h(t)$, that includes all the frequency components plus the dc component but without the fundamental in the frame of the fundamental frequency.

$$X_h(t) = \left(x(t-T+s) - 2\operatorname{Re}\left(\langle x \rangle_1(t)e^{j\frac{2\pi}{T}(t-T+s)}\right)\right)e^{-j\frac{2\pi}{T}(t-T+s)} \qquad (3.15)$$

Now, the base-frequency term of the EMT waveform can be obtained by augmenting $X_h(t)$ with the already calculated fundamental component.

$$\langle X \rangle_B(t) = X_h(t) + 2\langle x \rangle_1 \qquad (3.16)$$

This procedure prevents the calculation of individual harmonic components using repetitive manipulation of (3.2) to yield $\langle X \rangle_B$ as in (3.9) and, hence, reduces a great deal of computational complexity.

3.2.3   Advantages over Conventional Method

The actual advantage of modeling with BFDP mostly depends on the application. Many applications may find convenience in modeling with the conventional method rather than modeling with BFDP in steady state. However, when it comes to transient simulation, there is no guarantee that all the dynamics can be accurately modeled

using one or two harmonic components. In fact, network transients may include much high-frequency content as well as a dc component. Hence, BFDP modeling and simulation offers noteworthy advantages over the conventional method in dynamic phasor-EMT co-simulation applications.

As highlighted earlier in the thesis, one of the main advantages of using BFDP is that it has the ability to capture important high-frequency contents of the network; in fact, the entire spectrum of harmonics of the network can be captured and then represented using a single dynamic phasor quantity. As a result, it delivers a scheme to reproduce a large number of harmonics in steady state and transient solution of the network similar to the extended-frequency content in CDP. If an adequately small time-step is used in simulations, all the harmonic contents and fast transients can be retained in the network solution. It is important to note that all these additional advantages come through the significant reduction in computational burden and complexity and hence well enhance simulation speed.

3.3 Modeling and Simulation with Dynamic Phasors – An Example

Dynamic phasor modeling and simulation can be further illustrated using a general example. Therefore, modeling of a controlled six-pulse thyristor converter using both dynamic phasor methods is presented in this section and comparisons are made to understand the advantages and disadvantages of the two methods. Simulation results are compared with results obtained from implementing the same circuit in PSCAD/EMTDC EMT simulator. Figure 3.2 and Figure 3.3 show the circuit diagram

and voltage waveforms of a three-phase controlled rectifier constructed using thyristors.
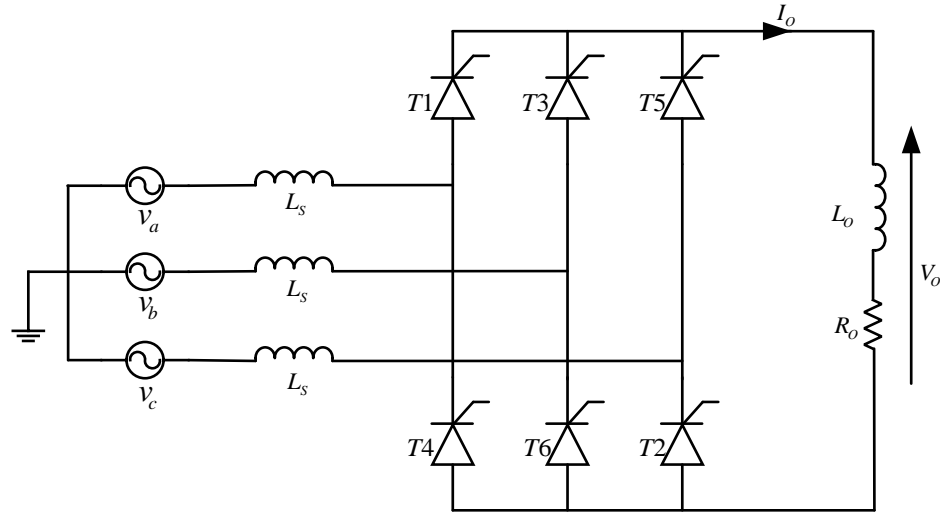
Figure 3.2: Circuit diagram of six-pulse thyristor converter
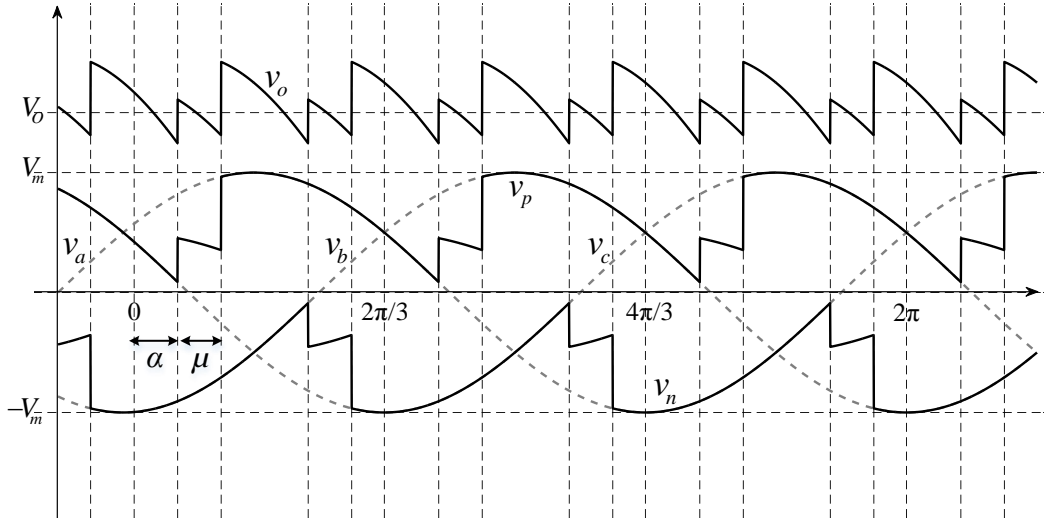
Figure 3.3: Voltage waveforms of six-pulse thyristor converter

The AC side of the converter is connected to an ideal three-phase source with a source side inductance L_S included in each phase. The DC side is configured as an inductor L_O and resistor R_O. The operation of the six-pulse thyristor converter can be briefed with the help of its voltage waveforms.

The six thyristors of the converter can be divided into two parts. The positive half consists of thyristors T_1, T_3, and T_5 while the negative half consists of thyristors T_2, T_4, and T_6. At any given time, only one thyristor from each half conducts except during commutation. Due to the effect of the source-side inductance, thyristors cannot turn on or off instantaneously; thus, the thyristor turning on and the thyristor turning off in the same half converter start conducting simultaneously resulting in commutation overlap between two phases. During commutation, the voltage is the average of the corresponding two phases. The angle difference between the beginning and the end of each commutation is called the overlap angle, μ.

$$\mu = \cos^{-1}\left(\cos(\alpha) - \frac{2\omega L_S I_o}{\sqrt{2}\,V_{LL}} \right) - \alpha \tag{3.17}$$

where V_{LL} is the line to line rms voltage and α is the firing angle. When the magnitude of a particular phase comes to be the highest among the three phases, the thyristor of the positive half of the same phase becomes forward biased and ready to conduct. It will start conducting as soon as it receives the firing command on its gate. The same happens in the negative half of the converter when the phase voltage becomes the lowest among the three phases. The angle difference between the time it becomes forward biased and the time it receives its gate signal is called the firing angle α and is taken as a controlled input.

The approach used to model this kind of power electronic converter using dynamic phasors is based on switching functions. A switching function is mainly characterized using the thyristor switching explained in the previous two paragraphs and provides the mathematical relationship between input and output. An illustrative diagram of the voltage switching functions for each phase of the example is shown in Figure 3.4.
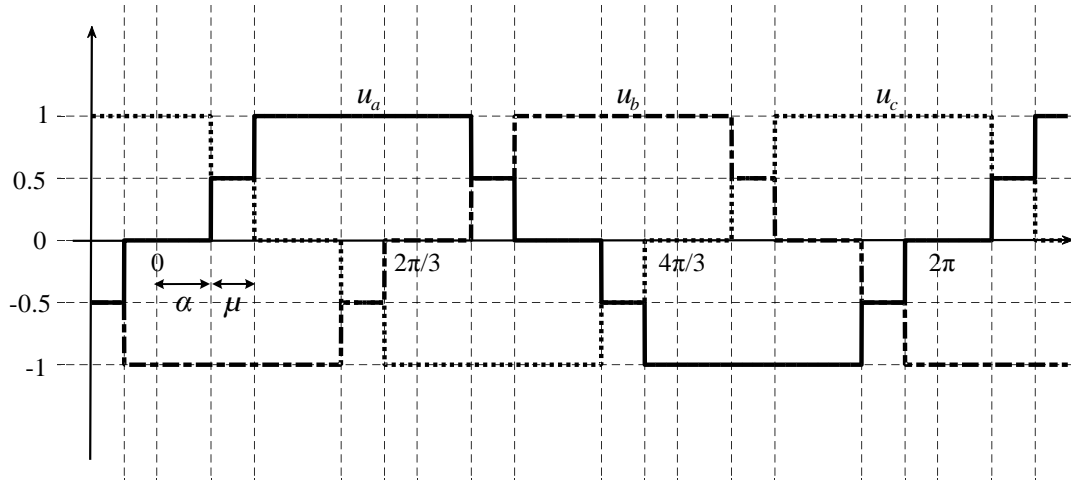
Figure 3.4 : Voltage switching functions of 3-phase thyristor converter

The output voltage of the converter can be expressed using switching functions and AC voltages as below.

$$v_o = u_a v_a + u_b v_b + u_c v_c \qquad (3.18)$$

Now, the dynamics of the output can be obtained by applying Kirchhoff's voltage law to the DC side.

$$\frac{d\,i_o}{dt} = -\frac{R_o}{L_o} i_o + \frac{1}{L_o} v_o \qquad (3.19)$$

This equations provides sufficient information to model the output dynamics of the converter by applying dynamic phasor principles discussed in this chapter.

3.3.1 Modeling with Conventional Dynamic Phasors

By applying dynamic phasor operations to (3.18) and (3.19), the following equations can be found.

$$\frac{d \langle i_o \rangle_k}{dt} = -\left(j\omega_o k + \frac{R_o}{L_o} \right)\langle i_o \rangle_k + \frac{1}{L_o} \langle v_o \rangle_k \tag{3.20}$$

$$\langle v_o \rangle_k = \langle u_a v_a \rangle_k + \langle u_b v_b \rangle_k + \langle u_c v_c \rangle_k \tag{3.21}$$

where ω_0 is the fundamental angular frequency. The AC voltage is assumed to be purely sinusoidal and only the base-frequency component exists. Therefore, the dynamic phasor of $v_{a,b,c}$ can be found using (3.2) with $k = 1$. Switching functions have the harmonics of order 1, 5, 7, 11, 13, 17… etc. The dynamic phasor quantity of kth frequency component of the switching function is given by

$$\langle u_x \rangle_k (t) = \frac{-je^{-jk(\alpha - \phi_x)}}{2\pi k}\left(1 + e^{-jk\mu}\right)\left(1 - e^{-jk2\pi/3}\right) \tag{3.22}$$

Phase angle ϕ_x must be selected as 0, -2π/3, +2π/3 for phase a, b, and c, respectively. The output voltage is made of the dc term and multiples of 6th order harmonics. It is understood from (3.20) that one has to solve a separate state equation to model each individual harmonic considered. For example, if one considers six harmonic components, i.e. $k = 0$, 6, 12, 18, 24, and 30, then the system consists of the following six separate state equations.

$$\frac{d\langle i_o\rangle_0}{dt} = -\frac{R_o}{L_o}\langle i_o\rangle_0 + \frac{1}{L_o}\langle v_o\rangle_0$$

$$\frac{d\langle i_o\rangle_6}{dt} = -\left(j6\omega_o + \frac{R_o}{L_o}\right)\langle i_o\rangle_6 + \frac{1}{L_o}\langle v_o\rangle_6$$

$$\vdots \qquad\qquad \vdots \qquad\qquad \vdots$$

$$\frac{d\langle i_o\rangle_{30}}{dt} = -\left(j30\omega_o + \frac{R_o}{L_o}\right)\langle i_o\rangle_{30} + \frac{1}{L_o}\langle v_o\rangle_{30} \qquad (3.23)$$

Each equation (except the one corresponding to the dc component) must be separated to real and imaginary parts before going into the numerical integration. This nearly doubles the number of state equation to be solved. More about solving state equations by means of numerical integrations is discussed in subsection 4.1.4. After obtaining the solutions the time-domain equation of output current can be obtained as (3.3).

3.3.2 Modeling with Base-Frequency Dynamic Phasors

Modeling with BFDP follows the same steps as in conventional method. By applying the BFDP principle to the converter equations one obtains the following.

$$\frac{d\langle i_o\rangle_B}{dt} = -\left(j\omega_o + \frac{R_o}{L_o}\right)\langle i_o\rangle_B + \frac{1}{L_o}\langle v_o\rangle_B \qquad (3.24)$$

$$\langle v_o\rangle_B = \langle u_a v_a\rangle_B + \langle u_b v_b\rangle_B + \langle u_c v_c\rangle_B \qquad (3.25)$$

Since all the frequency components including dc of the output current is represented by $\langle i_o\rangle_B$, taking solution of (3.24) yields the output waveform. Unlike the conventional method, this method has only one state equation to integrate using an appropriate numerical method, yet it is able to produce many harmonics components.

Numerical integration shares a significant proportion of computational complexity; therefore, this method brings large computational advantage over the traditional method.

Computation of $\langle v_o \rangle_B$ is challenging since it has three multiplication terms. But it can be estimated using (3.12) as the source voltages are assumed to be purely sinusoidal. It is up to the user to decide how many harmonics components of the switching functions to be considered based on the accuracy requirement.

$$\langle u_x v_x \rangle_B (t) = \left(\langle v_x \rangle_{-1} \langle u_x \rangle_1 + \langle v_x \rangle_1 \langle u_x \rangle_{-1} \right) e^{-j\frac{2\pi}{T}t}$$
$$+ 2 \sum_{h=6,12,..}^{+30} \left(\langle v_x \rangle_{-1} \langle u_x \rangle_{h+1} + \langle v_x \rangle_1 \langle u_x \rangle_{h-1} \right) e^{j(h-1)\frac{2\pi}{T}t} \qquad (3.26)$$

where $x = a, b, c$. Finally the time-domain solution is obtained as in (3.10).

3.3.3   Simulation Results

The circuit shown in Figure 3.2 is constructed in PSCAD/EMTDC simulator and the results are compared with the both dynamic phasor solutions obtained by modeling the same circuit in MATLAB. Both steady state results and dynamic responses are compared with PSCAD/EMTDC results to have an understanding of the accuracy of two dynamic phasor models. Then the time taken for two dynamic phasor solutions are compared. Case parameters selected for the simulation are listed below in Table 3-1.

Table 3-1 : Thyristor converter parameters

Parameter	Value
V_{LL}	230 V
f_o	60 Hz
L_S	0.01 H
L_L	0.1 H
R_L	10 Ω

Figure 3.5 and Figure 3.6 illustrate the comparison of output current and voltage with PSCAD/EMTDC results for different choices of selected harmonics. As the first case, only two components (k = 0 and 6) are included in dynamic phasors. Simulation is started with a firing angle α of 15° and it is then suddenly changed to 30° at t = 0.25 s. Then, the same observation is done capturing all harmonics up to 30 (k = 0, 6, 12, 18, 24, 30) of the dynamic phasor models.
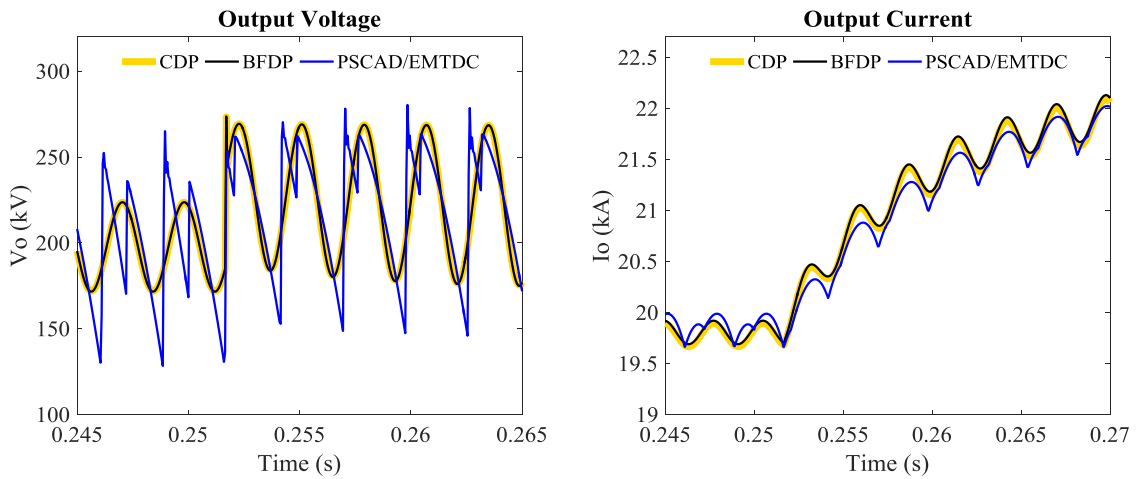
Figure 3.5 : Comparison of six-pulse thyristor converter waveform considering harmonics up to 6th order (k = 0 and 6)
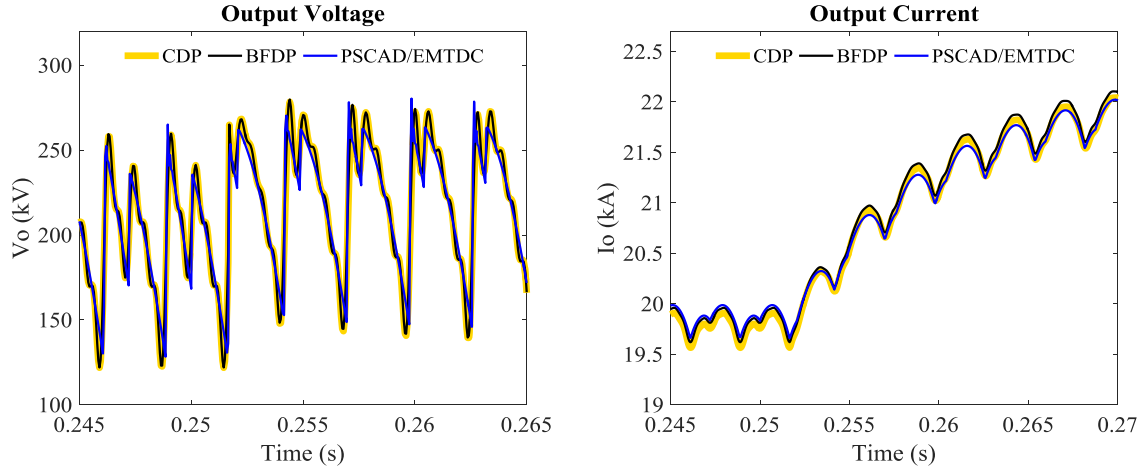
Figure 3.6 : Comparison of six-pulse thyristor converter waveform considering harmonics up to 30th order (k = 0, 6, 12, 18, 24 and 30)

The results prove that the error between dynamic phasor models and PSCAD/EMTDC results are higher when a small number of harmonics are modeled. Even though both voltage and current follow the same dynamic pattern, the shape of steady state and dynamic response waveforms are not matching. This is due to the fact that the PSCAD waveform provides the full harmonic spectrum of the waveform, thus, reconstructing dynamic phasor waveforms without considering high frequency components creates a marked difference between the waveforms. However, the accuracy of dynamic phasor results in both steady state and transients seems to have a good agreement with PSCAD/EMTDC results when a larger number of harmonics are modeled.

Another necessary observation is that the accuracy of BFDP and CDP seems to be the same since both are modeled using the same number of harmonics in each case. The difference between the two dynamic phasor models can be readily understood by a simulation speed comparison as in Figure 3.7. The time taken to acquire each dynamic phasor solution with respect to the number of harmonics used to reconstruct

the waveforms are compared. Simulations are carried out using MATLAB and the firing angle is maintained at 30° during the entire simulation.
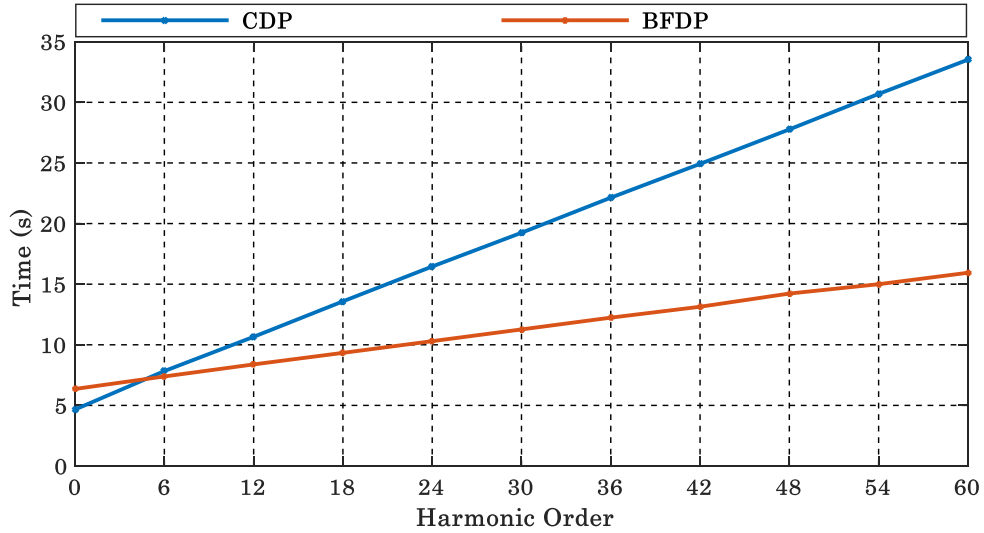
Figure 3.7 : Time taken for dynamic phasor simulations in MATLAB

When the solutions only include the dc component, CDP method is faster than the BFDP solution. It is because in CDP the system has only one state equation to solve since the dc component consists of real values. However, when the dc component is written in terms of BFDP, it consists of real and imaginary parts; consequently, there are two state equations to solve. However, in CPD the number of state equations keep increasing with the number of considered harmonics while BFDP always gives the solution using two state equations. Therefore, BFDP is always ahead of the CPD in speed when the number of modelled harmonics is high as witnessed in Figure 3.7.

3.4   Summary and Major Conclusions

A review of the traditional dynamic phasor technique and a recently developed method known as base-frequency dynamic phasor was presented. The first method involves modeling individual harmonics separately while the new method shows all the harmonics in terms of the base frequency. Mathematical principles, properties, and general benefits and drawbacks of both methods were discussed. A case of six-pulse thyristor rectifier was used to demonstrate the dynamic phasor modeling process and comparison of results were made against a detailed transient simulation model. Practice of BFDP or CDP depends on the application. BFDP gives noteworthy advantage over CDP in terms of computations and simulation speed when modeling higher number of harmonics. An efficient algorithm to convert EMT waveforms to BFDP for such applications was also presented in this chapter.

Chapter 4

New Dynamic Phasor Model of an MMC and DP-EMT Interfacing

Development of an extended-frequency dynamic phasor model of an MMC and interfacing the developed model with EMT simulator are two of the main objectives of this thesis. Comprehensive explanation of this procedure is presented in this chapter. Focus in Section 4.1 is on derivation of fundamental mathematical equations of an MMC and applying dynamic phasor principles. Then the proposed MMC model and interfacing it with the rest of the electrical network built in an EMT simulator are discussed in Section 4.2.

4.1   Mathematical Model of an MMC

Circuit diagrams of a general phase of an MMC and submodules of the upper and lower arms are depicted in Figure 4.1, where $x = a, b, c$ refers to a phase.
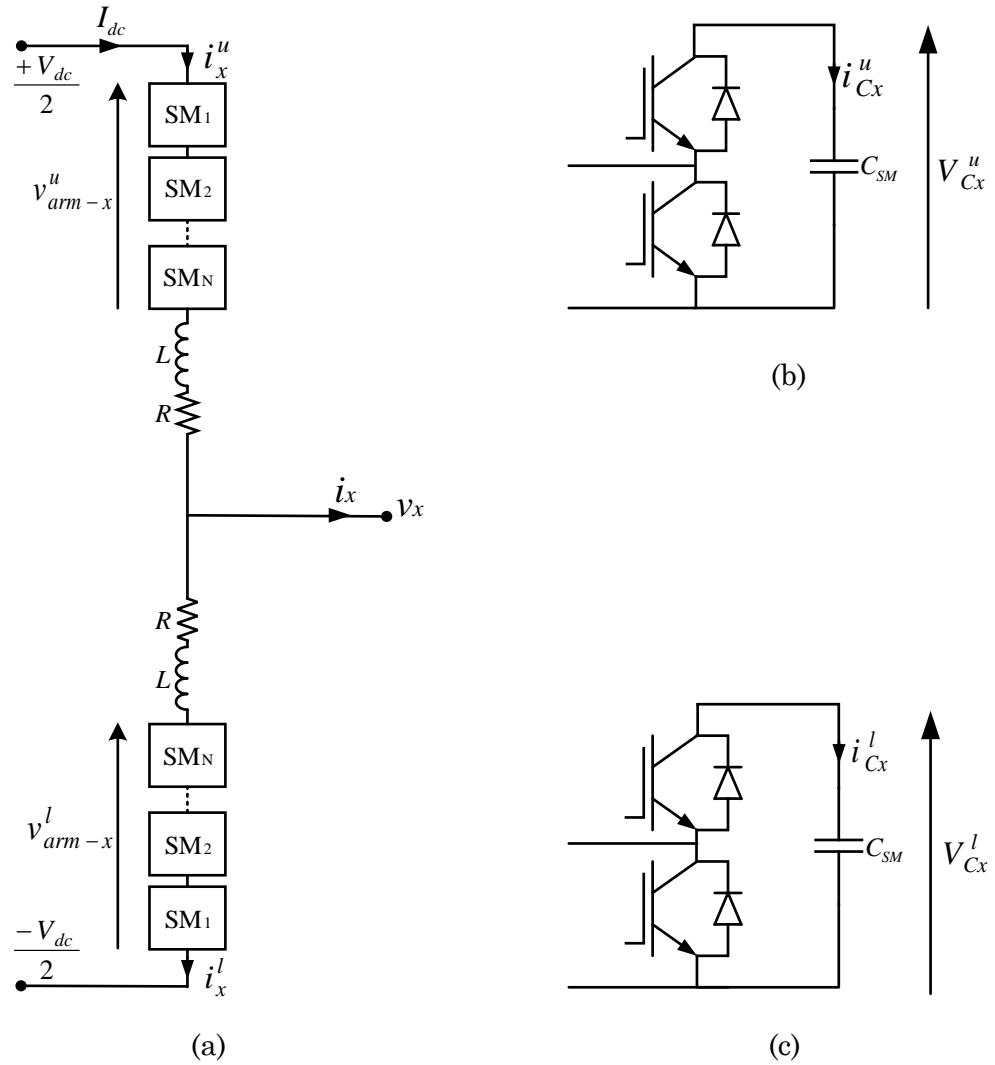
Figure 4.1 : Circuit diagrams of (a) General phase of MMC, (b) Upper arm submodule, (c) Lower arm submodule

4.1.1　Time-Domain Dynamic Equations of an MMC

Derivation of the governing equations of the MMC can commence by applying Kirchoff's voltage law to the upper arm and lower arm separately.

$$L\frac{d}{dt}i_x^u = V_{dc} - v_{arm-x}^u - R\,i_x^u - v_x \tag{4.1}$$

$$L\frac{d}{dt}i_x^l = V_{dc} - v_{arm-x}^l - R\,i_x^l + v_x \tag{4.2}$$

Note that the subscripts u and l stand for the upper arm and lower arm variables, respectively. v_{arm-x}^u and v_{arm-x}^l represent the total voltage across all the submodules of the upper and lower arms and are given by

$$v_{arm-x}^u = S_x^u V_{Cx}^u \tag{4.3}$$

$$v_{arm-x}^l = S_x^l V_{Cx}^l \tag{4.4}$$

where $S_x^{u,l}$ are arm switching functions of the MMC and characterise the number of capacitors turned on in each arm during each switching state. Switching functions perform a vital role in MMC modeling applications; hence, a detailed description of switching functions used in this model is carried out in subsection 4.1.3.

Another two equations can be derived by applying Kirchoff's current law to the upper and lower arm individual submodules.

$$C_{SM}\frac{d}{dt}V_{Cx}^u = i_{Cx}^u \tag{4.5}$$

$$C_{SM}\frac{d}{dt}V_{Cx}^l = i_{Cx}^l \tag{4.6}$$

Submodule currents, $i_{Cx}^{u,l}$, depend on the on/off state of the submodule at a given time; therefore, they can be written as a function of switching function and arm current. The number of submodules per arm is denoted by N.

$$i_{Cx}^{u} = \frac{S_{x}^{u}}{N} i_{x}^{u} \qquad (4.7)$$

$$i_{Cx}^{l} = \frac{S_{x}^{l}}{N} i_{x}^{l} \qquad (4.8)$$

Even though, it is not a direct requirement for modeling process, it is essential to have awareness about the content of arm currents when deciding on harmonic contents to be retained. Therefore, it is important to consider the following two equations.

$$i_{x}^{u} = \frac{I_{dc}}{3} + \frac{i_{x}}{2} + i_{cir-x} \qquad (4.9)$$

$$i_{x}^{l} = \frac{I_{dc}}{3} - \frac{i_{x}}{2} + i_{cir-x} \qquad (4.10)$$

where i_{cir-x} is the circulating current flowing through the arm, which comprises of second order harmonics. The above two equations are accurate under the assumption that all three phases are well balanced. After going through all equations, the following four equations can be derived combining (4.1)-(4.8).

$$\frac{d}{dt} V_{Cx}^{u} = \frac{S_{x}^{u}}{C_{SM} N} i_{x}^{u} \qquad (4.11)$$

$$\frac{d}{dt} V_{Cx}^{l} = \frac{S_{x}^{l}}{C_{SM} N} i_{x}^{l} \qquad (4.12)$$

$$\frac{d}{dt} i_{x}^{u} = \frac{V_{dc}}{2L} - \frac{1}{L} S_{x}^{u} V_{Cx}^{u} - \frac{R}{L} i_{x}^{u} - \frac{1}{L} v_{x} \qquad (4.13)$$

$$\frac{d}{dt} i_{x}^{l} = \frac{V_{dc}}{2L} - \frac{1}{L} S_{x}^{l} V_{Cx}^{l} - \frac{R}{L} i_{x}^{l} + \frac{1}{L} v_{x} \qquad (4.14)$$

Equations (4.11)-(4.14) give sufficient information to characterise the dynamics of an MMC. For analytical and mathematical convenience, instead of taking the upper and lower arms separately, these equations are re-written in terms of new variables defined by taking the summation and difference of the upper and lower arm variables.

$$\frac{d}{dt}V_{Cx}^s = \frac{1}{2NC_{SM}}(S_x^s i_x^s + S_x^d i_x^d) \tag{4.15}$$

$$\frac{d}{dt}V_{Cx}^d = \frac{1}{2NC_{SM}}(S_x^s i_x^d + S_x^d i_x^s) \tag{4.16}$$

$$\frac{d}{dt}i_x^s = -\frac{1}{L}\left(\frac{1}{2}S_x^s V_{Cx}^s + \frac{1}{2}S_x^d V_{Cx}^d + Ri_x^s - V_{dc}\right) \tag{4.17}$$

$$\frac{d}{dt}i_x^d = -\frac{1}{L}\left(\frac{1}{2}S_x^s V_{Cx}^d + \frac{1}{2}S_x^d V_{Cx}^s + Ri_x^d - v_x\right) \tag{4.18}$$

Subscript s is used to denote summation and d is used to denote difference of the upper and lower arm variables. Using (4.9) and (4.10), it is seen that the difference of arm currents gives the line current i_x on the AC side.

$$i_x^s = \frac{2}{3}I_{dc} + 2i_{cir-x} \tag{4.19}$$

$$i_x^d = i_x \tag{4.20}$$

In the proposed model of an MMC discussed in Section 4.2, i_x is available as an input measurement from the EMT simulator at the AC side dynamic phasor-EMT interface. Therefore, V_{Cx}^s, V_{Cx}^d, and i_x^s are used as state variables while (4.18) is used to determine the phase voltage, v_x. A small number of state variables is always beneficial since it increases the system speed when solving the system.

4.1.2 Dynamic Phasor Equations of an MMC

The following dynamic phasor equations can be found by applying properties of dynamic phasor to (4.15)-(4.18).

$$\frac{d}{dt}\left\langle V_{Cx}^{s}\right\rangle_{k} = \frac{1}{2NC_{SM}}\left(\sum_{i=-\infty}^{+\infty}\left\langle S_{x}^{s}\right\rangle_{k-i}\left\langle i_{x}^{s}\right\rangle_{i} + \sum_{i=-\infty}^{+\infty}\left\langle S_{x}^{d}\right\rangle_{k-i}\left\langle i_{x}^{d}\right\rangle_{i}\right) - jkw_{o}\left\langle V_{Cx}^{s}\right\rangle_{k} \qquad (4.21)$$

$$\frac{d}{dt}\left\langle V_{Cx}^{d}\right\rangle_{k} = \frac{1}{2NC_{SM}}\left(\sum_{i=-\infty}^{+\infty}\left\langle S_{x}^{s}\right\rangle_{k-i}\left\langle i_{x}^{d}\right\rangle_{i} + \sum_{i=-\infty}^{+\infty}\left\langle S_{x}^{d}\right\rangle_{k-i}\left\langle i_{x}^{s}\right\rangle_{i}\right) - jkw_{o}\left\langle V_{Cx}^{d}\right\rangle_{k} \qquad (4.22)$$

$$\frac{d}{dt}\left\langle i_{x}^{s}\right\rangle_{k} = -\frac{1}{2L}\left(\sum_{i=-\infty}^{+\infty}\left\langle S_{x}^{s}\right\rangle_{k-i}\left\langle V_{Cx}^{s}\right\rangle_{i} + \sum_{i=-\infty}^{+\infty}\left\langle S_{x}^{d}\right\rangle_{k-i}\left\langle V_{Cx}^{d}\right\rangle_{i}\right)$$
$$- \left(\frac{R}{L} + jkw_{o}\right)\left\langle i_{x}^{s}\right\rangle_{k} - \frac{1}{L}\left\langle V_{dc}\right\rangle_{k} \qquad (4.23)$$

$$\left\langle v_{x}\right\rangle_{k} = -\frac{1}{4}\left(\sum_{i=-\infty}^{+\infty}\left\langle S_{x}^{s}\right\rangle_{k-i}\left\langle V_{Cx}^{d}\right\rangle_{i} + \sum_{i=-\infty}^{+\infty}\left\langle S_{x}^{d}\right\rangle_{k-i}\left\langle V_{Cx}^{s}\right\rangle_{i}\right)$$
$$- \left(\frac{R+jkw_{o}}{2}\right)\left\langle i_{x}^{d}\right\rangle_{k} - \frac{L}{2}\frac{d}{dt}\left\langle i_{x}^{d}\right\rangle_{k} \qquad (4.24)$$

where $\omega_{o} = \frac{2\pi}{T}$ is the fundamental angular frequency of the system.

Note that i_{x}^{s} and V_{Cx}^{s} contain dc and even harmonics, and V_{Cx}^{d} and v_{x} comprise odd harmonics. According to (4.19), i_{x}^{s} is made of dc current and circulating current. Therefore, predominant harmonic components of i_{x}^{s} are dc and second harmonics (k = 0 and 2). Similarly for the other two state variables V_{Cx}^{s} and V_{Cx}^{d}, consideration of the first two harmonics components, i.e. k = 0 and 2 for V_{Cx}^{s} and k = 1 and 3 for V_{Cx}^{d} is adequate since capacitor ripples depend on the current flowing through the

submodules and higher order harmonics of these variables are almost non-existing. As shown in Chapter 6, this choice provides accurate results compared to an EMT simulator.

A state equation can be written for individual harmonic component of each state variable substituting corresponding k values. The resulting system takes the form of a first-order linear system as given below.

$$\frac{d}{dt}X(t) = A(t)X(t) + B(t)U(t) \tag{4.25}$$

where

$$X(t) = \left[\left\langle i_x^s \right\rangle_0 \quad \left\langle V_{Cx}^s \right\rangle_0 \quad \mathrm{Re}\left\langle V_{Cx}^d \right\rangle_1 \quad \mathrm{Im}\left\langle V_{Cx}^d \right\rangle_1 \quad \mathrm{Re}\left\langle i_x^s \right\rangle_2 \quad \mathrm{Im}\left\langle i_x^s \right\rangle_2 \quad \mathrm{Re}\left\langle V_{Cx}^s \right\rangle_2 \quad \mathrm{Im}\left\langle V_{Cx}^s \right\rangle_2 \quad \mathrm{Re}\left\langle V_{Cx}^d \right\rangle_3 \quad \mathrm{Im}\left\langle V_{Cx}^d \right\rangle_3 \right]^T$$

$$\tag{4.26}$$

$$U(t) = \left[\left\langle V_{dc} \right\rangle_0 \quad \mathrm{Re}\left\langle i_x^d \right\rangle_1 \quad \mathrm{Im}\left\langle i_x^d \right\rangle_1 \quad \mathrm{Re}\left\langle i_x^d \right\rangle_3 \quad \mathrm{Im}\left\langle i_x^d \right\rangle_3 \right]^T \tag{4.27}$$

$$A(t) =$$

$$
\begin{bmatrix}
\dfrac{-R}{L} & \dfrac{-\langle S_x^s\rangle_0}{2L} & \dfrac{-\mathrm{Re}\langle S_x^d\rangle_1}{L} & \dfrac{-\mathrm{Im}\langle S_x^d\rangle_1}{L} & 0 & 0 & 0 & 0 & \dfrac{-\mathrm{Re}\langle S_x^d\rangle_3}{L} & \dfrac{-\mathrm{Im}\langle S_x^d\rangle_3}{L} \\[2ex]
\dfrac{\langle n_x^s\rangle_0}{\gamma} & 0 & 0 & 0 & 0 & 0 & 0 & 0 & 0 & 0 \\[2ex]
\dfrac{\mathrm{Re}\langle S_x^d\rangle_1}{\gamma} & 0 & 0 & w & \dfrac{\mathrm{Re}\!\left(\langle S_x^d\rangle_1+\langle S_x^d\rangle_3\right)}{\gamma} & \dfrac{\mathrm{Im}\!\left(\langle S_x^d\rangle_1+\langle S_x^d\rangle_3\right)}{\gamma} & 0 & 0 & 0 & 0 \\[2ex]
\dfrac{\mathrm{Im}\langle S_x^d\rangle_1}{\gamma} & 0 & -w & 0 & \dfrac{-\mathrm{Im}\!\left(\langle S_x^d\rangle_1-\langle S_x^d\rangle_3\right)}{\gamma} & \dfrac{\mathrm{Re}\!\left(\langle S_x^d\rangle_1-\langle S_x^d\rangle_3\right)}{\gamma} & 0 & 0 & 0 & 0 \\[2ex]
0 & 0 & \dfrac{-\mathrm{Re}\!\left(\langle S_x^d\rangle_1+\langle S_x^d\rangle_3\right)}{2L} & \dfrac{\mathrm{Im}\!\left(\langle S_x^d\rangle_1-\langle S_x^d\rangle_3\right)}{2L} & \dfrac{-R}{L} & 2w_o & \dfrac{-\langle S_x^s\rangle_0}{2L} & 0 & \dfrac{-\mathrm{Re}\langle S_x^d\rangle_1}{2L} & \dfrac{-\mathrm{Im}\langle S_x^d\rangle_1}{2L} \\[2ex]
0 & 0 & \dfrac{-\mathrm{Im}\!\left(\langle S_x^d\rangle_1+\langle S_x^d\rangle_3\right)}{2L} & \dfrac{-\mathrm{Re}\!\left(\langle S_x^d\rangle_1-\langle S_x^d\rangle_3\right)}{2L} & -2w_o & \dfrac{-R}{L} & 0 & \dfrac{-\langle S_x^s\rangle_0}{2L} & \dfrac{\mathrm{Im}\langle S_x^d\rangle_1}{2L} & \dfrac{\mathrm{Re}\langle S_x^d\rangle_1}{2L} \\[2ex]
0 & 0 & 0 & 0 & \dfrac{\langle S_x^s\rangle_0}{\gamma} & 0 & 0 & 2w & 0 & 0 \\[2ex]
0 & 0 & 0 & 0 & 0 & \dfrac{\langle S_x^s\rangle_0}{\gamma} & -2w & 0 & 0 & 0 \\[2ex]
\dfrac{\mathrm{Re}\langle S_x^d\rangle_3}{\gamma} & 0 & 0 & 0 & \dfrac{\mathrm{Re}\langle S_x^d\rangle_1}{\gamma} & \dfrac{-\mathrm{Im}\langle S_x^d\rangle_1}{\gamma} & 0 & 0 & 0 & 3w \\[2ex]
\dfrac{\mathrm{Im}\langle S_x^d\rangle_3}{\gamma} & 0 & 0 & 0 & \dfrac{\mathrm{Im}\langle S_x^d\rangle_1}{\gamma} & \dfrac{\mathrm{Re}\langle S_x^d\rangle_1}{\gamma} & 0 & 0 & -3w & 0
\end{bmatrix}
$$

(4.28)

$$
B(t) =
\begin{bmatrix}
\dfrac{1}{L} & 0 & 0 & 0 & 0 \\[2ex]
0 & \dfrac{2\,\mathrm{Re}\langle S_x^d\rangle_1}{\gamma} & \dfrac{2\,\mathrm{Im}\langle S_x^d\rangle_1}{\gamma} & \dfrac{2\,\mathrm{Re}\langle S_x^d\rangle_3}{\gamma} & \dfrac{2\,\mathrm{Im}\langle S_x^d\rangle_3}{\gamma} \\[2ex]
0 & \dfrac{\langle S_x^s\rangle_0}{\gamma} & 0 & 0 & 0 \\[2ex]
0 & 0 & \dfrac{\langle S_x^s\rangle_0}{\gamma} & 0 & 0 \\[2ex]
0 & 0 & 0 & 0 & 0 \\[2ex]
0 & 0 & 0 & 0 & 0 \\[2ex]
0 & \dfrac{\mathrm{Re}\!\left(\langle S_x^d\rangle_1+\langle S_x^d\rangle_3\right)}{\gamma} & \dfrac{-\mathrm{Im}\!\left(\langle S_x^d\rangle_1-\langle S_x^d\rangle_3\right)}{\gamma} & 0 & 0 \\[2ex]
0 & \dfrac{\mathrm{Im}\!\left(\langle S_x^d\rangle_1+\langle S_x^d\rangle_3\right)}{\gamma} & \dfrac{\mathrm{Re}\!\left(\langle S_x^d\rangle_1-\langle S_x^d\rangle_3\right)}{\gamma} & 0 & 0 \\[2ex]
0 & 0 & 0 & 0 & 0 \\[2ex]
0 & 0 & 0 & 0 & 0
\end{bmatrix}
$$

(4.29)

and $\gamma = 2NC_{SM}$.

Input matrix U can be constructed using the instantaneous values measured at both DC side and AC side dynamic phasor-EMT interfaces. According to definition, one can readily calculate $\langle V_{dc} \rangle_0$ by taking the average of the instantaneous values of V_{dc} during the previous cycle. Dynamic phasors $\langle i_x^d \rangle_1$ and $\langle i_x^d \rangle_3$ can be found using the measured line current with the help of (3.2) with $k = 1$ and 3.

Dynamic phasors of all individual harmonic components, except the DC component, are made up of complex values. Therefore, they must be separated to real and imaginary parts before taking the solution of the above first-order differential equation system using a suitable integration method. More details about the solution of this system are discussed in subsection 4.1.4.

A definitive task of modeling is to generate the output AC voltage waveform. Producing the phase voltage using the conventional dynamic phasor method is straightforward since one can readily compute dynamic phasor components of phase voltage using (4.24) and the state variables defined in (4.26) with the help of a switching function. Generally, an MMC arm consists of a large number of submodules. As a result, the output voltage waveform takes the shape of a sinusoidal waveform at the fundamental frequency. Therefore, producing base-frequency components is often adequate to generate an accurate steady state output voltage waveform. However, in various network transients such as faults, it is possible to find dc and high frequency contents in the waveform. On the other hand, there are some simulation scenarios that use a small number of arm submodules. In such situations, a significant amount of higher order harmonics exists and use of extended-frequency dynamic phasors is required in order to accurately model steady state and transient responses. This is, however, challenging with CDP since it requires repetitive computation of a large

number of frequency components separately. As a way out, a flexible method to determine the AC voltage employing BFDP is presented below.

The nature of the output voltage waveform is mainly determined by the switching of submodule capacitors and the current passing through the arm inductor and resistor. Therefore, the entire harmonic spectrum of the output voltage can be compressed to one equation using BFDP if one can compute dynamic phasors of the switching functions corresponding to each harmonic and map the instantaneous values of AC current to BFDP efficiently.

$$\langle v_x \rangle_B = -\frac{1}{4}\left(\langle S_x^s . V_{Cx}^d \rangle_B + \langle S_x^d . V_{Cx}^s \rangle_B\right) - \left(\frac{R + jw_oL}{2}\right)\langle i_x^d \rangle_B - \frac{L}{2}\frac{d}{dt}\langle i_x^d \rangle_B \qquad (4.30)$$

The BFDP voltage equation (4.30) consists of two product terms. None of the variables in each product is sinusoidal. Therefore, BFDP of both product terms have to be found as in (3.11). However, S_x^s is purely a DC component and the higher order harmonics of V_{Cx}^d and V_{Cx}^s are not significant. Therefore, reasonably accurate results can be obtained considering only two harmonic components, i.e., $k = 1$ and 3 for $\langle V_{Cx}^d \rangle_k$ and $k = 0$ and 2 for $\langle V_{Cx}^s \rangle_k$. Note that those dynamic phasor values are already available from the state equation solution given by (4.25).

The challenging part of (4.30) is formulation of $\langle i_x^d \rangle_B$ because it requires a number of integrations if constructed using (3.2) and (3.9). However, instantaneous values of i_x^d are available from the EMT solver. Therefore, $\langle i_x^d \rangle_B$ can be constructed efficiently using the algorithm discussed in subsection 3.2.2. The derivative part of the right-hand side can be ignored if the user is prepared to give up a negligible

amount of accuracy since the arm inductance is typically small (in the range of several milli-henries (mH)). If not ignored, it can be readily calculated by taking the difference of $\langle i_x^d \rangle_B$ present value and past value then dividing by the time-step.

The algorithm given in subsection 3.2.2 maps the entire harmonic spectrum of the AC current i_x^d into $\langle i_x^d \rangle_B$. Therefore, the accuracy of the constructed voltage waveform mainly depends on how many harmonics are chosen to construct the switching function, when the voltage waveform is expected to have many harmonics.

4.1.3   Switching Function

The role of the switching function is to illustrate the number of inserted submodules in an arm during each switching state. The discrete function takes place due to NLC modulation can be written as a series of harmonic components as below. It is important to note that these two switching functions are produced based on the assumption that all submodule capacitor voltages in an arm are balanced and are equal to the nominal value of the capacitor.

$$S_x^u = \frac{N}{2} - m\frac{N}{2}\sum_{k=1}^{\infty} C_k \sin(k\theta + k\delta + k\phi_x) \tag{4.31}$$

$$S_x^l = \frac{N}{2} + m\frac{N}{2}\sum_{k=1}^{\infty} C_k \sin(k\theta + k\delta + k\phi_x) \tag{4.32}$$

The phase angle θ comes from a PLL locked onto the PCC of AC network. The angle difference between the PCC and the converter output, δ, and the modulation index, m, are generated by the controller and obtained as inputs. The constant angle ϕ_x is a representation of the phase thus ϕ_x = 0, -2π/3, and +2π/3 for phase *a, b,* and *c,*

respectively. Coefficient C_k is calculated based on the NLC technique used for submodule switching discussed in Section 2.2.1. For odd and even values of N, the C_k can be calculated separately as below.

$$C_k = \begin{cases} \left(\dfrac{8}{k\pi N} \displaystyle\sum_{i=1}^{\frac{N+1}{2}} \cos(k\alpha_i) \right) - \cos(k\alpha_1) & \text{if } N \text{ odd} \\[6mm] \left(\dfrac{8}{k\pi N} \displaystyle\sum_{i=1}^{\frac{N}{2}} \cos(k\alpha_i) \right) & \text{if } N \text{ even} \end{cases} \tag{4.33}$$

where switching instant α_i is given by,

$$\alpha_i = \begin{cases} \sin^{-1}\left(\dfrac{2}{mN}(i-1) \right) & \text{if } N \text{ odd} \\[6mm] \sin^{-1}\left(\dfrac{2}{mN}\left(i-\dfrac{1}{2}\right) \right) & \text{if } N \text{ even} \end{cases} \tag{4.34}$$

In order to use these in MMC equations, addition and difference of the upper and lower arm's switching functions have to be taken.

$$S_x^s = N \tag{4.35}$$

$$S_x^d = -mN \sum_{k=1}^{\infty} C_k \sin(kw_o t + k\delta + k\phi_x) \tag{4.36}$$

The summation S_x^S is a dc quantity; hence, higher order harmonics do not exist. The difference of the switching functions, S_x^d, has only odd harmonics; therefore, k is an odd number. Dynamic phasor representation of kth harmonic of (4.35) and (4.36) is given by

56

$$\left\langle S_x^S \right\rangle_k = \begin{cases} N & \text{if } k = 0 \\ 0 & \text{Otherwise} \end{cases} \tag{4.37}$$

$$\left\langle S_x^d \right\rangle_k = \begin{cases} j\dfrac{mNC_k}{2}e^{jk(\delta+\phi_x)} & \text{if } k \text{ odd} \\ 0 & \text{Otherwise} \end{cases} \tag{4.38}$$

Note that the multiplication $m \times C_k$ provides the Fourier coefficient corresponding to the kth harmonic of the discrete function take place due to NLC. Once C_k is calculated, the dynamic phasor of the switching function for any harmonic can be easily found by means of (4.38).

4.1.4   Solving Equations Numerically

There are many well-established solution techniques to obtain a solution of a first order differential equation system. However, real world systems described by differential equations are often complex and large, thus analytical solutions are impractical. Apart from that, digital computer simulations are unable to produce continuous information of the dynamics of a given problem; instead, dynamic data are produced in discrete intervals. On the other hand, in power system dynamics problems, it is sufficient to obtain a numerical approximation; hence, numerical integration techniques are widely used.

Selection of a proper numerical method is vital since many properties of the solution such as accuracy, stability, and time requirement rest on the technique used to acquire the solution [48]. There are a number of numerical techniques that provide diverse benefits and drawbacks. One of simplest methods used in some applications is Euler's method. Weaknesses of this method are low level of accuracy and inability

to guarantee a stable solution [49]. Another well-known and extensively used numerical method is the trapezoidal integration method. It provides reliable and accurate results and, most importantly it preserve the stability of the solution for a linear real system [48], [50]. Therefore, the trapezoidal method has become a method of choice in most dynamic simulation applications. There are other methods such as Runge-Kutta second order and fourth order methods, but they lack simplicity and general applicability, which the trapezoidal method possesses [48], [49]. Considering the application and its stability requirement, the trapezoidal numerical integration technique is used to solve the linear system described in (4.25). Basic concepts of this method are discussed below.

Consider the following general form of a first order system:

$$\dot{x}(t) = f\big(x(t), u(t), t\big) \tag{4.39}$$

For a linear state equation system, (4.39) takes the following standard form:

$$\dot{x}(t) = Ax(t) + Bu(t) \tag{4.40}$$

The objective of the numerical integration method is to approximate the value of x at time $t = t + \Delta t$ assuming that the solution at time t is known. The trapezoidal solution can be derived as below.

$$x(t + \Delta t) \approx x(t) + \left(\frac{\dot{x}(t) + \dot{x}(t + \Delta t)}{2} \right) \Delta t \tag{4.41}$$

Standard form of the solution is given by (4.42) and (4.43).

$$x(t + \Delta t) \approx x(t) + \left(\frac{f\left(x(t), u(t)\right) + f\left(x(t + \Delta t), u(t + \Delta t)\right)}{2} \right) \Delta t \qquad (4.42)$$

$$x(t + \Delta t) \approx x(t) + \left(\frac{Ax(t) + Bu(t) + Ax(t + \Delta t) + Bu(t + \Delta t)}{2} \right) \Delta t \qquad (4.43)$$

Then the linear formula can be further simplified as

$$x(t + \Delta t) \approx \left(I - \frac{\Delta t}{2} A \right)^{-1} \left(\left(I + \frac{\Delta t}{2} A \right) x(t) + B \left(\frac{u(t) + u(t + \Delta t)}{2} \right) \Delta t \right) \qquad (4.44)$$

Solution of MMC dynamic phasor system of equation is obtained using (4.44). Starting from the initial conditions at $t = 0$, solution for state variables is found at each time-step until the end of the simulation is reached. Since the matrix A is time-variant, the inverse of $\left(I - \frac{\Delta t}{2} A \right)$ has to be taken at each time-step. Given the matrix A is 10x10 (for one phase), and considering its sparsity, a technique such as LU decomposition can be employed to compute the inversion.

In the meantime, selection of an appropriate simulation time-step Δt is essential since a large time-step results in a large deviation of the solution from the actual solution and a smaller time-step size leads to less computational efficiency. Therefore, a trade-off between accuracy and speed has to be made when selecting the right simulation time-step and it is often found by trial and error.

4.2   DP-EMT Interface

The MMC model has to interface with EMT simulator on both DC and AC sides. A general block diagram of the proposed interface including PLL and controller is illustrated in Figure 4.2.
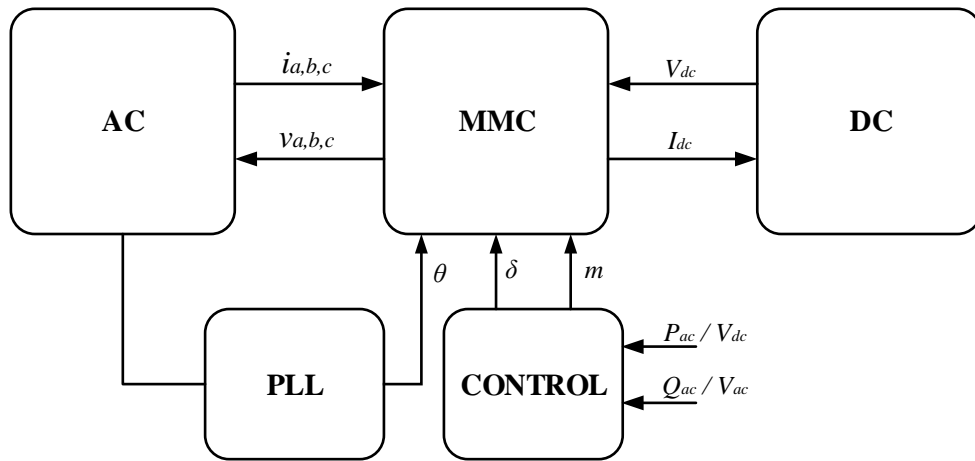
Figure 4.2 : Proposed MMC-EMT interface

The instantaneous values of line currents corresponding to all three phases from the AC network and DC voltage from the DC bus are taken at the interfaces. Phase voltages and DC current are calculated and fed to the corresponding systems. Based on this approach, the MMC behaviour is represented using a dependent current source and three voltage sources as depicted in Figure 4.3. The internal variables of the MMC are modeled and available for observation.
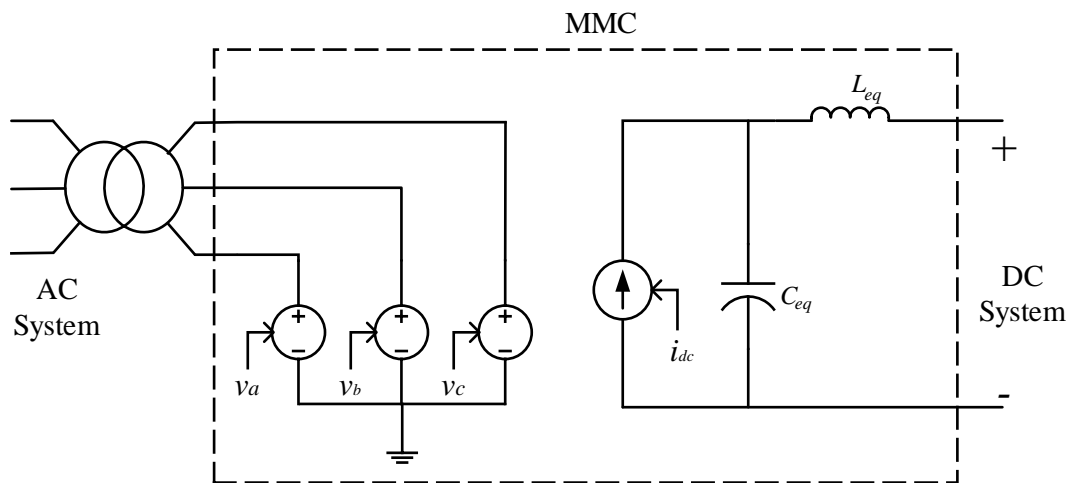
Figure 4.3 : MMC model representation

4.2.1   AC-side Interface

The AC side is provided with three controlled voltage sources and the command for each source is given through the dynamic phasor solver. The complete mathematical procedure of voltage waveforms modeling is discussed in Section 4.1. A summary of this procedure can be compressed into a schematic diagram as shown in Figure 4.4.
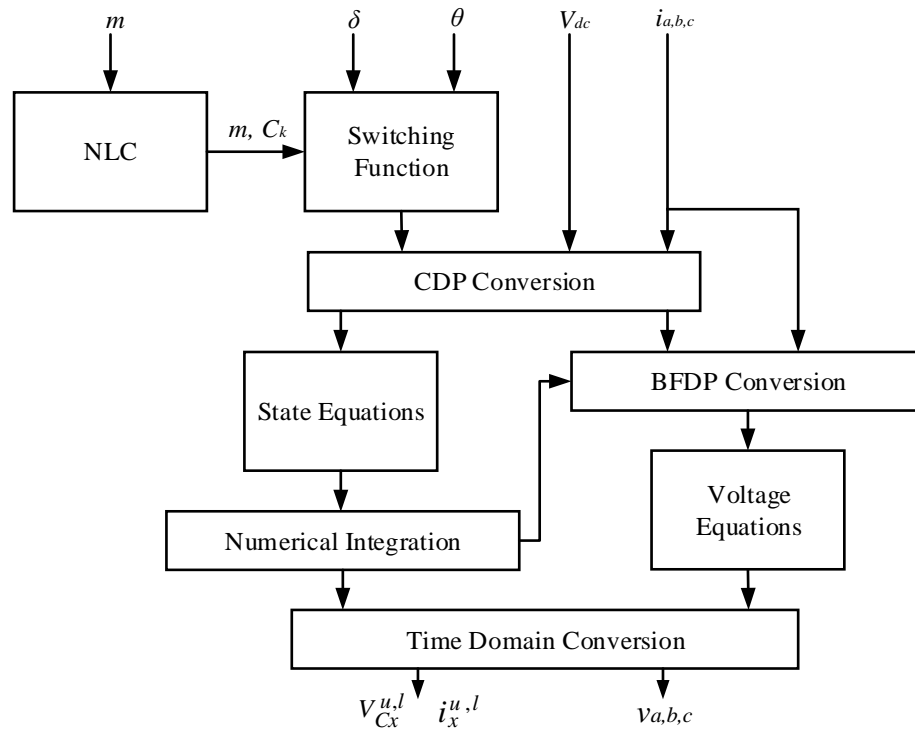
Figure 4.4 : Schematic diagram of AC voltage modeling procedure

To begin, the nearest level control scheme determines the number of conducting submodules based on the modulation index m, and subsequently the Fourier coefficients C_k of resulting discrete waveform. They are then used to produce the switching function, which is synchronized with the AC network by means of PLL measurement and power angle δ. In the subsequent stage, the switching function

along with DC voltage and line currents, which are available from the interfaces, are converted to CDP and state equations given by (4.21)-(4.23) are derived. Solution of this system, which is obtained through trapezoidal integration, delivers the behaviour of internal parameters of the MMC. Switching function, line currents, and internal variables obtained by numerical integration are used to produce voltage waveforms as in (4.30) in BFDP domain. Finally, all parameters are converted to time-domain before being sent as commands to controlled voltage sources at AC interface. MMC arm currents and submodule voltages are available as outputs for observation.

4.2.2   DC-Side Interface

The proposed representation of DC system interface with MMC can be seen from Figure 4.3. DC current is modelled and fed to the controlled current source. There are two methods to derive the DC current.

➢ **Power balance approach**

In this method of modeling, the principle of power balance is employed; internal MMC losses are assumed to be zero. Therefore, the DC current can be readily calculated by equating the instantaneous power on the AC side to instantaneous power on the DC side.

$$I_{dc}(t) = \frac{\sum_{x=a,b,c} v_x\, i_x}{V_{dc}(t)} \tag{4.45}$$

Line currents for each phase and DC voltage are available from the interface while phase voltages are available from the dynamic phasor solution. Since fast transients are of no interest in an average model, the calculated instantaneous DC

current can be sent through a low-pass filter with appropriate cut-off frequency before it is given to the current source.

➢ **State variable approach**

From (4.19), it is observed that the state variable i_x^S is made of DC current and arm circulating current. Under the assumption that all three phases are well balanced, summation of second order circulating currents of three phases turns out to be zero. In fact, the DC term of i_x^S is directly available from dynamic phasor solution. Therefore, a relationship to determine DC current can be written incorporating i_x^S as given in (4.46).

$$I_{dc}(t) = \frac{\sum_{x=a,b,c} \left\langle i_x^s \right\rangle_0}{2} \tag{4.46}$$

Dynamic phasor of a DC term ($k = 0$) is the same as the time-domain value, hence, separate conversion is not required.

Whichever method is used to determine the DC current, the effect of energy stored inside the MMC on the DC side is not represented through the current source. Therefore, an equivalent capacitor C_{eq} is added externally in parallel with the current source to characterise the total energy stored inside submodule capacitors. The value of C_{eq} can be derived using energy conservation principle. Assume E_{MMC} as the total energy stored inside the MMC submodules; the value of E_{MMC} is given by the summation of energy stored in the upper and lower arms in each phase. Equivalent capacitor must be able to bear the same amount of energy.

$$E_{MMC} = \frac{1}{2} C_{SM} N \sum_{x=a,b,c} \left(V_{Cx}^u\right)^2 + \left(V_{Cx}^u\right)^2 \qquad (4.47)$$

$$E_{MMC} = \frac{1}{2} C_{eq} V_{dc}^2 \qquad (4.48)$$

If one assumes that all capacitors are well balanced, both the upper and lower submodule voltages are approximately equal to V_{dc}/N. Then, (4.47) can be further simplified to,

$$E_{MMC} = 6 \times \frac{1}{2} C_{SM} N \left(\frac{V_{dc}}{N}\right)^2 \qquad (4.49)$$

Finally, a formula for DC side equivalent capacitance can be derived in terms of submodule capacitance including (4.48) in (4.49).

$$C_{eq} = \frac{6 C_{SM}}{N} \qquad (4.50)$$

According to (4.9) and (4.10), one third of the DC current flows in each arm, and consequently, through each arm inductance. The DC side equivalent inductor L_{eq} is included to mimic the effect of arm inductance on DC current (especially rate of change of DC current). Since the same current flow through the upper and lower arms, inductors in both arms are connected in series while inductors in each phase are connected in parallel to each other.
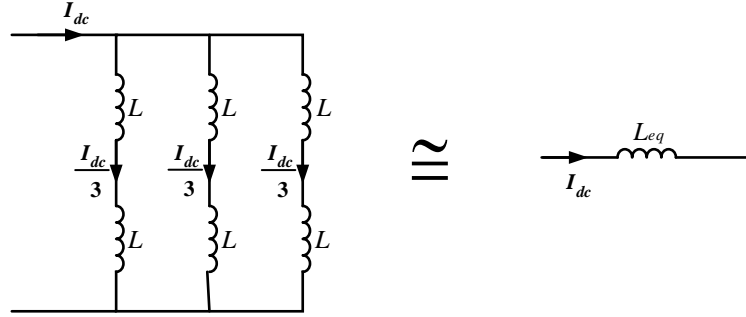
Figure 4.5 : MMC equivalent DC-side inductor representation

Figure 4.5 shows the formation of equivalent inductor using arm inductors. A simple formula to find L_{eq} can be given as in (4.51).

$$L_{eq} = \frac{2}{3}L \qquad (4.51)$$

4.3 Summary and Major Conclusions

This chapter presented a novel and flexible average model of an MMC, which is capable of interfacing with an EMT solver. The model uses a hybrid method that involve both CDP and BFDP techniques. The governing equations of the MMC dynamics were derived and then converted to phasor domain by applying dynamic phasor operators. Internal dynamics were modeled in CDP domain, in the form of a state equation system by selecting only important harmonics. Solution of this system, which was obtained via numerical integration, was then used to model external AC voltages in BFDP domain. A switching function was employed to give the relationship between AC side and DC side. The interface of the MMC was made of controlled current source and voltage sources. Derivation of DC current and equivalent parameter values were discussed. The main unique feature of this model is that it has

the capability to include any number of output harmonics without adversely affecting the simulation speed (as shown in Chapter 5), while modeling internal dynamics accurately.

Chapter 5

Model Validation

The developed MMC model is validated by comparing its results with a detailed IGBT-based MMC model (henceforward referred to as detailed switching model) and another validated MMC model (henceforward referred to as detailed average model) with lower computational load, both developed in PSCAD/EMTDC simulator. Specifics about the detailed average model can be found in [8]. In order to obtain accurate transient results, the time-step used to simulate detailed switching model has to be very small compared to averaged models. Therefore, transient results of small systems are compared with the detailed switching model while transient results of larger systems of the developed model are compared with the detailed averaged model.

PSCAD/EMTDC is a widely accepted EMT-type simulation tool developed for analysis of powers system dynamic performances. It allows the user to construct electrical networks schematically and perform simulations in order to analyse the constructed system. Solutions are obtained based on a user-defined fixed time-step. It has a master library that consists of a large number of electrical components, and provides flexibility to model user-defined components using FORTRAN programing language.

The MMC model proposed in Chapter 4 is programmed as a user-defined component and then integrated to the EMT simulator. The detailed switching model is built using components available in the master library. Control systems and the rest of the electrical network to which the MMC is interfaced are similar for all three models. Four types of HVDC test systems are considered for model validations. These include, (i) inverter operation of MMC, (ii) rectifier operation of MMC, (iii) a back-to-back system, and (iv) a twelve-bus system with an MMC-HVDC link placed between two distance busses.

5.1   MMC Operation as an Inverter

5.1.1   Test System Specifications

Figure 5.1 illustrates the configuration of the first test system considering operation of MMC as an inverter. Behaviour of the AC system is represented using a Thévenin impedance and a voltage source, and the DC side is provided with two constant voltage sources with a grounded middle point. The MMC is connected to the AC system through a transformer at the PCC.
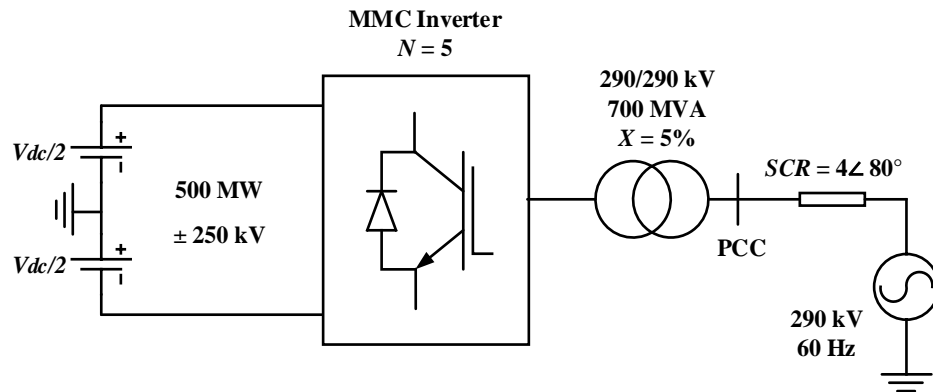

Figure 5.1 : MMC inverter test system configuration

The number of submodules per arm is selected as five for clarity of identifying voltage levels of waveforms and for the purpose of reducing the computational burden of the detailed switching MMC model. Test system specifications are tabulated in Table 5-1.

Table 5-1 : MMC inverter test system specifications

Parameter	Value
AC system voltage	290 kV
AC system frequency	60 Hz
Short circuit ratio (SCR)	4.0 ∠ 80°
Transformer voltage ratio	290 kV : 290 kV
Transformer power rating	700 MVA
Transformer leakage reactance	0.05 pu
MMC submodule capacitance	1500 μF
Number of submodules per arm	5
MMC arm inductance	0.001 H
MMC arm resistance	0.05 Ω
Nominal DC voltage	±250 kV
Nominal DC power	500 MW

This test system is selected similar to the test system given in [18] for comparative purposes, thus transformer reactance and MMC arm reactance are not properly sized. However, it does not affect the functionality or the purpose of the simulation.

Real power flow of the inverter and the rms terminal voltage at the PCC are controlled by means of direct controllers for simplicity as shown in Figure 5.2. The operational and control performance can be improved significantly by employing decoupled controllers to control AC-side and circulating current.
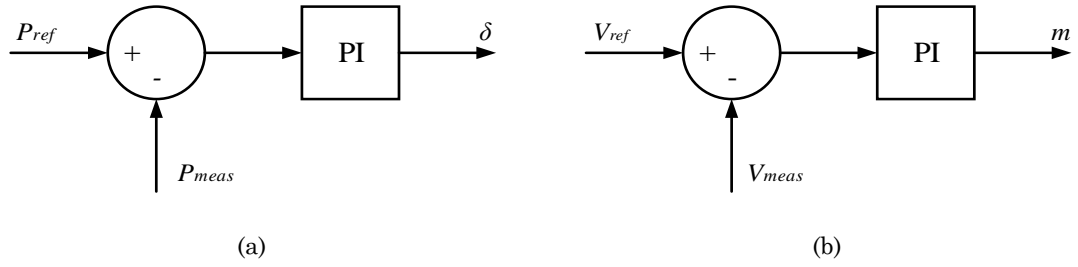
Figure 5.2 : MMC inverter (a) real power control (b) terminal voltage control

The error signals generated by comparing references and the measured values are given to the PI controllers to produce the modulation index and the converter power angle. The rest of the controls are modeled as discussed in Section 2.2.

5.1.2   Steady State Simulation

The time-step used for detailed switching model simulation is 5 µs for high accuracy. In order to compare the influence of the number of harmonics for dynamic phasor model waveforms, the same time-step is used for the first simulation of dynamic phasor model. Power and system voltage are controlled at 500 MW and 1 pu, respectively and phase voltages and currents are measured at the PCC. Figure 5.3 illustrates a comparison of accuracy of steady state output waveforms of MMC by gradually increasing the number of harmonics in the dynamic phasor model. It is clear that the number of voltage level of the voltage waveform is six (N+1) and therefore, a large number of harmonics exist. When a small number of harmonics are considered in the dynamic phasor model, the error of the current and voltage waveforms seems to be large but it tends to become small when the number of harmonic considered is large. However, an overly large number of harmonics is unnecessary to include since it increases the computations without giving significant improvement of accuracy.
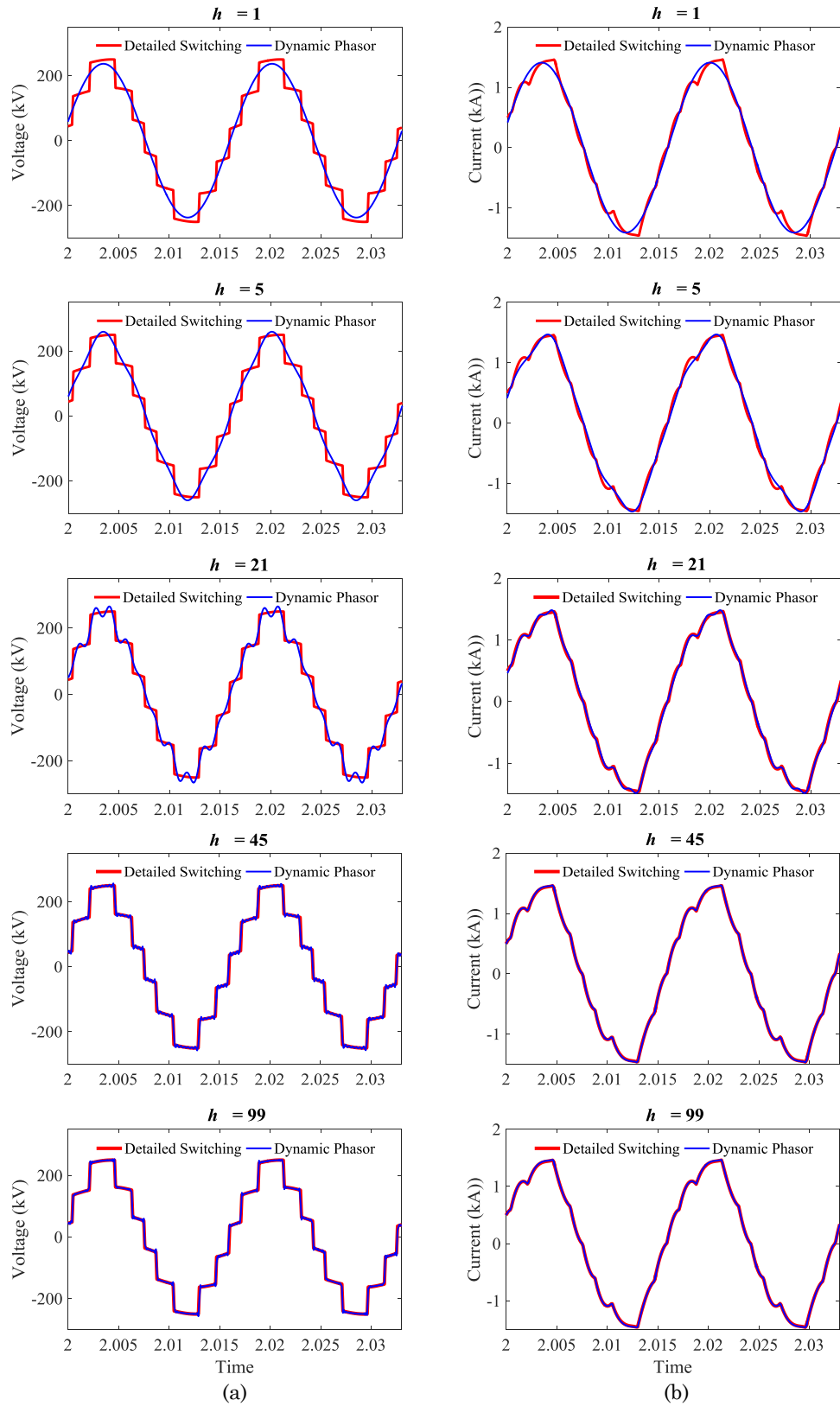
Figure 5.3 : Accuracy comparison of inverter waveforms by increasing the harmonic content, (a) output voltage waveform (b) output current waveform
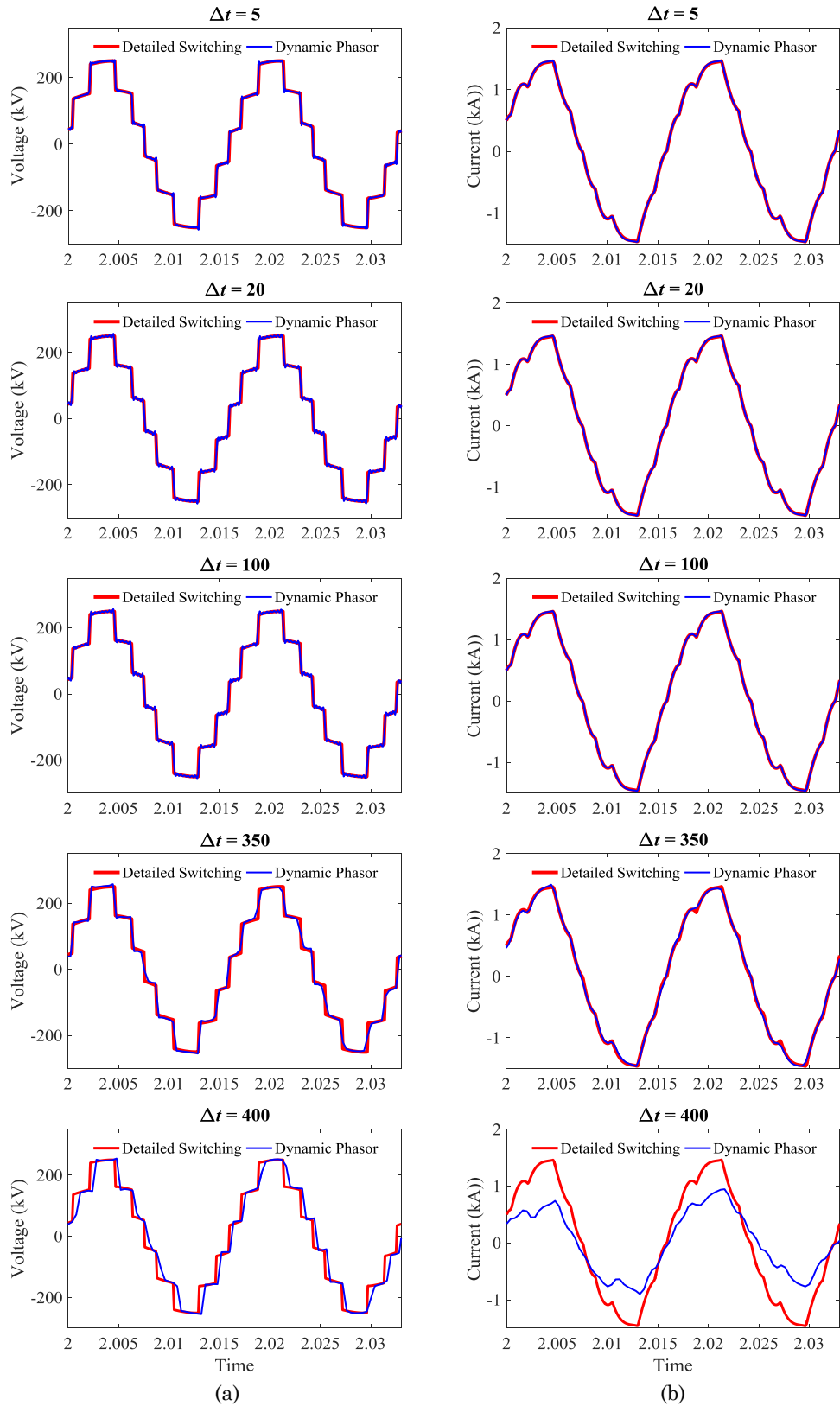
Figure 5.4 : Accuracy comparison of inverter waveforms for different time-steps, (a) output voltage waveforms (b) output current waveforms

In the second experiment, the influence of the simulation time-step for dynamic phasor model is compared. The detailed switching model is simulated using the 5 μs time-step and the accuracy of dynamic phasor model is compared by gradually increasing the simulation time-step. The number of harmonics included in the dynamic phasor model is kept constant at 45. Observations are shown in Figure 5.4. For smaller time-steps, results do not show any visual change in accuracy. However, the accuracy of the dynamic phasor waveforms is not significantly deteriorated as the time-step increases to larger values. As one can see from Figure 5.4, the dynamic phasor model provides reasonable results even up to a 350 μs time-step. Compared to the switching model, this is a marked improvement as the user can use a large time-step for EMT simulation and still obtain results with sufficient accuracy.

For clarification of advantage given by dynamic phasor model in terms of time-step size, the six-level switching model is also simulated with larger time-steps and compared with the simulation results obtained by simulating the same model with 5 μs time-step. Observations of the detailed switching model simulations are shown in the Figure 5.5. It can be seen that the switching model starts to produce visibly inaccurate results when the time-step reaches 100 μs. It is important to note that the switching model is constructed considering only five submodules per arm. In a real scenarios, however, the number of levels will be much larger; thus, the maximum time-step that can be used for the switching model simulation will be further reduced and even a very small time-step might not give correct information. Dynamic phasor model will not reduce the accuracy level for the same time-step as number of levels increases. This can be further observed from the back-to-back system simulation in Section 5.3.
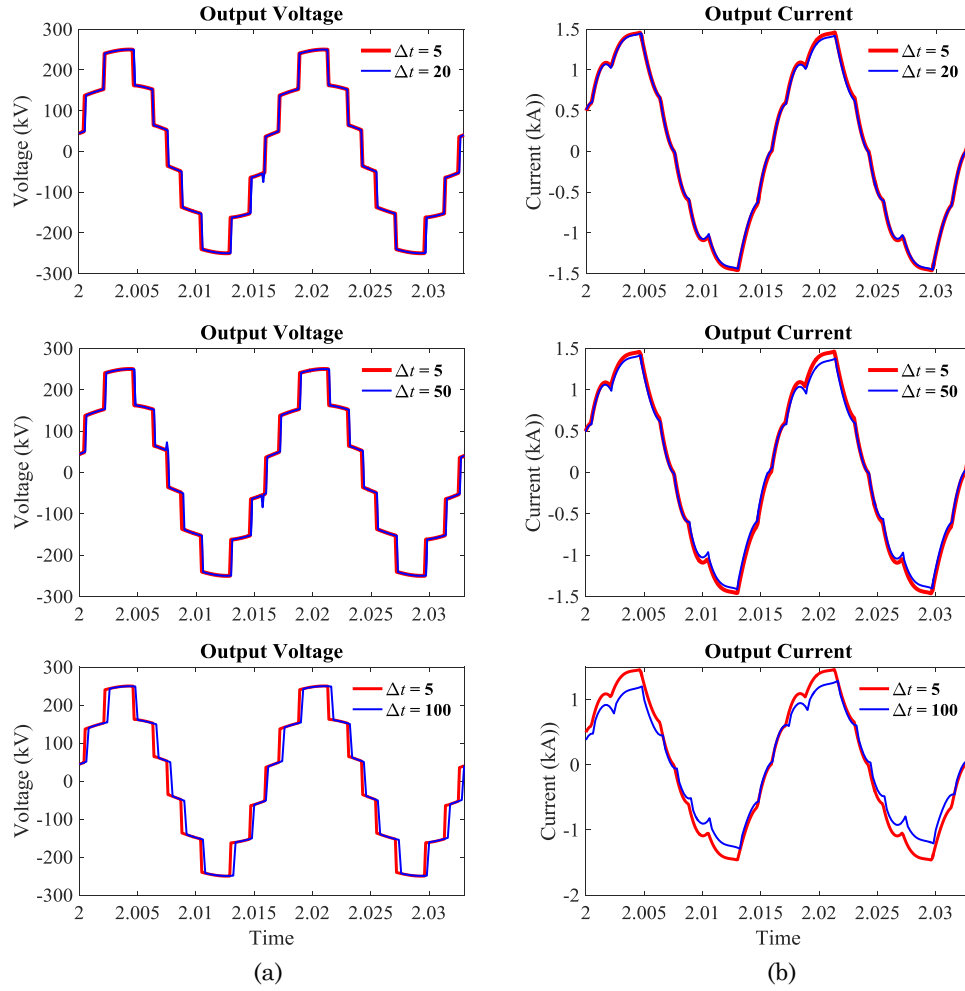
Figure 5.5 : Accuracy comparison of detailed MMC switching model for different time-steps, (a) voltage waveforms (b) current waveforms

One of the main features of the new dynamic phasor model is that it can give the internal steady state and dynamic waveforms of the MMC. Figure 5.6 illustrate the steady state performance of the MMC arm currents and submodule capacitor voltage ripples for a simulation time-step of 100 μs and with 45 harmonics at the output.
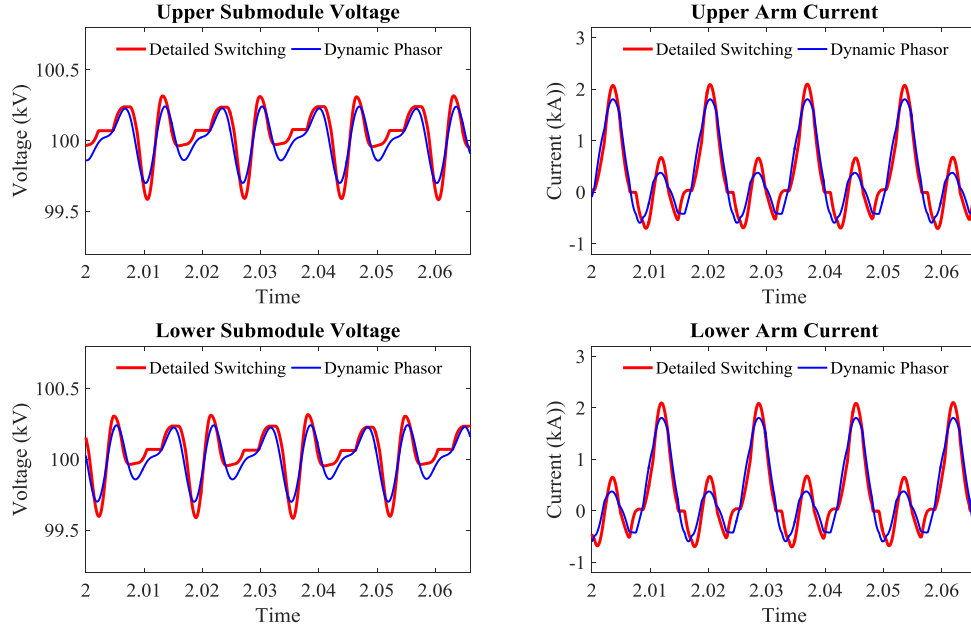
Figure 5.6 : MMC internal waveforms

It is observed that the new model is providing internal data with reasonable accuracy. Direct controls are used to control the MMC without a circulating current suppression method and also the number of voltage levels is very small; therefore, a significant amount of multiples of second order harmonic exists. However, as discussed in the previous chapter, only the first two harmonics of capacitor voltages and arm currents are modeled. Therefore, an error is generated in the dynamic phasor model compared to switching model. In case of need for improved accuracy, it is recommended to provide a circulating current controller.

5.1.3   Step Change of Real Power Reference

In order to compare the dynamic response of the MMC model, a step change of active power reference is given from 500 MW to 300 MW at 2.5 s for both models. Harmonic components up to 45th order are modeled and a time-step of 100 μs is used for dynamic phasor model simulation. Results are illustrates in Figure 5.7.
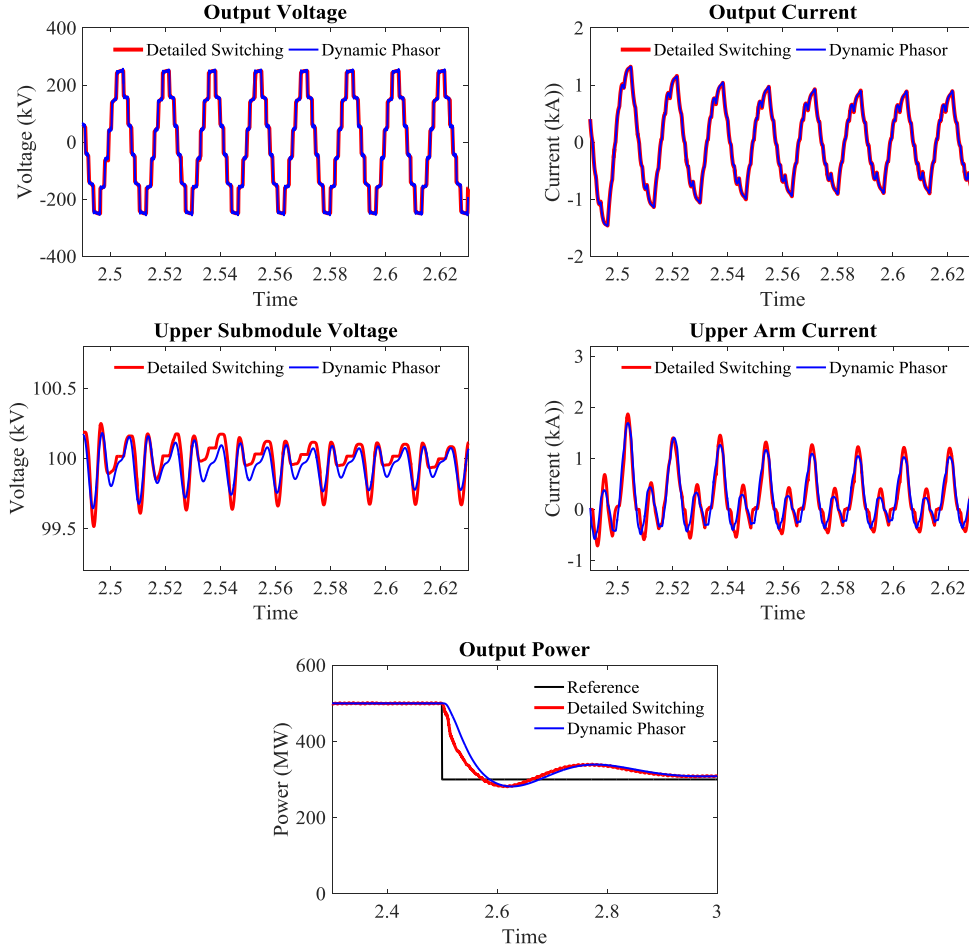
Figure 5.7 : Inverter response to a step change in active power reference

Since the voltage is controlled at 1 pu, there is no change of the output voltage waveform. However, the output current is reduced to respond to the power flow change. The output current is a part of the arm current. Therefore, arm currents and voltage ripples of the capacitors also respond to the active power change. As it can be seen from Figure 5.7, dynamic phasor model transients and switching model transients closely follow each other. The accuracy of the external waveforms of the dynamic phasor model is higher than that of the internal waveforms due to large number of harmonics considered.

5.1.4   Step Change of AC Voltage Magnitude Reference

A step change in the AC voltage magnitude from at PCC is applied at 2.5 s. The voltage

reference is reduced from 1 pu to 0.8 pu. Observations are shown in Figure 5.8.
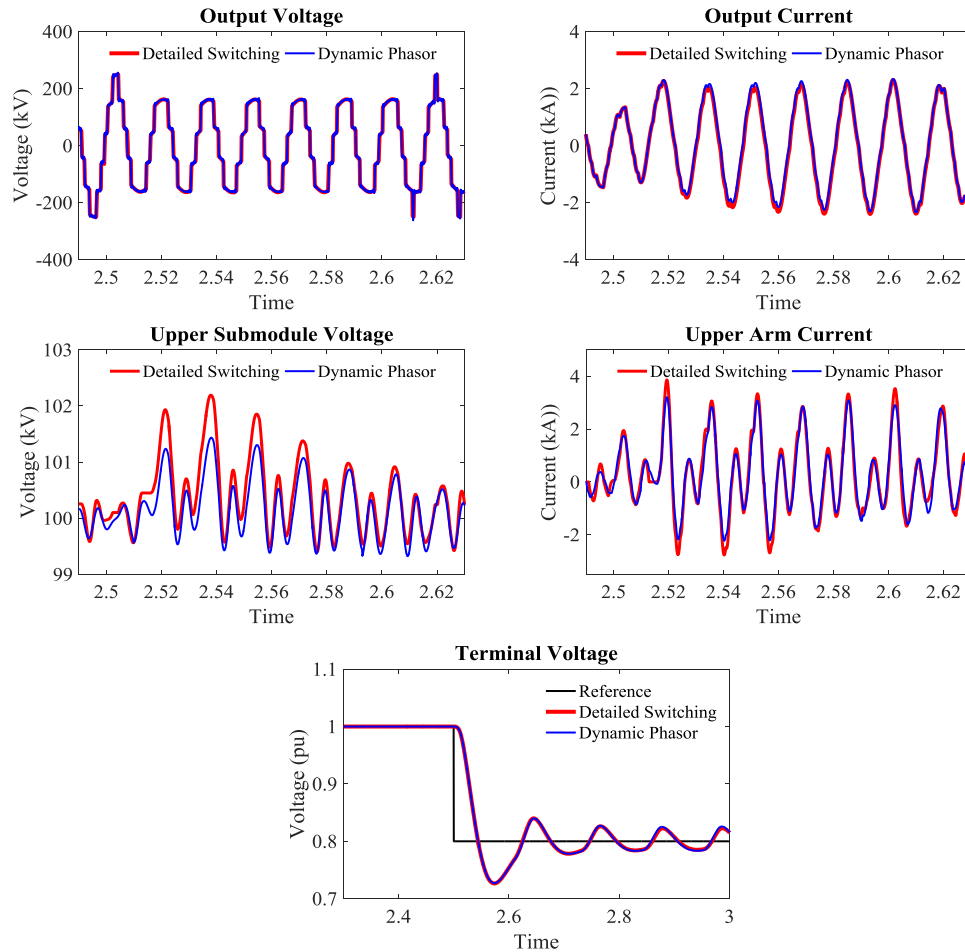
Figure 5.8 : Inverter response to a step change in voltage reference

It can be seen that when the voltage reference is lowered, the output voltage is

reduced and the current is increased to maintain the power flow at 500 MW. During

the initial transient, the number of levels of the MMC output voltage is reduced to

four then it increases back to six. External dynamics of the new model are nearly

identical to the PSCAD/EMTDC results and the internal dynamics are given with

reasonable accuracy.

5.2   MMC Operation as a Rectifier

5.2.1   Test System Specifications

The same system used in the Section 5.1 is used to study the operation of the MMC as a rectifier by changing the direction of the power flow. The DC side is replaced with a constant resistive load. The DC pole-to-pole voltage is controlled at 500 kV and AC voltage is controlled at 1 pu. Test system configuration and the control systems are shown in the Figure 5.9 and Figure 5.10, respectively.
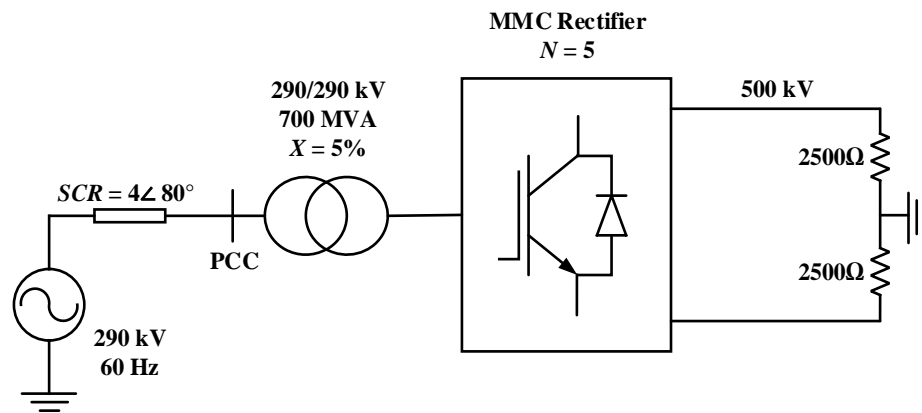
Figure 5.9 : MMC rectifier test system configuration
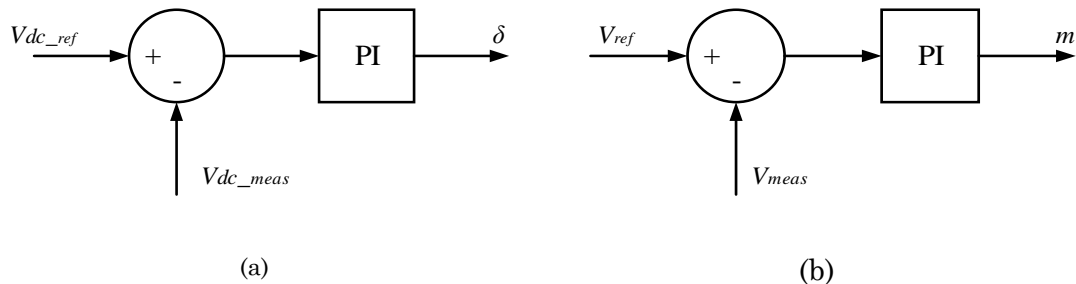
Figure 5.10 : MMC rectifier (a) DC voltage control (b) terminal voltage control

Both steady state and dynamic results of the dynamic phasor model are observed for simulations considering harmonics up to 45th order and using the time-step of 100 µs. Detailed switching model simulation is carried out using a 5-µs time-step.

5.2.2   Steady State Simulation

Figure 5.11 provides the results obtained from steady state simulations of both the switching and dynamic phasor models. As in the inverter case, the rectifier operation of the dynamic phasor model of MMC also provides accurate waveforms compared to PSCAD/EMTDC model. A small error can be observed from the output voltage and current waveforms of the dynamic phasor model compared to the switching model. The reason is that unlike the inverter operation, the rectifier is not supported with a constant dc voltage source. Therefore, the average capacitor voltage value of the switching model, and thus, the magnitude of voltage level of the rectifier fluctuates with the instantaneous DC link voltage. However, in the dynamic phasor model, the DC link voltage value is averaged over the previous cycle and the instantaneous waveform dynamics are ignored. The error can be minimized by increasing the number of submodules per arm.
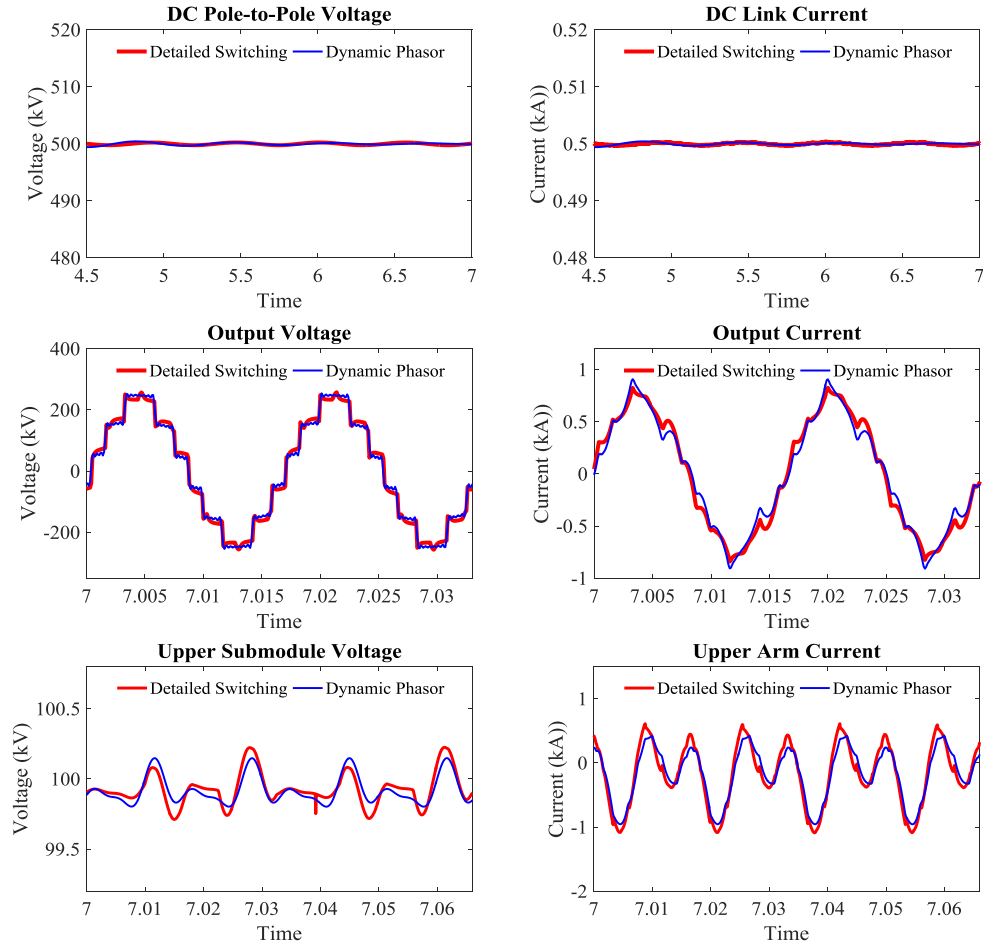
Figure 5.11 : MMC steady state operation as a rectifier

5.2.3 Step Change in DC Voltage Reference

A step change to DC voltage reference of the controller from 500 kV to 520 kV is applied at t = 7.5 s. Comparative results for internal and external dynamics are observed and depicted in Figure 5.12.
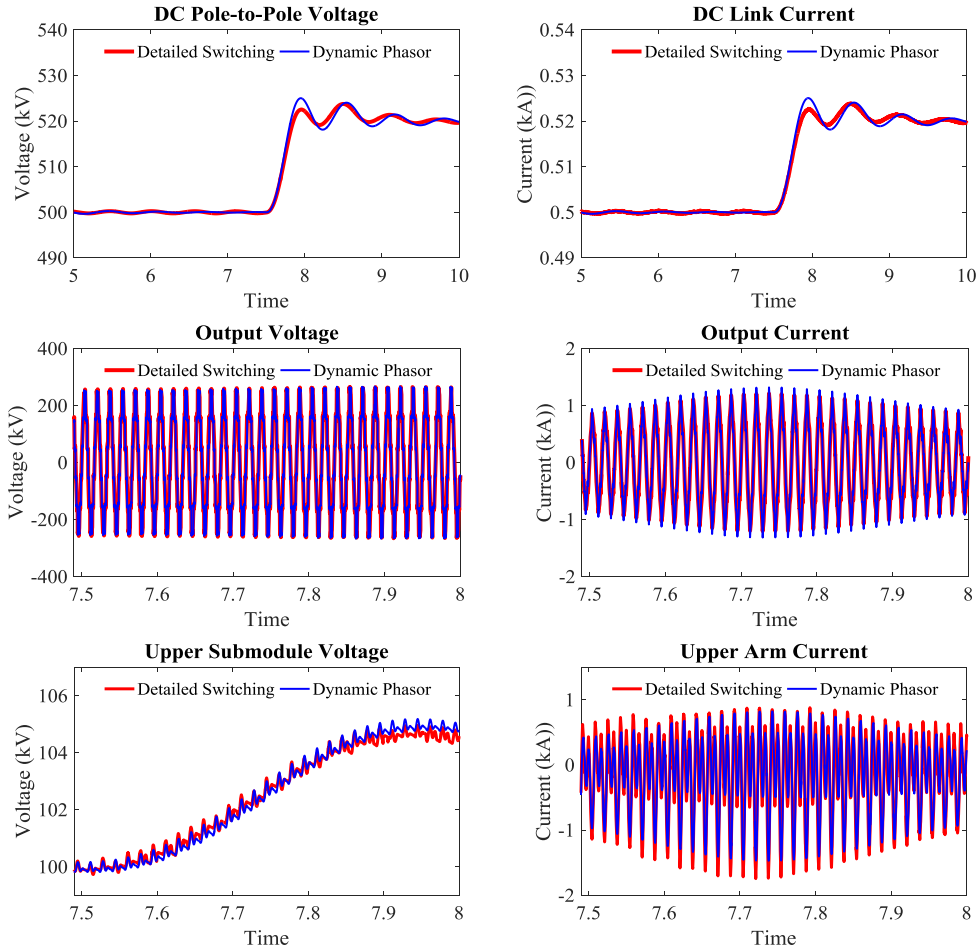
Figure 5.12 : MMC rectifier response to a step change in DC voltage reference

Since the load is purely resistive, an increase of DC voltage increases the DC current correspondingly. It does not affect the AC voltage because the voltage is controlled at 1 pu by means of a separate controller. However, in order to increase the DC voltage, it draws more power from the AC side, thus, the AC current and arm currents are subjected to transients. Dynamic responses of both PSCAD/EMTDC model and the dynamic phasor model are nearly identical.

5.3 MMC Operation in a Back-to-Back System

5.3.1 Test System Specifications
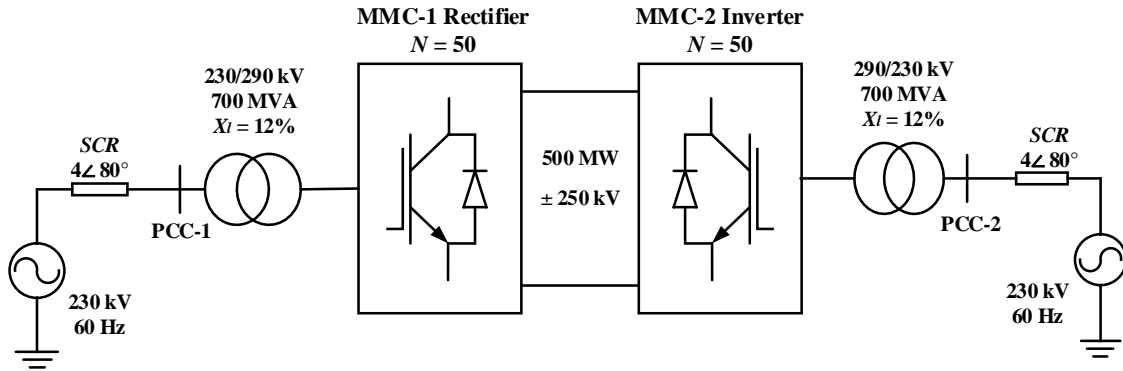
Figure 5.13 : Back-to-back system test system configuration

A back-to-back HVDC system as shown in Figure 5.13 is chosen as the next study case. Two similar AC systems are considered and power is sent from system-1 to the system-2 via the back-to-back system. System parameters are given in Table 5-2.

Voltage magnitude and real power flow into the AC sytem-2 are controlled at the MMC-2 by means of simple PI controllers. DC pole-to-pole voltage and reactive power flow to the AC sytem-1 are controlled at MMC-1. The number of levels per MMC arm is increased to 50 in order to present a more realistic scenario and reduce the harmonic content of waveforms. Therefore, the dynamic phasor results are compared with another validated MMC model (referred to as detailed average model henceforth) with less computational load, which is also developed in PSCAD/EMTDC environment as the simulation of the switching MMC model with such a large number of submodules is not practical. Dynamic phasor model is simulated at 100 µs and harmonics up to 45th order are considered. 20 µs is used for the detailed average model simulation.

Table 5-2 : MMC back-to-back system specifications

Parameter	MMC-1 values	MMC-2 values
AC system voltage	230 kV	230 kV
AC system frequency	60 Hz	60 Hz
Short circuit ratio (SCR)	4.0 ∠ 80°	4.0 ∠ 80°
Transformer voltage ratio	290 kV:230 kV	290 kV:230 kV
Transformer power rating	700 MVA	700 MVA
Transformer leakage reactance	0.12 pu	0.12 pu
MMC submodule capacitance	5000 μF	5000 μF
Number of submodules per arm	50	50
MMC arm inductance	21 mH	21 mH
MMC arm resistance	0.05 Ω	0.05 Ω
Nominal DC voltage	±250 kV	
Nominal DC power	500 MW	

5.3.2   Real Power Control

Initially the power flow from AC system-1 to AC system-2 through the HVDC system is controlled at 500 MW and is then reduced to 400 MW at t = 7.5 s. Dynamic responses of both MMC models are shown in Figure 5.14.
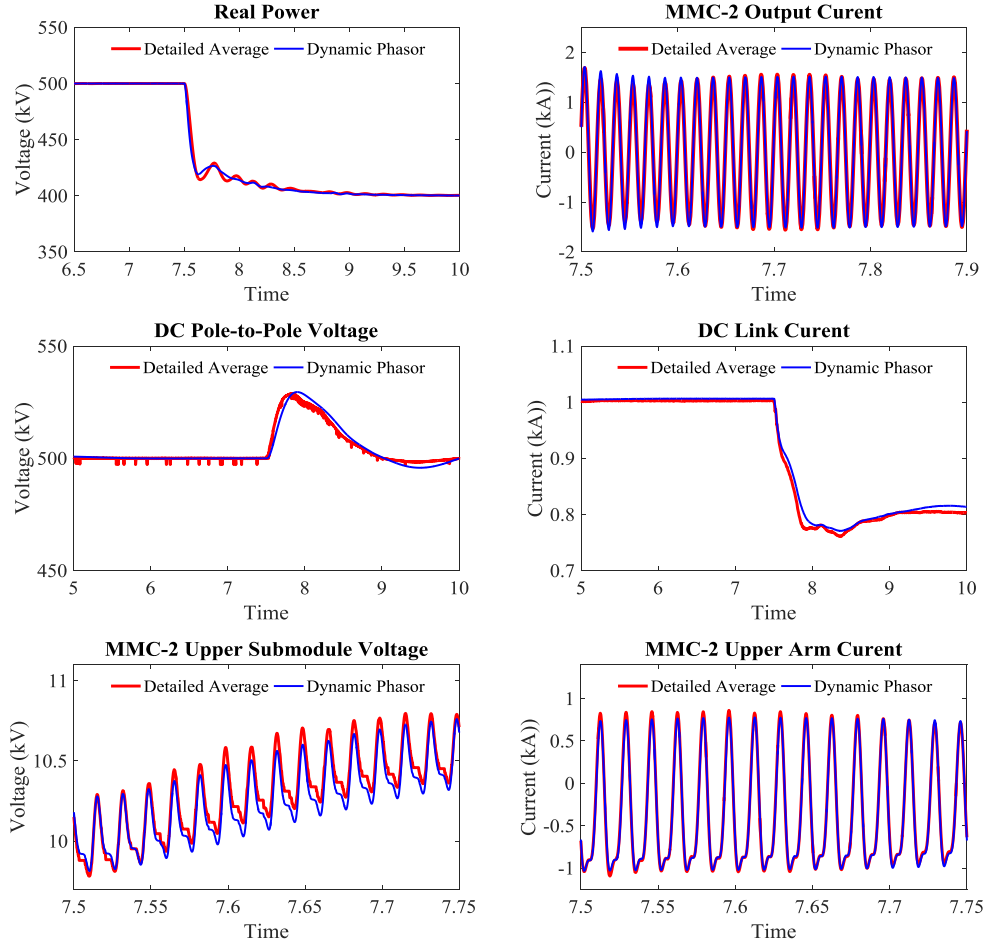
Figure 5.14 : MMC back-to-back system response to real power control

Only the waveforms that are subjected to transients are shown. Since AC system-2 voltage is controlled at 1 pu, the output current of the MMC-2 responds to the change of power and follows the oscillations of the real power flow during the transient. MMC-1 initially sends the same amount of power as demanded by the MMC-2. Therefore, the sudden reduction of power drawn from system-2 increases the DC voltage until the dc voltage controller reacts to the situation and regulates the DC voltage. DC current is reduced from 1 kA to 0.8 kA. The average capacitor voltage follows the same pattern as the DC bus voltage and the arm currents of MMC-2 follow the same pattern as system-2 output current. For clarity of the illustration of the ripples of internal waveforms, only a small duration of the dynamics is shown.

84

5.3.3 Reactive Power Control

The system is started with MMC-1 feeding 200 MVAr of reactive power to system-1. Then the reactive power reference is change to -50 MVAr at t = 7.5 s.
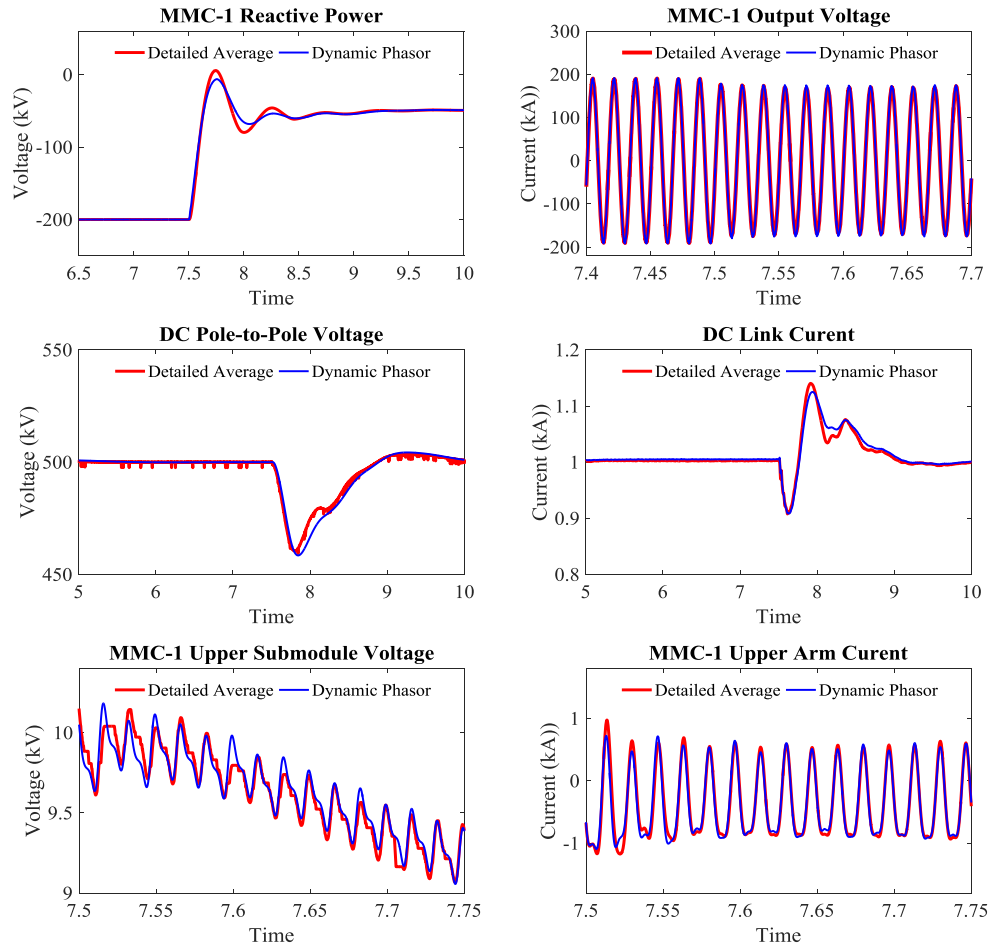
Figure 5.15 : MMC back-to-back system response to reactive power control

As seen from Figure 5.15, the voltage magnitude of system-1 is reduced as a result of reduced reactive power flow. This unexpected reduction of voltage magnitude gives a sudden reduction of MMC-2 side power flow for a small duration, thus, creating a voltage sag at the DC bus.

It can be seen that the capacitor ripples of the detailed average model are distorted at certain points due to the large simulation time-step. However, dynamic

phasor model still preserves the accuracy with the same time-step. Regardless of the distortion, transient responses of both models are approximately equal.

5.3.4   DC Pole-to-Pole Voltage Control

At the start the DC pole-to-pole voltage reference is set to 500 kV and 500 MW of power flows from AC system-1 to AC system-2. DC voltage reference is increased to 520 kV at t = 7.5 s.
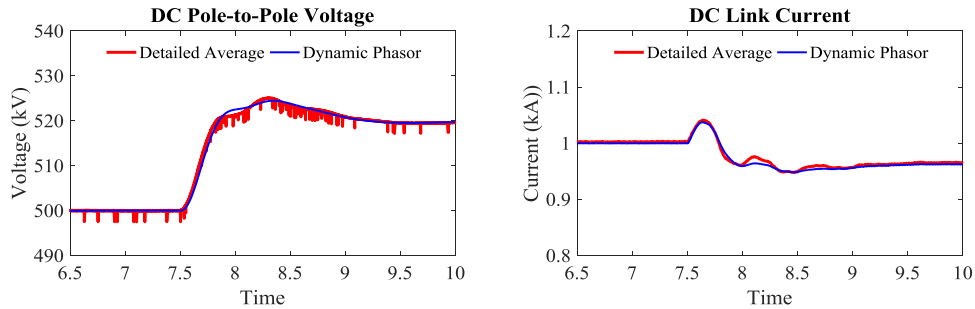
Figure 5.16 : MMC back-to-back system response to DC voltage control

Figure 5.16 illustrates the dynamic responses of DC link voltage and current waveforms to increase of DC voltage reference. DC voltage undergoes a small oscillation and settles at 520 kV. DC current is reduced to maintain constant power demanded by the AC system-2.

5.3.5   Real Power Reversal

Initially the back-to-back system is set to send 500 MW of real power to AC sytem-2 from AC system-1. At t = 7.5 s, the real power reference of MMC-2 is change from 500 MW to -500 MW. The change correspond to a power flow reversal from AC system-2 to AC system-1. System responses to real power reversal are illustrated in Figure 5.17.
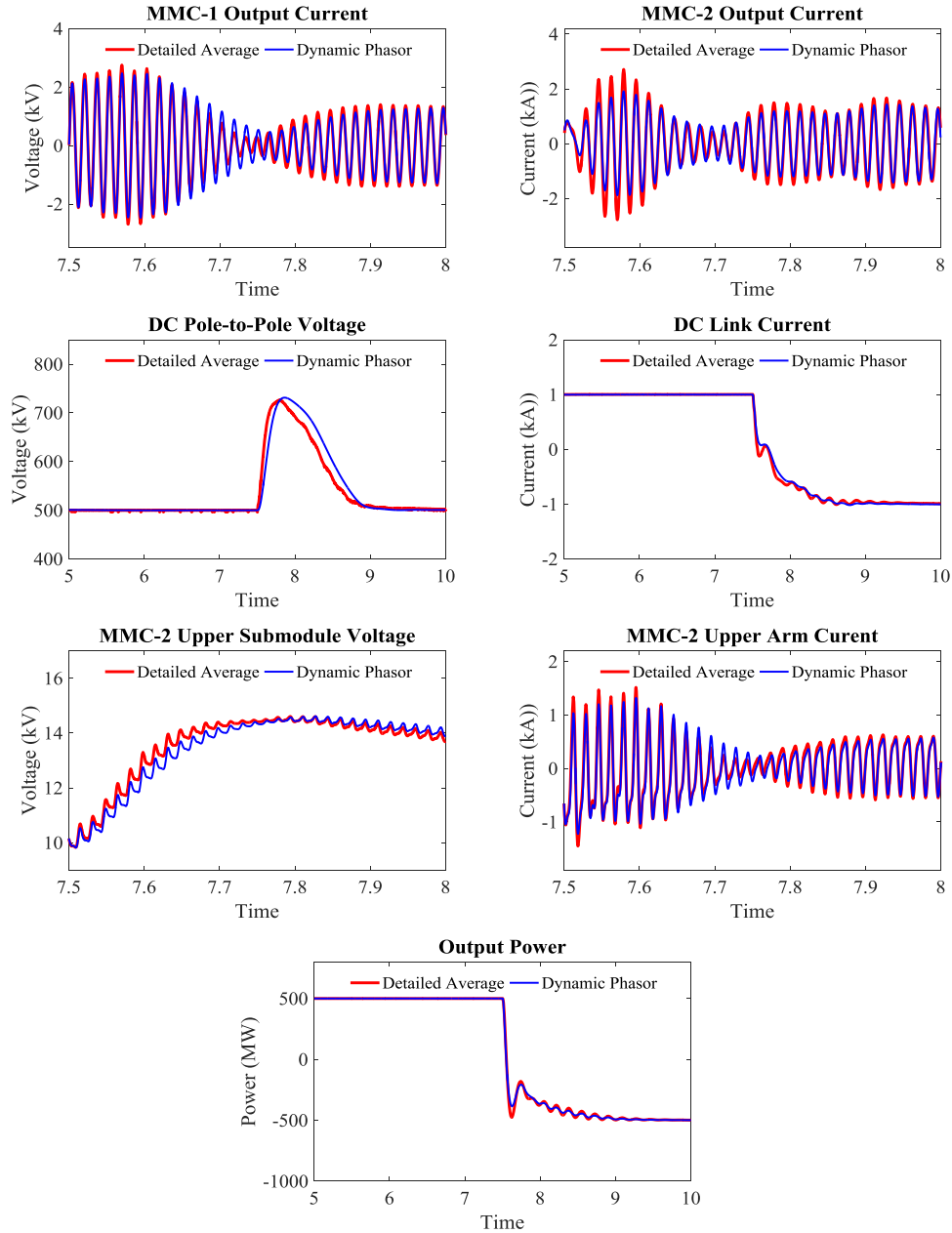
Figure 5.17 : MMC back-to-back system response to real power reversal

Phase currents of both AC systems are changed during the power flow reversal.
DC current is reversed from 1 kA to -1 kA; the DC bus voltage is maintained at 500
kV before and after the transient. Change of power direction without changing DC
voltage is one of the main advantages of VSC-HVDC systems compared to traditional
LCC-HVDC schemes.

5.4   Twelve-Bus System

5.4.1   Test System Specifications

A 12-bus system is selected as the fourth test system for the purpose of testing the dynamic phasor MMC model in a large power system with machine dynamics. The single-line circuit diagram of the 12-bus system is provided in Appendix A of this thesis and more details can be found in [51]. A 600-km long, 500-kV MMC-HVDC link is placed between bus-1 and bus-3 and 350 MW of real power is sent from bus-1 to bus-3. System specifications are tabulated in Table 5-3.

Table 5-3 : Twelve-bus system and MMC-HVDC link specifications

Parameter	MMC-1 (bus-1)	MMC-2 (bus-3)
AC system voltage	230 kV	230 kV
AC system frequency	60 Hz	60 Hz
Transformer voltage ratio	230 kV : 290 kV	230 kV : 290 kV
Transformer power rating	700 MVA	700 MVA
Transformer leakage reactance	0.1 pu	0.1 pu
MMC submodule capacitance	10 mF	10 mF
Number of submodules per arm	50	50
MMC arm inductance	0.01 H	0.01 H
MMC arm resistance	0.05 Ω	0.05 Ω
Nominal DC voltage	$\pm$250 kV	
Nominal DC power	350 MW	

Voltage magnitude and real power flow into bus-3 are controlled at the MMC-2 and the DC pole-to-pole voltage and voltage magnitude of bus-1 are controlled at MMC-1. The dynamic phasor model results are validated by implementing the same

88

system with a detailed average model of MMC. The 12-bus system with dynamic phasor model is simulated using time-step of 50 µs and the twelve-bus system with detailed averaged model is simulated using 1 µs since its accuracy deteriorates if large time-step is used.

5.4.2   Remote Generator Voltage Reference Change

A step increase from 1 pu to 1.05 pu is given to the voltage reference of the generator connected to bus-12 at t = 15 s. Dynamic responses of MMCs and corresponding busses are shown in Figure 5.18.
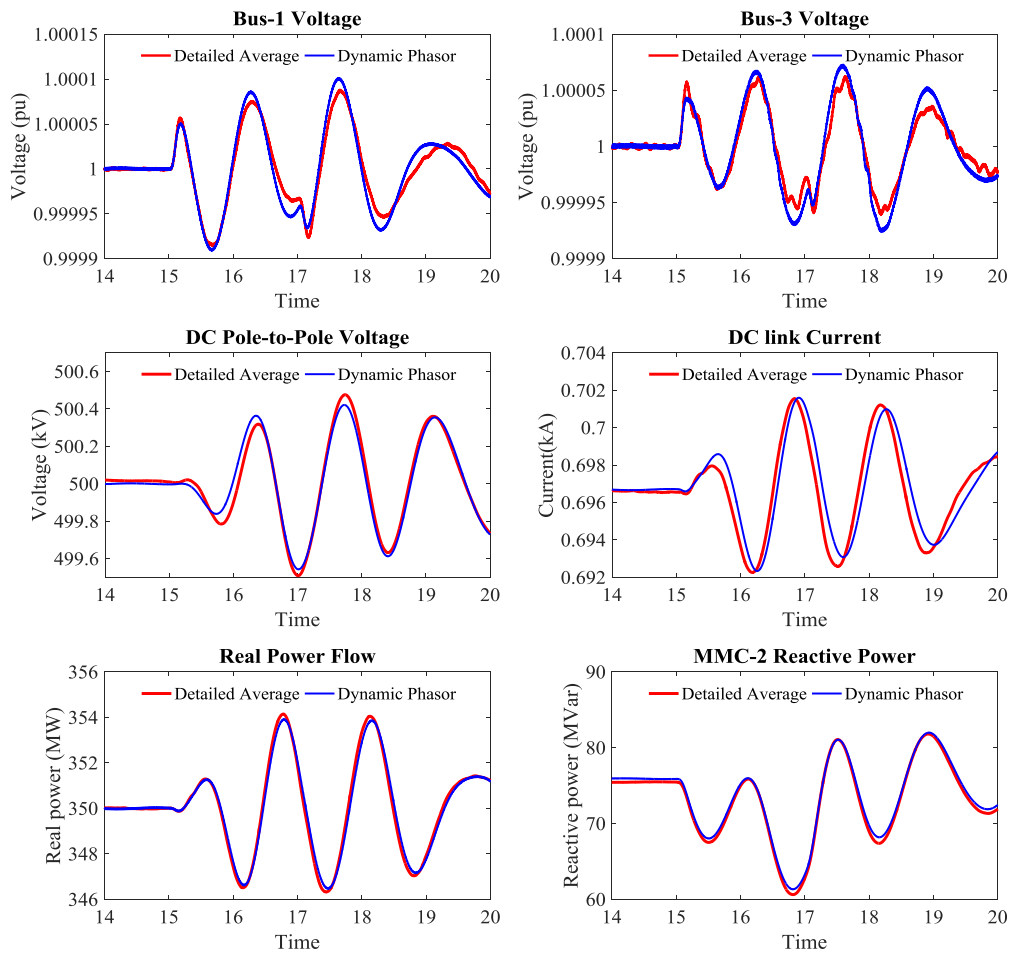
Figure 5.18 : MMC responses to generator voltage reference increase at bus-12

Responding to generator voltage reference change at bus-12, each parameter shown in Figure 5.18 undergoes to a small transient. However, the variations of those waveforms are not significant compared to steady state values and they come back to controlled value after a few oscillations. As it can be observed, both models provided the same dynamic responses.

5.4.3 Three-Phase Symmetric Fault

As the next scenario, a remote symmetric three-phase-to-ground fault is applied at bus-6. The fault is applied for a 50 ms duration at t = 15 s and waveforms of MMCs and corresponding busses are illustrated in Figure 5.19.
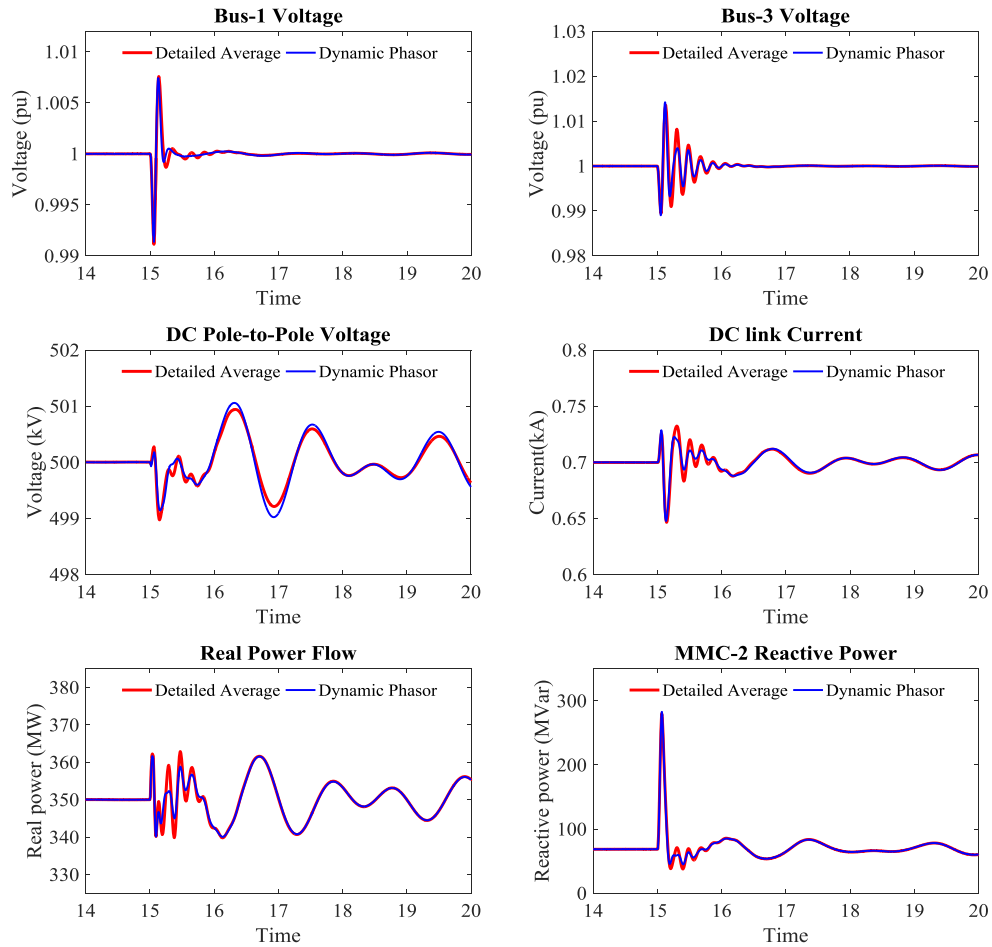
Figure 5.19 : MMC responses to remote three-phase fault in 12-bus system

It can be seen that dynamic phasor model closely follows the dynamic and steady state responses of detailed average model. There is small visible mismatches of magnitudes at certain points of some waveforms; however, the mismatches are very small and negligible compared to steady state values.

5.4.4   System Response to MMC-2 Voltage Control

In subsections 5.4.2 and 5.4.3, MMC behaviour for various disturbances in AC system was studied and compared. Focus of this subsection is to study the system dynamic response to a change in the MMC-HVDC link. A step change to the inverter bus (bus-3) voltage reference is given by means of MMC-2's voltage controller. Initially bus-3 voltage is set to 1 pu and then reduced to 0.95 pu at $t = 15$ s.

Figure 5.20 illustrates the voltage magnitudes of several selected busses (bus-1, 2, 3, 4, 5, and 6). It can be observed that the bus-3 voltage is reduced from 1 pu to 0.95 pu. As a results, voltage of bus-4 is also reduced and voltages of bus-2 and 5 are slightly increased. There is no visible change of voltage magnitudes of bus-1 and bus-6 after the transient. Dynamic results of both models are nearly matching. However, it can be seen that few small oscillations are missing from the dynamic phasor model at the start of the transient. The reason could be attributed to the fact that the number of submodules per arm is large; therefore, the time-step used to simulate the detailed average model is not adequate. However, further reduction of the time-step is not practical since it consumes lots of time for simulation.
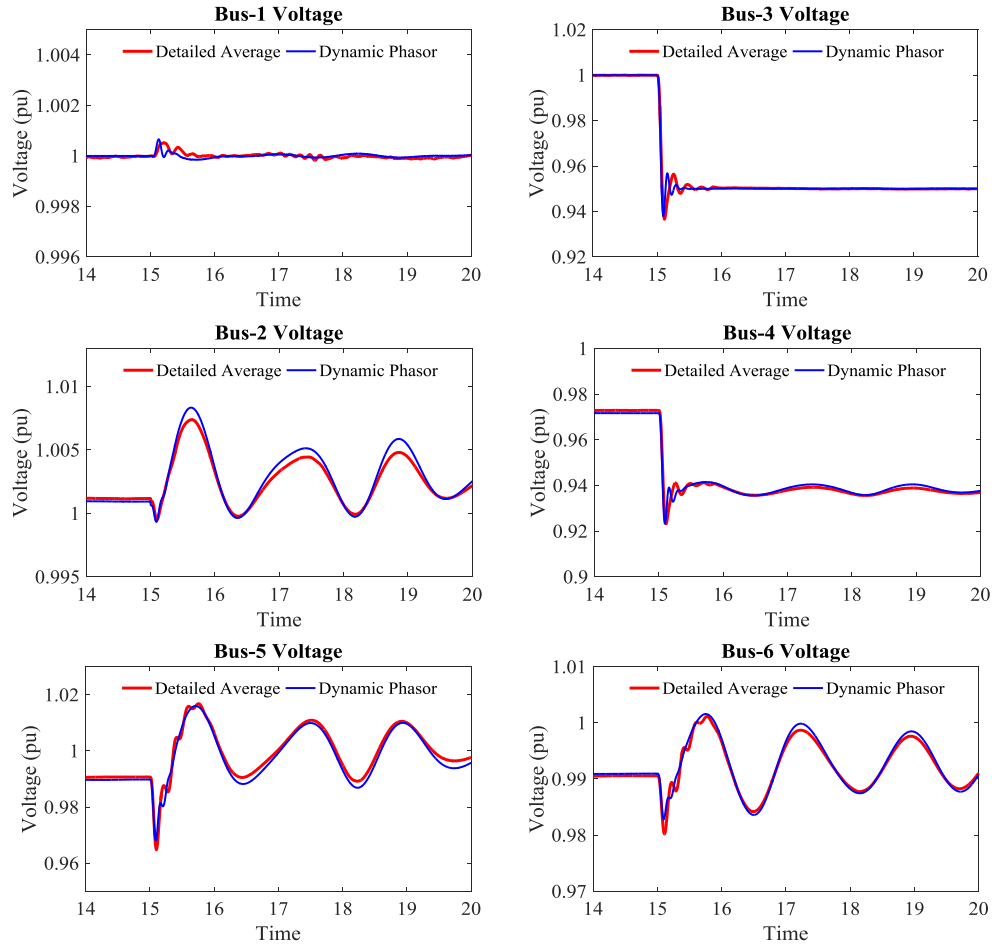
Figure 5.20 : Bus voltage change of 12-bus system for step change in MMC-2 voltage reference

5.5   Time and Speed-Up Comparisons

A simulation speed comparison is conducted in order to quantify the advantage given by the new dynamic phasor EMT model compared to the detailed switching model and the detailed average model. Simulations are performed on a computer with a 2.60 GHz, Intel core i5-3230M processor and 8 GB of RAM running PSCAD/EMTDC version 4.5.3.0.

5.5.1　Influence of Time-Step and Harmonic Content

For detailed switching model simulation, only a 6-level (5 submodules per arm) MMC was available. Therefore, the inverter system discussed in Section 5.1 is considered and simulation time of detailed switching model running at 5 μs is taken as the benchmark for speed-up comparison. A 5-s duration is considered for simulation.

Table 5-4 : Simulation time of 6-level detailed switching
MMC model

Time-Step (Δt)	Simulation time
5 μs	269.038 s

Time taken for dynamic phasor MMC model embedded inverter system simulation is measured by gradually increasing the modeled harmonic content (h) of output waveforms for different time-steps. Simulation time for larger time-steps are measured by running simulations for longer periods and interpolating result to 5 s period for higher accuracy. Comparative results are presented in Table 5-5.

It can be observed that for a six-level MMC, the dynamic phasor model provides a factor of 2.3 speed-up if the same time-step is used. However, one of the main advantages of the dynamic phasor model compared to switching model and other types of averaged models is the ability to use a larger time-step in EMT simulation. As it can be observed from tabulated results, the advantage in terms of simulation speed increases as the time-step of dynamic phasor model simulation is increased. Simulation is approximately 120 times faster if a 250-μs time-step is used.

Table 5-5 : Simulation time comparison of dynamic phasor MMC model for different time-steps and harmonic content

$\Delta t \setminus h$	1		21		45		99	
	Time(s)	Speed -up ratio (%)	Time(s)	Speed -up ratio (%)	Time(s)	Speed -up ratio (%)	Time(s)	Speed -up ratio (%)
5 µs	113.308	239	115.098	234	115.16	233	115.91	233
20 µs	78.728	341	79.415	342	81.583	338	84.495	329
50 µs	17.071	1575	17.327	1556	17.904	1552	18.33	1502
100 µs	7.202	3735	7.28	3751	7.535	3695	7.712	3570
250 µs	2.049	13130	2.097	12830	2.167	12415	2.354	11429
350 µs	1.397	19258	1.471	18289	1.53	17584	1.63	16505

Another observation that can be seen from Table 5-5 is that the simulation time does not change significantly if the order of modeled harmonic content of the output voltage waveform is increased to a larger value. This is due to the fact that the BFDP captures and models all harmonics in one equation. Therefore, the computation increase corresponding only to the calculation of switching function and the weight of switching function calculation is very small compared to rest of the computations. If CDP principle were used, the number of equations would be increased proportionally to harmonic order and a separate integration had to be done to capture each frequency component of the output current adding significant computational burden.

5.5.2   Influence of the Number of Submodules per Arm

In the previous section, simulation time comparison was made considering only five submodules per arm. However, in real-world applications, the number of submodules per arm is much higher and falls in to the range of several hundreds. Simulation of

detailed switching MMC model with hundreds of submodules per arm is not practical. Therefore, the influence of number of submodules for simulation speed is compared against the detailed average model of the MMC by simulating the back-to-back system given in Figure 5.13 and gradually increasing the number of submodules per arm. A period of 10 s is simulated using a time-step of 100 μs for both models. The number of harmonics considered for dynamic phasor model is 45. Time taken for simulations are tabulated in Table 5-6.

Table 5-6 : Influence of arm submodule number for simulation time of dynamic phasor MMC model and detailed average MMC model

Number of SM per arm	Detailed average MMC model simulation time	Dynamic phasor MMC model simulation time	Speed-up ratio (%)
5	17.564 s	23.733 s	74.0067
25	25.308 s	25.735 s	98.3408
50	37.04 s	31.133 s	118.9734
100	64.563 s	39.567 s	163.1739
200	152.354 s	56.696 s	268.7209
400	471.297 s	61.574 s	765.4156

When the number of voltage levels increases, the nearest level controller of dynamic phasor model performs more computations to determine the switching states, thus, the simulation time is increased. However, increase of simulation speed is significantly less compared to the detailed average model of the MMC. It can be observed that when the number of submodules is less, the dynamic phasor model is less effective but when it increases to a value more than 25, the dynamic phasor model start to demonstrate significant speed performances compared to detailed average model of the MMC. Almost all the MMC applications are expected to have large submodules per arm; therefore, the dynamic phasor model is going to be more advantageous in EMT simulation of realistic applications.

It is important to note that this comparison is made against the detailed average model of the MMC using the same time-step. Therefore, it is expected that the simulation speed of dynamic phasor model is to be much higher compared to a detailed switching MMC model when the number of submodules per arm is large. The advantage can be improved further by using a larger time-step for dynamic phasor model simulation.

5.6   Summary and Major Conclusions

In this chapter, validation for dynamic phasor MMC model proposed in Chapter 5 was carried out against a switching MMC model and the detailed average MMC model in PSCAD/EMTDC environment. Four HVDC test systems were considered for the result comparison.

To begin with, inverter and rectifier operation of the proposed model of MMC was analysed separately and steady state and dynamic results were compared with the detailed switching model. Due to practical limitations, the switching model was constructed only with five submodules per arm. Then the dynamic phasor model was embedded to a back-to-back system considering a large number of submodules per arm. Real and reactive power control, DC bus voltage control and real power reversal of the back-to-back system were separately analysed. Then, the MMC model was embedded and tested in a large electrical network. Finally, a simulation speed comparison was made in order to analyse the time advantage given by the proposed model.

During the experiments carried out in this chapter, it was found that the new dynamic phasor MMC model provides accurate steady state and transient responses

in both internal and external waveforms compared to other MMC models. The accuracy of waveforms can be improved by adding more harmonic contents of output waveforms without significant variation of simulation speed. Furthermore, the new model provided accurate results for larger simulation time-steps that other two models cannot use. The dynamic phasor model was significantly faster than both other MMC models with large number of submodules per arm if simulated with a same time-step. The advantage can be further improved by running simulations with a larger simulation time-step.

Chapter 6

Contributions, Conclusions and Future Work

6.1   Contributions and Conclusions

The main contribution of this research work is the development of a new flexible and efficient dynamic phasor-based MMC model for EMT-type simulations. What follows next are the contributions made throughout this work and distinct conclusions drawn from each contribution.

1. A review on MMC topology, operation, control, and application

   Origination of MMC has laid a path to new research aspects, such as finding various topologies, control schemes, modulation strategies, and developing different types of models, over the past years. The overview of the MMC presented in Chapter 2 summarized the basic operation, circuit configuration, modulation and submodule capacitor voltage balancing, medium and high power applications and general advantages given by MMC compared to other VSC topologies.

2. A comparative study of dynamic phasor principles

   Two dynamic phasor concepts, the traditional concept (CDP) and a novel one (BFDP), were presented and comparative studies were carried out taking the case of six-pulse thyristor converter as an example. Comparative results obtained by implementing the same system in PSCAD/EMTDC simulator clarified that both concepts are capable of providing accurate steady state and dynamic results. However, it was shown that the BFDP provides a significant computational advantage over the traditional method in modeling applications with several harmonics.

3. Development of new extended-frequency dynamic phasor model of an MMC for EMT simulation

   A novel model of an MMC based on CDP-BFDP hybrid approach was developed and presented in this thesis. The model is flexible to accurately produce any user-defined number of frequency components of output waveforms based on the level of detail required. Also, it produces the most dominant harmonic contents of the internal dynamics thus retaining important operating quantities. The new model is extendable to include any number of submodules per arm.

4. Extending the concept of BFDP into power-electronic converter modeling

   Virtually all dynamic phasor modeling studies of power electronic converters reported in literature have been carried out focusing only on the low-frequency contents of converter waveforms in part due to the lack of effectiveness of the CDP method in modeling a large number of harmonics. However, the use of BFDP concept for power electronic converter modeling, as proven in this thesis, opens up the opportunity to replicate any number of harmonics without giving up accuracy

or simulation speed. Therefore, the contribution made by extending BFDP to power electronic converter modeling is expected to make an important impact on modeling applications.

5. Integrating the newly developed dynamic phasor MMC model in an EMT simulator interfacing the rest of the electrical network

The new MMC model was programed and embedded as a custom component in PSCAD/EMTDC transient simulator. AC and DC side's interfaces of the MMC were represented by dependent voltage and current sources, respectively, and the command for each source was given through the user-defined component. The model was successfully interfaced with the rest of the electrical network and the control systems developed in the EMT simulator.

6. Validation of the model under various types of disturbances incorporating the model into very small to large scaled test systems

Inverter operation, rectifier operation, back-to-back HVDC system operation, and operation within a large electrical network of the new dynamic phasor MMC model were tested for various scenarios and it was found that the results closely match the results of detailed switching model and a detailed averaged model both implemented in PSCAD/EMTDC environment. Compared to the other two models, the accuracy of the dynamic phasor waveforms can be improved by considering a larger frequency content and/or considering higher number of submodules per arm. It was observed that the new model provided accurate steady state and dynamic representation even for a larger simulation time-step while the accuracy of other two models were deteriorated at rather small time-steps.

7. Analysis of the speed performance of the model by taking harmonic content, simulation time-step and complexity of the MMC into consideration

Speed analysis done in Section 5.5 revealed that the new model allows to add more frequency components without significantly increasing the simulation speed, thus, the precision of waveforms can be improved efficiently. The speed advantage given by the dynamic phasor model increases steeply when simulating real world scenarios, which consist of a large number of submodules. The ability to use a larger simulation time-step makes it even more appealing (speed wise) compared to detailed switching and detailed averaged models.

As a summary, the effort of developing a flexible averaged model for EMT co-simulation can be concluded as successful. Validation results illustrated that the new model preserves precision during both steady state and transient conditions with much improved efficiency. This model is an improvement compared to the detailed models and other average models since the user can select the compromise between the accuracy and the simulation speed. Considering the flexibility and the accuracy, this model is expected to be useful in design applications such as control tuning, component ratings, and insulation level design. Furthermore, it can be used for many research and study purposes, including, but not limited to, studying the functional and low frequency behavior of large power systems, and transient stability studies.

6.2   Limitations and Future Work

During the modeling and validation process, few limitations that lay the platform for significant future work on the new dynamic phasor model were identified. The followings can be viewed as the potential future extensions of this research.

1. Initializing an HVDC system with the dynamic phasor MMC model was done manually by connecting a voltage source to the DC link at start-up then disconnecting it after steady state voltage and power are reached. Therefore, the start-up behavior of the system cannot be studied with the developed model. Implementing a proper energising procedure can be viewed as a possible future direction of this research.

2. Even though it is often adequate to consider the two most dominant harmonic components of capacitor voltages and arm current waveforms as in the developed model, the accuracy of internal waveforms deteriorates if the output waveforms consist of a great deal of harmonics. Therefore, one can make the model flexible to include as many frequency components as required to model internal waveforms. However, the inclusion of more harmonics in those waveforms will increase the computational burden.

3. Another way of improving the accuracy of internal waveforms is to add a circulating current suppression controller to the control system. This will reduce the magnitude of higher frequency contents of arm currents and is expected to enhance the accuracy of dynamic phasor model internal waveforms, which are modeled considering only dc and second-order harmonics.

4. The method developed in the thesis is limited to the NLC modulation method. Extending the modulation to other PWM techniques can be considered as another possible extension of this model. However, unlike in NLC modulation, obtaining Fourier coefficients of the discrete functions that take place due to other PWM methods will be a challenge.

5. During the modeling process of the dynamic phasor MMC, balanced grid conditions are assumed. (for example (4.9) and (4.10)). On the other hand, all the test systems studied in this thesis, phases are not independently controlled. Thus, MMC responses for unbalanced grid conditions may be problematic. More research can be done in this area in order to rectify this limitation. One possible way of doing this is controlling positive, negative, and zero sequence components separately with the MMC modeled in d-q frame.

6. During startup and dc faults, the IGBTs of the MMC are blocked, thus transforming the MMC to a six-pulse diode converter. However, in the proposed representation of MMC (Figure 4.3), the block mode operation of the MMC cannot be accurately modeled since each phase is represented using only an equivalent voltage source. Therefore, investigations have to be done to modify the MMC representation in order to characterize the blocked mode operation of the MMC.

References

[1]   K. Sharifabadi, L. Harnefors, P. Nee, S. Norrga, and R. Teodorescu, *Design, Control and Application of Modular Multilevel Converters for HVDC Transmission Systems*. John Wiley & Sons, Incorporated, 2016.

[2]   A. Dekka, B. Wu, R. L. Fuentes, M. Perez, and N. R. Zargari, "Evolution of Topologies, Modeling, Control Schemes, and Applications of Modular Multilevel Converters," *IEEE J. Emerg. Sel. Top. Power Electron.*, vol. 5, no. 4, pp. 1631–1656, 2017.

[3]   J. Glasdam, J. Hjerrild, Ł. H. Kocewiak, and C. L. Bak, "Review on multi-level voltage source converter based HVDC technologies for grid connection of large offshore wind farms," in *2012 IEEE International Conference on Power System Technology (POWERCON)*, 2012, pp. 1–6.

[4]   R. Feldman *et al.*, "A Hybrid Modular Multilevel Voltage Source Converter for HVDC Power Transmission," *IEEE Trans. Ind. Appl.*, vol. 49, no. 4, pp. 1577–1588, Jul. 2013.

[5]   K. Friedrich, "Modern HVDC PLUS application of VSC in Modular Multilevel Converter topology," in *2010 IEEE International Symposium on Industrial Electronics*, 2010, pp. 3807–3810.

[6]   H. Saad *et al.*, "Modular Multilevel Converter Models for Electromagnetic Transients," *IEEE Trans. Power Deliv.*, vol. 29, no. 3, pp. 1481–1489, Jun. 2014.

[7]   S. Debnath, J. Qin, B. Bahrani, M. Saeedifard, and P. Barbosa, "Operation, Control, and Applications of the Modular Multilevel Converter: A Review," *IEEE Trans. Power Electron.*, vol. 30, no. 1, pp. 37–53, Jan. 2015.

[8]   U. N. Gnanarathna, A. M. Gole, and R. P. Jayasinghe, "Efficient Modeling of Modular Multilevel HVDC Converters (MMC) on Electromagnetic Transient Simulation Programs," *IEEE Trans. Power Deliv.*, vol. 26, no. 1, pp. 316–324, Jan. 2011.

[9]   A. Lesnicar and R. Marquardt, "An innovative modular multilevel converter topology suitable for a wide power range," in *2003 IEEE Bologna Power Tech Conference Proceedings,* 2003, vol. 3, pp.1- 6

[10]   N. Watson and J. Arrillaga, *power system electromagnetic transient simulation.* 1st ed., ser. IET Power and Energy Series, The Institution of Engineering and Technology, 2003, vol. 39

[11]   M. Kulasza, "Generalized dynamic phasor-based simulation for power systems," M.Sc. thesis, Dept. Elect. and Com. Eng., Uni. of. Manitoba, Canada, 2014.

[12]   J. Mahseredjian, V. Dinavahi, and J. A. Martinez, "Simulation Tools for Electromagnetic Transients in Power Systems: Overview and Challenges," *IEEE Trans. Power Deliv.*, vol. 24, no. 3, pp. 1657–1669, Jul. 2009.

[13]   J. Peralta, H. Saad, S. Dennetiere, J. Mahseredjian, and S. Nguefeu, "Detailed and Averaged Models for a 401-Level MMC-HVDC System," *IEEE Trans. Power Deliv.*, vol. 27, no. 3, pp. 1501–1508, Jul. 2012.

[14] H. Saad *et al.*, "Dynamic Averaged and Simplified Models for MMC-Based HVDC Transmission Systems," *IEEE Trans. Power Deliv.*, vol. 28, no. 3, pp. 1723–1730, Jul. 2013.

[15] J. Xu, A. M. Gole, and C. Zhao, "The Use of Averaged-Value Model of Modular Multilevel Converter in DC Grid," *IEEE Trans. Power Deliv.*, vol. 30, no. 2, pp. 519–528, Apr. 2015.

[16] S. R. Deore, P. B. Darji, and A. M. Kulkarni, "Dynamic phasor modeling of Modular Multi-level Converters," in *2012 IEEE 7th International Conference on Industrial and Information Systems (ICIIS)*, 2012, pp. 1–6.

[17] D. Jovcic and A. A. Jamshidifar, "Phasor Model of Modular Multilevel Converter With Circulating Current Suppression Control," *IEEE Trans. Power Deliv.*, vol. 30, no. 4, pp. 1889–1897, Aug. 2015.

[18] S. Rajesvaran, "Modeling of modular multilevel converters using extended-frequency dynamics phasors," M.Sc. thesis, Dept. Elect. and Com. Eng., Uni. of. Manitoba, Canada, Sep. 2016.

[19] S. Rajesvaran and S. Filizadeh, "Modeling modular multilevel converters using extended-frequency dynamic phasors," in *2016 IEEE Power and Energy Society General Meeting (PESGM)*, 2016, pp. 1–5.

[20] M. A. Perez, S. Bernet, J. Rodriguez, S. Kouro, and R. Lizana, "Circuit Topologies, Modeling, Control Schemes, and Applications of Modular Multilevel Converters," *IEEE Trans. Power Electron.*, vol. 30, no. 1, pp. 4–17, Jan. 2015.

[21] H. Akagi, "Classification, Terminology, and Application of the Modular Multilevel Cascade Converter (MMCC)," *IEEE Trans. Power Electron.*, vol. 26, no. 11, pp. 3119–3130, Nov. 2011.

[22] S. Allebrod, R. Hamerski, and R. Marquardt, "New transformerless, scalable Modular Multilevel Converters for HVDC-transmission," in *2008 IEEE Power Electronics Specialists Conference*, 2008, pp. 174–179.

[23] R. Marquardt, "Modular Multilevel Converter: An universal concept for HVDC-Networks and extended DC-Bus-applications," in *The 2010 International Power Electronics Conference - ECCE ASIA* , 2010, pp. 502–507.

[24] J. Dorn, H. Huang, and D. Retzmann, "A new Multilevel Voltage-Sourced Converter Topology for HVDC Applications," *in CIGRE session, B4-304*, 2008, Paris, France.

[25] E. Solas, G. Abad, J. A. Barrena, S. Aurtenetxea, A. Cárcar, and L. Zając, "Modular Multilevel Converter With Different Submodule Concepts-Part I: Capacitor Voltage Balancing Method," *IEEE Trans. Ind. Electron.*, vol. 60, no. 10, pp. 4525–4535, Oct. 2013.

[26] E. Solas, G. Abad, J. A. Barrena, S. Aurtenetxea, A. Cárcar, and L. Zając, "Modular Multilevel Converter With Different Submodule Concepts-Part II: Experimental Validation and Comparison for HVDC Application," *IEEE Trans. Ind. Electron.*, vol. 60, no. 10, pp. 4536–4545, Oct. 2013.

[27] M. Glinka and R. Marquardt, "A new AC/AC multilevel converter family," *IEEE Trans. Ind. Electron.*, vol. 52, no. 3, pp. 662–669, Jun. 2005.

[28] A. Nami, J. Liang, F. Dijkhuizen, and G. D. Demetriades, "Modular Multilevel Converters for HVDC Applications: Review on Converter Cells and Functionalities," *IEEE Trans. Power Electron.*, vol. 30, no. 1, pp. 18–36, Jan. 2015.

[29] M. Zygmanowski, B. Grzesik, and R. Nalepa, "Capacitance and inductance selection of the modular multilevel converter," in *2013 15th European Conference on Power Electronics and Applications (EPE)*, 2013, pp. 1–10.

[30] K. Ilves, S. Norrga, L. Harnefors, and H. P. Nee, "On Energy Storage Requirements in Modular Multilevel Converters," *IEEE Trans. Power Electron.*, vol. 29, no. 1, pp. 77–88, Jan. 2014.

[31] Z. Xu, H. Xiao, and Z. Zhang, "Selection methods of main circuit parameters for modular multilevel converters," *IET Renew. Power Gener.*, vol. 10, no. 6, pp. 788–797, 2016.

[32] Y. Li and F. Wang, "Arm inductance selection principle for modular multilevel converters with circulating current suppressing control," in *2013 Twenty-Eighth Annual IEEE Applied Power Electronics Conference and Exposition (APEC)*, 2013, pp. 1321–1325.

[33] M. Hagiwara and H. Akagi, "Control and Experiment of Pulsewidth-Modulated Modular Multilevel Converters," *IEEE Trans. Power Electron.*, vol. 24, no. 7, pp. 1737–1746, Jul. 2009.

[34] K. Wang, Y. Li, Z. Zheng, and L. Xu, "Voltage Balancing and Fluctuation-Suppression Methods of Floating Capacitors in a New Modular Multilevel Converter," *IEEE Trans. Ind. Electron.*, vol. 60, no. 5, pp. 1943–1954, May 2013.

[35] G. S. Konstantinou, M. Ciobotaru, and V. G. Agelidis, "Operation of a modular multilevel converter with selective harmonic elimination PWM," in *8th International Conference on Power Electronics - ECCE Asia*, 2011, pp. 999–1004.

[36] F. Deng and Z. Chen, "A Control Method for Voltage Balancing in Modular Multilevel Converters," *IEEE Trans. Power Electron.*, vol. 29, no. 1, pp. 66–76, Jan. 2014.

[37] P. M. Meshram and V. B. Borghate, "A Simplified Nearest Level Control (NLC) Voltage Balancing Method for Modular Multilevel Converter (MMC)," *IEEE Trans. Power Electron.*, vol. 30, no. 1, pp. 450–462, Jan. 2015.

[38] Q. Tu, Z. Xu, and L. Xu, "Reduced Switching-Frequency Modulation and Circulating Current Suppression for Modular Multilevel Converters," *IEEE Trans. Power Deliv.*, vol. 26, no. 3, pp. 2009–2017, Jul. 2011.

[39] Q. Tu and Z. Xu, "Impact of Sampling Frequency on Harmonic Distortion for Modular Multilevel Converter," *IEEE Trans. Power Deliv.*, vol. 26, no. 1, pp. 298–306, Jan. 2011.

[40] S. Rohner, S. Bernet, M. Hiller, and R. Sommer, "Modulation, Losses, and Semiconductor Requirements of Modular Multilevel Converters," *IEEE Trans. Ind. Electron.*, vol. 57, no. 8, pp. 2633–2642, Aug. 2010.

[41] M. Daryabak, S. Filizadeh, J. Jatskevich, A. Davoudi, M. Saeedifard, V.K. Sood, J.A. Martinez, D. Aliprantis, J. Cano, and A. Mehrizi-Sani, "Modeling of LCC-HVDC Systems Using Dynamic Phasors," *IEEE Trans. Power Deliv.*, vol. 29, no. 4, pp. 1989–1998, Aug. 2014.

[42] S. Henschel, "Analysis of electromagnetic and electromechanical power system transients with dynamic phasors," Ph.D. dissertation, Uni. of British Columbia, 1999.

[43] S. Chiniforoosh, J. Jatskevich, A. Yazdani, V. Sood, V. Dinavahi, J. A. Martinez, and A. Ramirez, "Definitions and Applications of Dynamic Average Models for Analysis of Power Systems," *IEEE Trans. Power Deliv.*, vol. 25, no. 4, pp. 2655–2669, Oct. 2010.

[44] K. Mudunkotuwa, S. Filizadeh, and U. Annakkage, "Development of a hybrid simulator by interfacing dynamic phasors with electromagnetic transient simulation," *Transm. Distrib. IET Gener.*, vol. 11, no. 12, pp. 2991–3001, 2017.

[45] S. R. Sanders, J. M. Noworolski, X. Z. Liu, and G. C. Verghese, "Generalized averaging method for power conversion circuits," *IEEE Trans. Power Electron.*, vol. 6, no. 2, pp. 251–259, Apr. 1991.

[46] "Validation of Generalized State Space Averaging Method for Modeling and Simulation of Power Electronic Converters for Renewable Energy Systems." *Journal of Electrical Engineering & Technology*, vol. 2, no. 2, pp. 231-240, 2007

[47] K. Mudunkotuwa and S. Filizadeh, "Co-Simulation of Electrical Networks by Interfacing EMT and Dynamic-Phasor Simulators." in *2017 International Conference on Power System transients(IPST)*, 2017, pp. 1–5

[48] F. L. Alvarado, "Parallel Solution of Transient Problems by Trapezoidal Integration," *IEEE Trans. Power Appar. Syst.*, vol. PAS-98, no. 3, pp. 1080–1090, May 1979.

[49] M. F. Fathoni and A. I. Wuryandari, "Comparison between Euler, Heun, Runge-Kutta and Adams-Bashforth-Moulton integration methods in the particle dynamic simulation," in *2015 4th International Conference on Interactive Digital Media (ICIDM)*, 2015, pp. 1–7.

[50] H. W. Dommel, "Digital Computer Solution of Electromagnetic Transients in Single-and Multiphase Networks," *IEEE Trans. Power Appar. Syst.*, vol. PAS-88, no. 4, pp. 388–399, Apr. 1969.

[51] S. Jiang, U. D. Annakkage, and A. M. Gole, "A platform for validation of FACTS models," *IEEE Trans. Power Deliv.*, vol. 21, no. 1, pp. 484–491, Jan. 2006.

Appendix A

Twelve-Bus Power System

Given below is the single line circuit diagram of the12-bus power system simulated in this thesis.
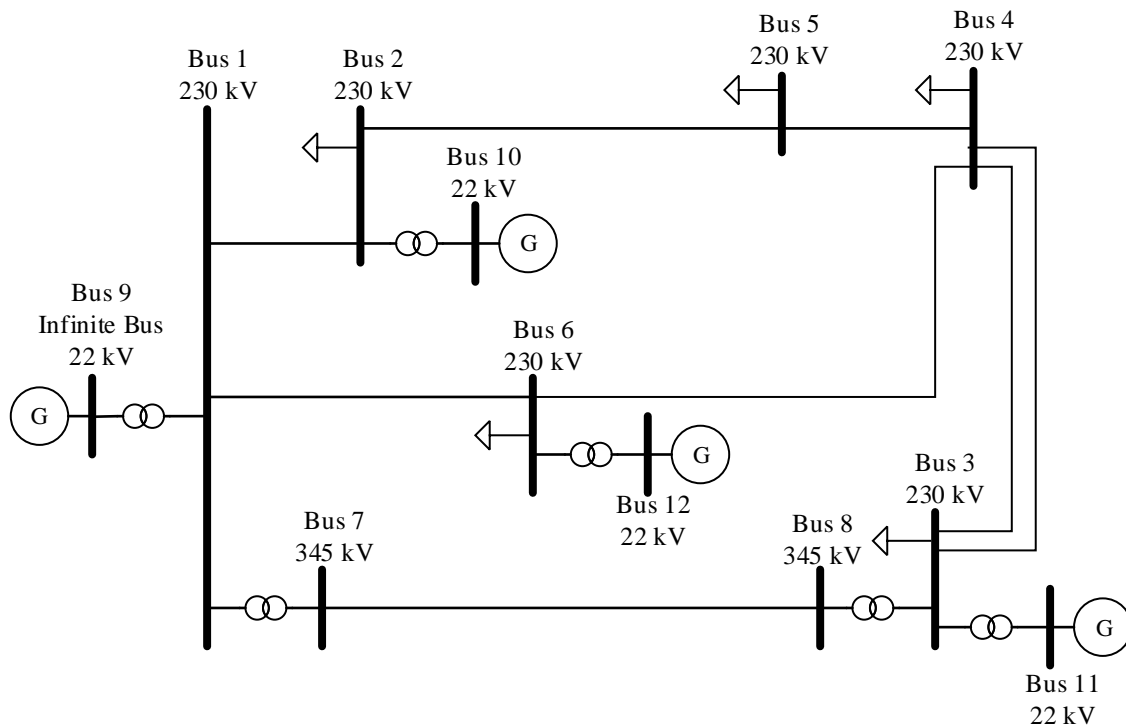
The 12-bus system consists of six 230-kV buses, two 345-kV buses, and four 22-kV generator buses. All transmission lines except one are 230 kV and the transmission line between bus-7 and bus-8 is 345 kV.